2004-05-13

Computational and experimental investigations of laser drilling and welding for microelectronic packaging

Wei Han
Worcester Polytechnic Institute

Repository Citation

Han, W. (2004). *Computational and experimental investigations of laser drilling and welding for microelectronic packaging*. Retrieved from https://digitalcommons.wpi.edu/etd-dissertations/286

Computational and experimental investigations of laser drilling and welding for microelectronic packaging

A Dissertation
Submitted to the faculty of the

Worcester Polytechnic Institute

in partial fulfillment of the requirements for the
Degree of Doctor of Philosophy in
Mechanical Engineering

by

Wei Han

10 May 2004

Approved:

Prof. Ryszard J. Pryputniewicz, Major Advisor

Prof. Cosme Furlong, Member, Dissertation Committee

Prof. Yiming (Kevin) Rong, Member, Dissertation Committee

Prof. Gretar Tryggvason, Member, Dissertation Committee

Dr. Thomas Marinis, Draper Laboratory, Cambridge, MA
Member, Dissertation Committee

Prof. John M. Sullivan, Jr., Graduate Committee Representative by

NEST – NanoEngineering, Science, and Technology
CHSLT – Center for Holographic Studies and Laser micro-mechaTronics
Mechanical Engineering Department
Worcester Polytechnic Institute
Worcester, MA 01609-2280

SUMMARY

Recent advances in microelectronics and packaging industry are characterized by a progressive miniaturization in response to a general trend toward higher integration and package density. Corresponding to this are the challenges to traditional manufacturing processes. Some of these challenges can be satisfied by laser micromachining, because of its inherent advantages. In laser micromachining, there is no tool wear, the heat affected zone can be localized into a very small area, and the laser micromachining systems can be operated at a very wide range of speeds. Some applications of laser micromachining include pulsed Nd:YAG laser spot welding for the photonic devices and laser microdrilling in the computer printed circuit board market.

Although laser micromachining has become widely used in microelectronics and packaging industry, it still produces results having a variability in properties and quality due to very complex phenomena involved in the process, including, but not limited to, heat transfer, fluid flow, plasma effects, and metallurgical problems. Therefore, in order to utilize the advantages of laser micromachining and to achieve anticipated results, it is necessary to develop a thorough understanding of the involved physical processes, especially those relating to microelectronics and packaging applications.

The objective of this Dissertation was to study laser micromachining processes, especially laser drilling and welding of metals or their alloys, for the microscale applications. The investigations performed in this Dissertation were based on analytical, computational, and experimental solutions (ACES) methodology. More specifically, the studies were focused on development of a consistent set of equations representing

interaction of the laser beam with materials of interest in this Dissertation, solution of these equations by finite difference method (FDM) and finite element method (FEM), experimental demonstration of laser micromachining, and correlation of the results.

The contributions of this Dissertation include:

1) development of a finite difference method (FDM) program with color graphic interface, which has the capability of adjusting the laser power distributions, coefficient of energy absorption, and nonlinear material properties of the workpiece as functions of temperature, and can be extended to calculate the fluid dynamic phenomena and the profiles of laser micromachined workpieces,
2) detailed investigations of the effect of laser operating parameters on the results of the profiles and dimensions of the laser microdrilled or microwelded workpiece, which provide the guideline and advance currently existing laser micromachining processes,
3) use, for the first time, of a novel optoelectronic holography (OEH) system, which provides non-contact full-field deformation measurements with sub-micrometer accuracy, for quantitative characterization of thermal deformations of the laser micromachined parts,
4) experimental evaluations of strength of laser microwelds as the function of laser power levels and number of microwelds, which showed the lower values than the strength of the base material due to the increase of hardness at the heat affected zone (HAZ) of the microwelds,

5) measurements of temperature profiles during laser microwelding, which showed good correlations with computational results,
6) detailed considerations of absorption of laser beam energy, effect of thermal and aerodynamic conditions due to shielding gas, and the formation of plasma and its effect on laser micromachining processes.

The investigations presented in this Dissertation show viability of the laser micromachining processes, account for the considerations required for a better understanding of laser micromachining processes, and provide guideline which can help explaining and advancing the currently existing laser micromachining processes. Results of this Dissertation will facilitate improvements and optimizations of the state-of-the-art laser micromachining techniques and enable the emerging technologies related to the multi-disciplinary field of microelectronics and packaging for the future.

ACKNOWLEDGEMENTS

First of all, I would like to express my deep gratitude to my advisor, Prof. Ryszard J. Pryputniewicz, for his guidance and support in the development of this Dissertation. Without his support, this work would be impossible.

Thanks are also extended to the members of my Dissertation committee; Prof. Cosme Furlong, Prof. Yiming Rong, Prof. Gretar Tryggvason, Dr. Thomas Marinis, and Prof. John M. Sullivan, Jr., for their time and assistance in this work.

Also, I would like to thank Mr. Shivananda Pai Mizar and Mr. Peter Hefti for their invaluable assistance throughout my experimental work, Mr. Adam Klempner and Mr. Ryan Marinis, for their aid during the completion of the experimental work. I would also like to thank all the other members of the Center for Holographic Studies and Laser micro-mechaTronics (CHSLT) for their support and help.

I would like to express my great gratitude to my parents and sister, for their endless love and encouragement throughout my studies at WPI.

Finally, my very special thanks to my husband, Mingzhe Li, for his profound love, patience, understanding, and unconditional support throughout the development of this Dissertation. I would not have been able to complete this work without his support.

TABLE OF CONTENTS

LIST OF FIGURES

LIST OF TABLES

NOMENCLATURE

c	specific heat, or speed of light
c_l	specific heat in liquid state
c_s	specific heat in solid state
d	distance between laser spot and thermocouple
e	strain
erf	error function
$erfc$	complementary error function
f	focal length of the lens, or laser pulse frequency
ffp	focal plane position
$f/\#$	photographic *f*-number of the lens
g	gravitational constant
g_e	degeneracy factors for electrons
g_i	degeneracy factors for ions
g_0	degeneracy factors for neutral atoms
$\bar{g}$	quantum mechanical Gaunt factor
h	melt thickness, or specific enthalpy, or Planck's constant
h_c	convective heat transfer coefficient
i	number of phase steps
k	thermal conductivity or imaginary part of the refractive index
k_{air}	thermal conductivity of the air surrounding the workpiece
k_b	Boltzmann's constant
k_l	thermal conductivity in liquid state
k_s	thermal conductivity in solid state
k_v	thermal conductivity in vaporization state
l	thermal diffusion length
l_{th}	thermal penetration depth
m	refractive index
$\bar{m}$	average mass of an evaporation atom
m_e	mass of melt ejection, or electron mass
m_s	mass of melting of solid metal
m_v	mass of evaporation
n	real part of the refractive index, or density of a weakly ionized plasma
n_c	critical electron density
n_e	electron density
n_i	density of singly ionized atoms
n_0	total gas density
p	perimeter of the workpiece, or pressure
p^{in}	pressure component enters the finite element volume
p^{out}	pressure component exits the finite element volume
p_r	recoil pressure
p_s	saturated vapor pressure

q	heat flux
q_c	convection heat flux
q_r	radiation heat flux
r	radial coordinate
s	hole depth
t	time
t_h	duration of the heating stage
t_m	duration for the temperature to reach melting temperature
t_p	laser pulse length
u	dummy variable, or internal energy
v	linear vaporization rate, or collision frequency
v_d	drilling velocity
v_{de}	“drilling” velocity due to ejection of the melt
v_{dv}	“drilling” velocity due to evaporation of the melt
v_e	melt-ejection velocity
v_m	melt velocity
v_r	radial melt flow velocity averaged over the melt layer thickness
v_v	evaporation velocity
w	laser beam radius at the surface of a workpiece, or angular frequency
w_0	Gaussian beam radius
x,y,z	Cartesian coordinates
x_R	Rayleigh range
z	axial coordinate, or deformation
z_m	melting depth penetration
A	surface area, or ambient pressure dependent coefficient, or energy absorption coefficient, or atomic constant
A_v	energy absorption coefficient in vaporization state
B_0	evaporation constant
C_V	volumetric specific heat
C_P	specific heat at constant pressure
D	diameter of the lens, or component in elasticity matrix
DOF	depth of focus
D_ave	average diameter of the microweld
D_front	entrance spot diameter on the top surface
D_min	minimum hole diameter
D_back	exit spot diameter on the bottom surface
E	energy, or modulus of elasticity
$E_{b,\lambda}$	blackbody monochromatic emissive power
E_f	an electron at the final continuum state
E_i	ionization potential for the neutral atoms in the gas at the initial continuum state
E_{req}	energy required for micromachining process
E_s	electric field intensity
E_0	maximum electric field intensity on axis

F	peak load
FDM	finite difference method
FEM	finite element method
G	collection of time and space terms of finite difference equation
I	power density
I_{abs}	absorbed laser intensity
I_m	laser beam intensity required to produce melting
I_s	laser beam intensity at the surface
I_v	threshold intensity
I_0	maximum laser beam power density, or average light intensity
J_0, J_1	Bessel functions of the first kind
L	characteristic length
L_m	latent heat of melting
L_v	latent heat of vaporization
M	mass of a neutral atom, or expansion factor of the beam expander, or moment
M_a	atomic mass
N	number of laser pulse
N_a	Avogadro's number
N_u	Nusselt number
OP	optical path
P	laser power
P_{lcond}	output power per unit length of the molten layer due to conduction
P_{lconv}	output power per unit length of the molten layer due to convection
P_{levp}	power per unit length spent for the evaporation
P_{lin}	input power per unit length of the molten layer
P_{lrad}	output power per unit length of the molten layer due to radiation
P_L	power loss from inelastic collisions
$P(\infty)$	normalized total power of the laser beam
P_0	constant power during a laser pulse
Q	source distribution function, rate at which heat is supplied
R	reflectivity, or radius of wavefront curvature
R^*	reflectivity of an opaque surface at normal incidence
R_a	Rayleigh number
R_d	electron diffusion rate
R_i	electron production rate
R_r	electron recombination rate
S	the area of the laser beam illuminates on the metal surface
T	temperature
T_{amb}	ambient temperature
T_e	excitation temperature
T_B	boiling temperature
T_l	temperature in liquid state
T_m	melting temperature

T_{ref}	reference temperature
T_s	surface temperature of the workpiece, or temperature in solid state
T_v	vaporization temperature
T^*	average temperature in the melt layer
T_0	initial temperature
ΔT	change in temperature
TS	tensile strength
U	energy of evaporation per atom, or thermal displacement
V	volume of the melted material
V_0	a coefficient of the order of magnitude of the sound velocity
Z	average ionic charge in the plasma
α	absorption coefficient, or a constant smaller than unity
α_e	coefficient of thermal expansion
$\overline{\alpha_e}(T)$	mean value of coefficient of thermal expansion
α_σ	a factor related to the coefficient of thermal expansion
β	coefficient of volumetric thermal expansion, or mass evaporation rate
γ	surface tension, or kinematic viscosity
δ	absorption depth of laser photons deposit energy
δ_m	melt-layer thickness at the edge of the laser spot
ε	emissivity, or component in total strain vector
ε_e	component in elastic strain vector
ε^{th}	component in thermal strain vector
ε_λ	weighted average of the monochromatic hemispherical emissivity
ε'	equivalent strain
ε_0	permittivity of free space
$\bar{\varepsilon}$	average electron energy
η	thermomechanical coupling factor
θ	divergence of a laser beam, or atomic constant
κ	thermal diffusivity
κ_m	thermal diffusivity of the melt metal
κ_s	thermal diffusivity of the solid metal
κ_v	thermal diffusivity of the vaporized metal
λ	wavelength
μ	melt viscosity
v	Poisson's ratio
ρ	density
σ	Stefan-Boltzmann constant, or stress, or root-mean-square surface roughness
σ_p	principle stress
σ_s	surface stresses
σ_1, σ_2, σ_3	principle stresses
σ'	von Mises or equivalent stress

τ	thermal time constant
φ	optical phase
ω	laser beam radius at the surface of a workpiece
Ω	collection of space and temperature terms in finite difference equation
∇	gradient operator

1. OBJECTIVES

The objectives of this Dissertation were to study laser micromachining processes for microelectronics and packaging applications, especially as they relate to microdrilling and microwelding of metals and their alloys. More specifically, this Dissertation was to develop a better understanding of the phenomena involved in the laser micromachining processes, than currently available. This development was to include analytical equations to represent thermal and mechanical characteristics of the processes, computational modeling of these processes, and experimental investigations of the representative processes.

2. INTRODUCTION

During recent years lasers have been intensively utilized as processing tools for the fabrication industry in a wide variety of applications. They have found applications in areas where conventional processing tools are not able to perform the work because of heat input, distortion, vacuum, or location. Although laser micromachining is gaining widespread acceptability it still produces results having a high variability in properties and quality. Therefore, it is very important to investigate the complex phenomena involved in laser micromachining, in order to control and optimize the overall qualities of the finished products.

In this chapter, an overview of laser micromachining will be presented in Section 2.1, including the state-of-the-art laser micromachining techniques used in microelectronics and packaging industry. Then, Section 2.2 will describe the methodologies utilized in this Dissertation. Finally, organization of the Dissertation will be presented in Section 2.3.

2.1. Overview

Laser micromachining is a part of laser materials processing. Laser materials processing consists of a large family of processes for material removing, or machining, heat treating, local surface modifications, etc. Laser micromachining can replace mechanical removal methods in many industrial applications, particularly in the processing of difficult-to-machine materials such as hardened metals, ceramics, and composites.

Laser machining is a thermal process (Webb, 1986). The effectiveness of this process depends on thermal properties and, to a certain extent, the optical properties rather than the mechanical properties of the material to be machined. Therefore, materials that exhibit a high degree of brittleness, or hardness, and have favorable thermal properties, such as low thermal diffusivity and conductivity, are particularly well suited for laser machining (Bertolotti, 1983).

Laser machining is a non-contact process. Since energy transfer between the laser and the material occurs through irradiation, no cutting forces are generated by the laser, leading to the absence of mechanically induced material damage, tool wear, and machine vibration. Moreover, the material removal rate for laser machining is not limited by constraints such as maximum tool force, built-up edge formation, or tool chatter.

Laser machining is a flexible process. When combined with a multi-axis workpiece positioning system or robot, the laser beam can be used for drilling, cutting, grooving, welding, and heat treating processes on a single machine. This flexibility eliminates transportation necessary for processing parts with a set of specialized machines. Also, laser machining can result in higher precision and smaller kerf widths or hole diameters than produced by comparable mechanical techniques (Chryssolouris, 1991).

In recent years, lasers have been widely used in manufacturing industry, especially in the fabrication of small components for electronics, aerospace, biomedical, MEMS, and other applications because they provide rapid, precise, clean, flexible, and efficient process (Steen, 2003). Some applications of state-of-the art laser materials processing include the pulsed Nd:YAG laser spot welding for the photonic devices (Marley, 2002), which utilized the laser for high precision joining and alignment. However, due to the physical movement of optical components that occurs during the resolidification phase of the laser microwelding process, post-weld shift (PWS) always exists and results in the component part shift towards the source of the heat for several hundred microns, as a result, controlling PWS and maintaining coupling efficiency has become a very challenging issue.

Laser materials processing is currently used in industry for an increasingly wide variety of tasks, and it has the advantages over conventional sources that it can be focused into a beam with a very high power density, and can be accurately controlled (McGeough, 2002). However, the mass and energy interchange phenomena involved in laser materials processing are extremely complicated, and high variability in properties and quality exist in the results of laser materials processing. Therefore, to utilize the advantages of laser processing and to achieve appropriate laser machining results, it is necessary to investigate further and to understand comprehensively the involved physical processes to a higher extent than for conventional machining, thus assist manufacturing industry in the design of new equipment needed to produce laser processed parts with good quality and reliability.

The primary concern, during laser interaction with metals, is the type of the interaction and the changes it produces in the material within and close to the region of the interaction. The requirements of knowledge before designing a laser based process include the selection of lasers, the beam delivery system, the interaction time between the laser beam and the workpiece, and the possible unwanted side effects. In addition, important requirements for lasers, which are used for materials processing, need to concern the sufficient power available at the workpiece, controlled focal intensity profile (hence well-characterized spatial mode), repeatability of the laser characteristics such as power, mode, polarization, pointing-stability, etc., reliability, and capital and running costs which are economic for the application (Ifflander, 2001).

In order to satisfy these requirements, the thermodynamics of laser heating should be addressed. This, however, is influenced by the optical and thermal properties of the workpiece, the laser beam characteristics, the dynamics of the irradiation process, and the phase change processes in the material. As could be expected, due to the complex physical phenomena involved in laser materials processing, exact solution of the process of laser beam interaction with metals is very difficult to obtain. To remedy this a number of studies have been carried out including the investigations of thermal field, thermalmechanical stress and deformation, fluid dynamics for the molten material, and plasma effect occurring during the short laser-material interaction period in order to obtain good understanding and reasonable approximation for laser materials processing.

2.2. Methodologies

In order to characterize the laser microdrilling and microwelding processes for the applications in microelectronics and packaging industry, analytical, computational, and experimental methodologies were utilized in this Dissertation. Analytical methodologies are characterized by exact closed form solutions and make use of infinitesimal elements. Computational methodologies make use of finite size elements in discretization of the physical domain and provide approximate solutions. Experimental methodologies employ, in general, actual objects subjected to real operating conditions, to provide information on responses of the objects to the applied loads.

More specifically, in this Dissertation, analytical approaches were utilized to develop the governing equations for the physical problems of laser materials processing, including heat transfer equations for temperature distributions of the workpiece under the high power density laser beam, the resultant thermomechanical stress and deformations, the plasma density which affects the absorption of the laser beam energy, etc. Computational approaches were utilized to solve the nonlinear equations in order to obtain approximation of the temperature and stress/deformation fields. Experimental approaches were utilized to investigate the effects of various operating parameters on the laser microdrilling and microwelding results. The combination of the analytical, computational, and experimental methodologies can help to gain thorough understanding of the physical phenomena that occur during laser materials processing, and it can lead to optimization and quality control for the processes involved.

2.3. Dissertation organization

The Dissertation is organized into seven chapters. Chapter 1 presents the objectives of this Dissertation. An introduction of this Dissertation is presented in Chapter 2, which includes the overview of laser micromachining processes, descriptions of the methodologies utilized in this Dissertation, and the organization of this Dissertation. Chapter 3 gives the background and literature review for the investigations of laser micromachining processes. Theoretical analyses are presented in Chapter 4, which first describes the general heat transfer problem occurring in laser micromachining, then discusses physical phenomena that occur in laser microdrilling and microwelding processes. The computational investigations of laser micromachining process are discussed in Chapter 5, which is composed of finite difference method to solve the governing heat transfer equation, development of computer interface for computing temperature profiles as well as the convection and radiation heat losses during laser micromachining, and calculations using finite element method and commercial software to solve for temperature, stress, and deformations for laser micromachining. The experimental investigations of laser microdrilling and microwelding processes are presented and discussed in details in Chapter 6. Individual laser parameters are investigated for their effects on laser microdrilling and microwelding processes, and the optimizations for the processes are proposed. In addition, correlations between computational and experimental results are performed and discussed in this chapter. Chapter 7 gives conclusions for the investigations conducted in this Dissertation, and some future works are proposed for further investigations of laser microdrilling and microwelding processes. Furthermore, Reference and appendixes are included at the end of this Dissertation as the supporting materials.

3. LITERATURE REVIEW

Since the invention of the laser in late 1950's, people have tried to use lasers for work with materials (Steen, 1991). During recent years lasers have become acceptable and reliable processing tools for the fabrication industry in a wide variety of applications (Haun, 1968). They have been extensively used in areas where conventional processing tools are not able to perform the work because of heat input, spot size requirements, or location.

Although laser materials processing has gained widespread acceptability, the mechanisms and main factors controlling the process remain controversial and need further theoretical and experimental studies. Thus, to utilize the advantages of laser processing and to achieve appropriate laser machining results, numerous investigations have been conducted to develop a thorough understanding of the physical processes involved. Traditional research efforts in the investigation of laser materials processing include three aspects: (1) theoretical studies, which are based on mathematical equations governing the fundamental physical phenomena such as heat transfer, phase transformation, fluid motion, plasma formation, thermomechanical stress/strain, etc., (2) numerical studies, which help solving the highly nonlinear partial differential equations (PDEs) from the theoretical studies, and (3) experimental studies, which were carried out to validate results of the theoretical and numerical studies.

A summary of results, based on theoretical and numerical studies, as found in available literatures is given in Section 3.1, while experimental results from literatures are summarized in Section 3.2.

3.1. Theoretical and numerical studies

Laser materials processing utilizes the high power density provided by the laser beam, which is focused on the workpiece. As a result, the workpiece material experiences heating, melting, and possible vaporization and re-solidification. Understanding the temporal evolution of the temperature field during laser material interaction is one of the most significant factors in achieving a desired quality of processing. The thermal history is required to determine dimensional changes in the machined part, the related stresses, phase transformations taking place, and the final metallurgical microstructures. Therefore, ability to determine the thermal field has been a major aspect of most models of laser micromachining.

For the general considerations of laser materials processing, a three-dimensional heat transfer model with a moving Gaussian heat source was developed using finite difference numerical techniques, which solved for temperature and melting profile in the workpiece of infinite length but finite width and depth (Mazumder and Steen, 1980). Another model solving for the melting depth profile and time evolution of the temperature was developed under the assumption that the process of laser heating and melting is a linear process, that is, the physical parameters of the material are independent of the temperature (Shen et al., 2000). In this study, one-dimensional heat conduction problem was solved approximately for a semi-infinite model in the solid and liquid regions, which gave the variation of the melt depth with time and temperature distributions in four materials: aluminum, titanium, copper, and silver.

The first one-dimensional model for evaporation dominated laser drilling was proposed in the late 1960s with the theory that material exposed to the laser beam is removed via evaporation (Ready, 1971). In 1976 Von Allmen proposed an alternative mechanism for material removal by indicating that surface evaporation in the area exposed to a laser beam induces recoil pressure, which ejects molten material (Von Allmen, 1976). This theory allowed order of magnitude estimation of drilling rates for microsecond and millisecond laser pulses, supporting the validity of the recoil pressure mechanism of material removal. A modified model was proposed later to include a more accurate calculation of melt front dynamics, which are usually treated in terms of the "problem of Stefan" (Anisimov and Khokhlov, 1995). Based on this approach, a new two-dimensional evaporation drilling model was proposed which predicted the temperature field in the beam interaction zone based on the assumption that no melt motion occurs. This assumption was proved to be valid if the absorbed beam intensity is sufficiently high that the material evaporates faster than it moves, and/or the interaction time is short enough that noticeable melt displacement cannot occur (Semak et al., 1997). However, with lower intensities or longer interaction times the evaporation recoil-pressure-induced melt flow can become an important transport mechanism. Calculations show that if the absorbed laser beam intensity is in the range of 5 to 10 MW/m^2 and the interaction time is higher than a threshold value (i.e., the intensity value at the onset of making the through hole), melt ejection from the interaction zone will be generated due to evaporation recoil pressure (Semak and Matsunawa, 1997). Furthermore, the latest development of the thermal considerations for laser drilling processes include the simulation of melting profiles using both Stefan conditions and the physical quantity enthalpy models, and the later method was proven to be more efficient in solving the problems with multiple phases (Verhoeven et al., 2003).

In addition to thermal considerations, laser materials processing involves several other complex phenomena, and laser-induced plasma is one of them; it significantly affects the absorption of laser beam energy (Herziger, 1986). At early stage, the kinetics of laser induced plasma, with its influence on absorption, was investigated giving indication that maximum efficiency and optimum quality only can be achieved in a narrow range of intensity (Herziger et al., 1986). A fundamental plasma based model for energy transfer in laser materials processing was the proposed, where the energy supply of a collision plasma with a low degree of ionization was considered, and the dominant energy transport process was found to be the release of kinetic and ionization energy of charged particles being absorbed and then recombining at the wall (Finke et al., 1990). A detailed three-dimensional model of laser induced plasma plume for laser welding using the CW CO_2 laser was developed, and the temperature, velocity, vapor concentration, absorption coefficient and the refractive index within the plasma plume were calculated, which were reasonably consistent with experimental data (Wang and Chen, 2003).

In most of the analytical and numerical investigations, the laser beam source was assumed to be at a circular cross section and of either uniform or Gaussian intensities at the surface. However, more detailed characteristics of the beam at its focus and its effect on the drilled hole profiles were studied by investigating beam divergence and aberrations at the focus and changing the size of the beam near the waist in the numerical models, which showed strong effect on the profile of the drilled holes (Olson and Swope, 1992).

A special category of laser materials processing is using ultra-short laser pulses, that is, the pulse lengths less than a nanosecond. When short pulses are used in laser materials processing, the electron kinetic theory needs to be employed to account for the electron-lattice atom collision, since the Fourier theory is no longer accurate due to omission of high-order terms in the representation of temperature profiles (Yilbas and Shuja, 1999). Therefore, the equations for non-equilibrium energy transport, thermal field, and thermal-mechanical analysis need to be derived based on a microscopic level consideration employing electron lattice site atom collisions (Yilbas and Arif, 2001). Furthermore, laser micromachining using high power, nanosecond pulsed excimer laser was investigated. It was found that explosive vaporization could occur when the laser influence is sufficiently high and the pulse length is sufficiently short, the temperature of the specimen could be raised to well above its boiling temperature. Numerical simulations of pulsed laser ablation were performed to validate the evaporation theories, based on the one-dimensional heat conduction model due to even distribution of the excimer laser over the target surface in a rectangular domain. Pulsed excimer laser ablation of nickel specimens was studied, focusing on properties of the laser-evaporated plume, which consisted of weakly ionized vapor and possible liquid droplets due to explosive phase transformations (Xu et al., 1999).

Laser welding processes offer great benefit over other welding processes, e.g., arc welding, resistance welding, etc., since less heat is coupled into the workpiece, resulting in a small heat affected zone (HAZ) and low distortion. The physical objectives desired in the process of laser welding of metals are several. Firstly, one should be able to carry out the welding processes avoiding the immediate onset of cracking of the welded specimen as well as the presence of damaging delayed fatigue effects, but additionally the welded joints should be subject to a minimum of distortion in the form of residual strains. In order to achieve a satisfactory study of the laser welding process, it is first of all necessary to know the temperature distributions resulting from the irradiation of the laser beam. The next step that must be addressed is to use the fundamental equations of linear thermo-elasticity to arrive at a knowledge of the distribution of stress in the elastic material under certain boundary conditions. Once a combined understanding of the temperature and stress distribution is achieved it is possible to identify domains in which the stresses may have a value above the yield point of the material at a given temperature, as well as regions where possible phase changes can occur for the particular material.

Numerical simulations of a laser welding process have been a major topic in welding research for several years. The results of simulations can be used to explain physical essence of some complex phenomena in the laser welding process explicitly and can be also used as the basis for optimization of the process. Simulations of the laser welding process enable estimation of transient stresses, residual stresses, and distortions. These can be used to evaluate structural misalignments and unexpected failures due to overstressing caused by the superposition of in-service loads and welding induced residual stresses. However, the simulation of the welding process is not an easy task since it involves interaction of thermal, mechanical, and metallurgical phenomena.

A number of analytical and numerical models of welding processes have been used to evaluate temperature and stress distribution during the welding process, as well as corresponding residual stresses and final distortions of structural components. These include analytical models (Yang and Xiao, 1995), two-dimensional finite element models (Fujii et al., 2000), and three-dimensional finite element models (Frewin and Scott, 1999). However, not all of parameters influencing the welding process, including microstructural changes due to phase transformation, heat flux simulation, and variation of thermal and mechanical material properties with temperature, were taken into account in the simulations listed above. Recently, a three-dimensional finite element model was developed for the butt-joint specimen that consisted of thick AH36 shipbuilding steel plates, considered a Gaussian distribution of heat flux with a moving heat source, the quasi-steady-state thermal solution, temperature dependent material properties, and metallurgical transformations (Tsirkas et al., 2003). Furthermore, for laser micromachining applications, the possibilities of using laser beam to produce welds of micrometer size were discussed, and a theoretical criterion defining the threshold pulse energy and beam intensity required for melt displacement (necessary for penetration-mode welding or drilling) was proposed, with the supportive numerical and experimental verifications (Semak et al., 2003).

For the study of stress distributions in laser welding process, early researches include the consideration of the thermoelasticity problem due to a moving heat source (Nowacki, 1962), development for the transient surface stress and displacement due to line heat sources in terms of Bessel functions (Barber, 1984), and the calculation of thermal stresses on an infinite slab caused by a moving square heat source on the surface (Sumi et al., 1987). More recently, an analytical solution for a semi-infinite plane subjected to a moving Gaussian heat source was obtained in terms of Bessel functions and exponential integrals (Sheng and Chen, 1991). An explicit formula for the shape of the deformed target surface under laser irradiation was obtained as a function of the deposited Gaussian energy distribution (Vicanek et al., 1994). Furthermore, the numerical model of the thermal stresses generated by a moving elliptical weld pool in the welding of thin metal sheets were developed (Postacioglu et al., 1997), and the stresses along the weld direction and the distortion of the workpiece from the laser welding process were evaluated using a Mellin-transform technique, where the considerations were restricted to the plane linear thermoelastic model in order to obtain the basic mathematical formula for the transient change in stresses, and the final results were expressed in terms of a convolution integral and illustrated by numerical calculations for the point heat source (Dain et al., 1999). The latest investigations include the transient thermal and stress analyses of a laser spot-welded joint using nonlinear finite element method, and since the study was limited to the thermoelastic stresses, it was found that the stresses and deformations were overestimated (Apalak et al., 2003).

During a laser welding process, a liquid pool of molten material is formed. Shape of this pool is affected by the thermocapillary convection. A lot of work has been done to understand the convection processes and free-surface deformations of the weld pools. The importance of convection in analysis of the weld pools was realized as early as 1947 (Shaeffler, 1947). A two-dimensional model was later developed to study temperature distribution and convection due to buoyancy, electromagnetic, and surface tension forces in arc weld pools (Oreper et al., 1983). A three-dimensional perturbation model was then developed to examine the effects of thermocapillary convection in laser melted pools (Chan et al., 1988). The above-mentioned studies were based on the assumption that the free surface of the melt pool was flat. Then a two-dimensional transient model for laser welding was developed to determine the shape of the free surface and found that the free-surface bulges upward under the beam at the pool center and near the solid-liquid interface, and the pool has a depression between these two regions (Paul and Debroy, 1988). These studies were concerned with a very small deformation of the weld pool free surface. During key-hole welding, a large deformation of the free surface is encountered due to the formation of a vapor and plasma-filled cavity, and the model of dynamic behavior of the keyhole was developed taking considerations of the fluid flow in the molten region (Kroos et al., 1992; Ducharme et al., 1994; Martin et al., 2001).

3.2. Experimental studies

Most of the analytical and computational investigations were accompanied by experimental verification for the temperature profiles, melting mechanisms, and stress determinations. However, from the practical point of view, it is the end product of the laser micromachining, for instance a drilled hole or a laser welded workpiece, that matters. Therefore, to utilize the laser beam for micromachining, various factors must be considered and evaluated in order to characterize the quality of resulting product. Major concerns in evaluating the laser micromachined workpiece are taper, circularity, barreling, spatter formation, strength, grain structure modification, and residual stresses. In addition, the repeatability is always critical in laser micromachining applications. In the experimental studies, the major factors include laser pulse energy, pulse length, focus settings, and the workpiece thickness and thermal properties. Effective utilization of the laser depends very much upon proper selection and optimization of all these factors. However, the experimental investigations usually have the disadvantage that, only several parameters can be studied for some specific materials and processing applications, and the results are usually based on statistical data. Therefore overall optimization is difficult to obtain because of various materials and processing procedures.

Early experimental investigations include a statistical method to investigate the effects of variation of a single pulse laser drilling parameters on the hole geometry of Nimonic 75 workpiece material (Yilbas and Yilbas, 1987), and a factorial design to identify the effects of a single pulse drilling on the hole quality, including resolidified material, taper, barreling, inlet cone, exit cone, surface debris and mean hole diameter (Yilbas, 1987). Temperature variations were measured during laser microdrilling processes and the data were correlated to numerical results based on the fundamental thermal analysis (Han, 1999). The effects of assist gas on the physical characteristics of spatter formation during laser percussion drilling on NIMONIC 263 alloy were investigated, O_2, Ar, N_2, and compressed air were selected, and the influence of the assist gas type on the mechanism of material ejection/removal was reported (Low et al., 2000). The effect of laser peak power and pulse width on the repeatability of hole geometry was studied for pulsed Nd:YAG laser drilling on 2 mm thick mild steel sheets (Ng and Li, 2001), and the characteristics of spatter formation under the effects of different laser parameters were investigated for laser drilling on NIMONIC 263 alloy sheets (Low et al., 2001). Six controllable laser variables were studied for the effect on hole taper and circularity in laser percussion drilling on stainless steel workpiece (Ghoreishi et al., 2002). Latest study include the investigations of the effect of systematic parameters on the resultant profiles of the holes for laser drilling of micrometer size holes on thin metal sheets, with the supportive analytical and computational characterizations of the thermal problems occur in laser microdrilling processes (Han et al., 2004).

For detailed investigations of laser drilling mechanism, melt ejection during laser drilling of metals were characterized and validated by experimental observations, and the particle size distribution, angle of trajectory, molten layer thickness and temporal variation of melt ejection were determined (Voisey et al., 2003).

For the applications of ultra fast lasers, the efficiency of laser ablation was studied by measuring the size of the crater for ultra-fast laser ablation, and femtosecond pulse was found to have the best efficiency, since in this regime, the laser beam cannot interact with the plasma, whereas in ns and ps regimes the plasma shielding can occur (Chaleard et al., 1986). For pulse durations larger than the typical relaxation time, i.e., for pulse lengths exceeding 10^{-6} s, the ablation rate grows with the pulse duration.

The effect of laser welding parameters on fusion zone shape and solidification structure of austenitic stainless steels were investigated, focused on the effect of workpiece thickness, laser peak power, welding speed, and defocusing distance, indicating that control of the welding parameters was very critical in order to obtain complete penetration, minimum fusion zone size, and acceptable weld profiles (El-Batahgy, 1997). The keyhole shapes were investigated in experiments for the effects of laser spot diameter, its intensity distribution, defocus, and welding speed (Jin and Li, 2003). For laser welding of a metal workpiece, reflectivity on the surface is usually of a high value. A number of investigations of the reflection of laser beams by metal surfaces for laser welding were carried out, mostly on polished surfaces. Some experimental data for reflectivity values for both CO_2 and Nd:YAG lasers were presented and compared with theoretically calculated values, which indicated that although reflectivity was quite high for polished metals, it decreased with an increase in temperature (Duley, 1985). Laser welding on thin sheet steel with surface oxidation was studied, and it was found that surface oxidation enhances the absorption of laser energy significantly and has little influence on the mechanical properties of laser welds (Xie and Kar, 1999). In order to evaluate the quality of laser welds, strength was tested and compared with the results from resistance welding, and it was found that the weld strength of laser spot welds was greater than that of resistance spot welds, and the joint strength of the laser spot welds depended on the weld joining area and the maximum diameter (Yang and Lee, 1999). Furthermore, a non-destructive measurement technique was developed and utilized to measure thermal deformations of the laser microwelds based on optical methodology, which provides quantitative real-time whole field of view imaging, and allows measurements of displacements and deformations with sub-micrometer accuracy for microelectronics and packaging applications (Han and Pryputniewicz, 2003b).

For the investigations of the formation and propagation of the laser-induced plasma plume during laser materials processing, high-speed holographic interferometry was applied for visualizing and imaging the refractive index distribution of the plasma plume and vaporized metal, which provided the feasibility of quantitative measurement of the density distribution of the laser-induced plume and vaporized metal in laser welding (Baik et al., 2001).

4. THEORETICAL ANALYSIS

The goal of this chapter is to present a model of laser beam interaction with metals.

Section 4.1 presents the general model for the laser processing of materials. The governing equation, of this three-dimensional heat transfer problem, is developed, boundary conditions are discussed, and exact analytical solution of the resulting partial differential equation is presented.

Section 4.2 considers the physical phenomenon of laser drilling, including the considerations of material removal mechanisms, threshold intensity of laser drilling, and moving boundary problem during laser melting.

Section 4.3 considers the mechanisms for laser welding, including the thermal stresses and deformations involved in the laser processing, and weldability of different materials.

Section 4.4 includes pertinent theoretical considerations, such as properties of laser beams, calculation of energy needed for laser micromachining, phase change during laser micromachining, plasma effect during laser micromachining, assisting gas effects, and the influence that variation in surface emissivity has on the results of laser micromachining processes.

4.1. General heat transfer problem for laser materials processing

Analysis of the interaction of a laser beam with a workpiece is based on development of a three-dimensional model for the geometry shown in Fig. 4.1.

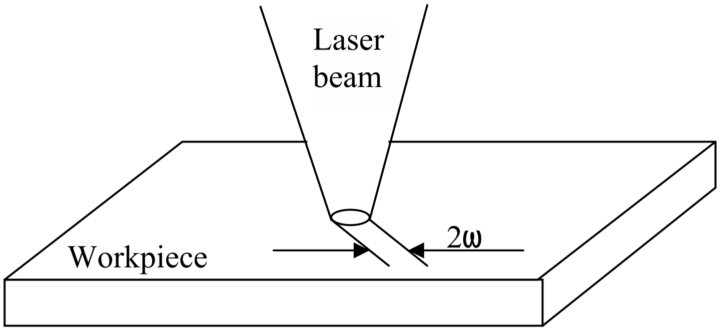

Fig. 4.1. Laser beam impinging on a workpiece of a finite size.

The geometry considered in this Dissertation is a finite, rectangular workpiece irradiated by a laser beam impinging on its surface and subjected to convection and radiation heat losses. The laser beam is characterized by its wavelength λ, the beam spot radius ω at the surface, and the power density I within the spot.

4.1.1. Governing equation

Based on the first law of thermodynamics, the equation for heat flow in a three-dimensional solid can be written as (Dowden, 2001; Pryputniewicz, 1998)

$$\rho \frac{\partial}{\partial t} \int_{T_0}^{T} c(T)\,dT = \frac{\partial}{\partial x}\left[k(T)\frac{\partial T}{\partial x}\right] + \frac{\partial}{\partial y}\left[k(T)\frac{\partial T}{\partial y}\right] + \frac{\partial}{\partial z}\left[k(T)\frac{\partial T}{\partial z}\right] + Q(x,y,z,t) \quad , \qquad (1)$$

where ρ is the density of the material of the workpiece, $c(T)$ is the temperature dependent specific heat of the material, $k(T)$ is the temperature dependent thermal conductivity, $Q(x, y, z, t)$ is the rate at which heat is supplied to the solid per unit time per unit volume, $T = T(x, y, z, t)$ is the resulting three-dimensional time dependent temperature distribution in the material, t is time, T_0 is the initial temperature, and x, y, z are the spatial Cartesian coordinates. For certain applications, it can be assumed that $k(T)$ and $c(T)$ do not change dramatically with temperature. Therefore, assuming constant specific heat and thermal conductivity for a particular time interval, Eq. 1 can be simplified to

$$\rho c \frac{\partial T}{\partial t} = k \nabla^2 T + Q \quad . \tag{2}$$

4.1.2. Boundary conditions

The workpiece experiences a combination of three kinds of heat transfer processes: conduction, convection, and radiation. The convection and radiation occur only on the boundary of the workpiece.

The convective heat loss per unit area of the surface of the workpiece due to the external-flow conditions can be expressed as

$$q_c = h_c (T - T_{amb}) \quad , \tag{3}$$

where q_c is the convection heat flux, h_c is the convective heat transfer coefficient, T is the temperature of the workpiece, and T_{amb} is the ambient temperature.

In order to determine h_c, the characteristic length L of the workpiece should be defined, i.e.,

$$L = \frac{A}{p} \quad , \tag{4}$$

where A is the area of the surface, and p is the perimeter of the workpiece. Then, the Nusselt number for the horizontal plate is (Bejan, 1993)

$$N_u = 0.27 \cdot R_a{}^{0.25} \quad , \tag{5}$$

where the Rayleigh number R_a is

$$R_a = \frac{g\beta}{\kappa\gamma} L^3 (T - T_{amb}) \ . \tag{6}$$

In Eq. 6, g is the gravitational acceleration, β is the coefficient of volumetric thermal expansion, κ is the thermal difffusivity, γ is the kinematic viscosity, L is the characteristic length, and other parameters are as defined for Eq. 3. The convective heat transfer coefficient, h_c, can be calculated as

$$h_c = N_u \frac{k_{air}}{L} \quad , \tag{7}$$

where k_{air} is the thermal conductivity of the air surrounding the workpiece.

The heat flux per unit area caused by radiation, q_r, is

$$q_r = \varepsilon\sigma(T^4 - T_{amb}{}^4) \quad , \tag{8}$$

where ε is the emissivity of the material, and σ is the Stefan-Boltzmann constant.

4.1.3. Analytical solution

To gain an insight into processes governing interaction of laser beams with metals, solution of Eq. 1 was examined subject to specific simplifying considerations. These considerations, at this time, are limited to the assumptions that the laser beam is uniformly distributed over a circular area of radius ω on the surface of a workpiece, and that the laser power P equals P_0 at time greater than 0, i.e., $P = P_0$ when $t \geq 0$. Then, using cylindrical coordinates, it can be shown (Carslaw and Jaeger, 1969) the temperature distribution is

$$T(r,z,t) = \frac{\varepsilon P_0}{2\pi\omega k}\int_0^\infty \frac{d\lambda}{\lambda} J_0(\lambda r) J_1(\lambda\omega)\left\{ e^{-\lambda z} erfc\left[\frac{z}{2(\kappa t)^{0.5}} - \lambda(\kappa t)^{0.5}\right] \right. \\ \left. - e^{\lambda z} erfc\left[\frac{z}{2(\kappa t)^{0.5}} + \lambda(\kappa t)^{0.5}\right]\right\} \quad . \tag{9}$$

In Eq. 9, r is the radial coordinate, z is the axial coordinate, t is time, J_0 and J_1 are Bessel functions of the first kind, P_0 is the constant power during a laser pulse, λ is the wavelength of the laser beam, ω is the radius of the laser spot at the surface, k is the thermal conductivity of the material, κ is the thermal diffusivity, ε is the thermal emissivity of the surface of the workpiece, and the relationship between the error function *erf* and the complementary error function *erfc* is defined as (Carslaw and Jaeger, 1969)

$$erfc(x) = 1 - erf(x) = \frac{2}{\pi}\int_x^\infty e^{-u^2}\, du \quad , \tag{10}$$

where x is the independent variable, and u is the dummy variable.

4.2. Laser drilling

Laser drilling has become a significant industrial process, because there are many outstanding advantages in using it as the fabrication method of small holes over other techniques. Laser drilling is a very complex process, since both melting and vaporization are encountered, and the phenomena such as fluid flow, gas dynamics, and plasma effects are involved. During laser drilling, material is removed via vaporization and physical ejection of molten material. For melt ejection to occur, a molten layer must form and the pressure gradients acting on the surface due to vaporization must be sufficiently large to overcome surface tension forces and expel the molten material from the hole.

One major application of laser drilling is making holes for combustors and turbines in aircraft jet engines. The holes are used for cooling purposes, where a cool air stream is either mixed with the hot combustion gases or directed to maintain the flame tube and turbine blade surfaces at a desired temperature. Since the combustor and turbine are usually made from tough heat-resistant alloys, mechanical drilling methods are both expensive and time-consuming. Therefore, aerospace manufactures have turned to non-electro-discharge machining methods, such as laser machining, electro-chemical machining, performed on combustors using Ruby, Nd:Glass, and Nd:YAG lasers. The lasers were operated in a pulsed mode with pulse frequencies less than 10 Hz and pulse energy between 10 J and 40 J. The results showed a degree of asymmetry in the hole profile, a significant layer of resolidified material, and formation of microcracks near the hole. A trepanning method, where the laser beam is moved in a circular motion along the plane of the workpiece to produce a hole, can also be used in conjunction with a pulsed

Nd:YAG beam operating at 300 Hz. The trepanning method produces holes by controlling the relative motion between the workpiece and the laser beam; using this method, non-circular hole geometry can also be produced (Chryssolouris, 1991).

A schematic of features of laser-drilled holes is shown in Fig. 4.2. Barrelling is the effect of energy trapped inside the workpiece to form a cavity, the formation of the barrel can guide the ejected material as it passes through the hole, forcing the molten material around the hole to come away from the sides. Resolidified material indicates the amount of material that had vaporized or melted during drilling, but had not escaped from the hole and so had resolidified on the internal surface. Taper is the measure of overall taper of the hole sides, but does not include inlet and exit cones. The surface debris is an assessment of the amount of resolidified materials appearing on the surface of the hole. The inlet and the exit cones are the measure between the entrance and minimum hole diameters and the measure between the minimum and exit hole diameters, respectively, and usually the inlet cone has a bigger value than the exit cone.

Although lasers have been intensively used for drilling applications, quality of the laser drilled holes still has high variations from desired results. Control of the drilling process for a given workpiece materials is accomplished through selection of beam power, focal spot size, and drilling time. Laser drilling can be performed through continuous drilling, with the use of a continuous-wave beam, or percussion drilling, with the use of a pulsed beam. In continuous drilling, material removal occurs through bottom of the hole with the aid of a gas jet. In percussion drilling, a pulsed beam removes

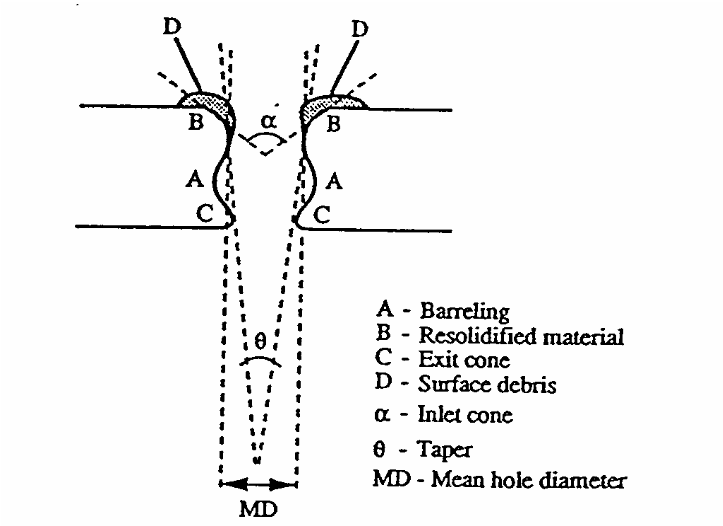

Fig. 4.2. Features of laser drilled holes.

material through melting and localized detonation or explosion. In this case, about 90% of the material is removed through detonation effects. Additionally, a reactive gas jet can be used to remove material through oxidation, chemical reactions, etc. (Tiffany, 1985).

In Section 4.2.1, a simple one-dimensional model ofr laser drilling is presented, including the discussion of temperature distributions and melting velocity. Then, in Section 4.2.2, detailed moving boundary problem during the melting period is illustrated. Finally, material removal mechanisms are discussed in Section 4.2.3.

4.2.1. One-dimensional model for laser drilling

Drilling can be divided into two stages: heating and material removal, Fig. 4.3. In the heating stage, temperature of the workpiece surface, T_s, is increased up to the phase transition temperature, T_m, by a laser beam. The heating stage is usually very short because the laser beam intensity is very high. In the material removal stage, the hole depth is increased through molten material removal.

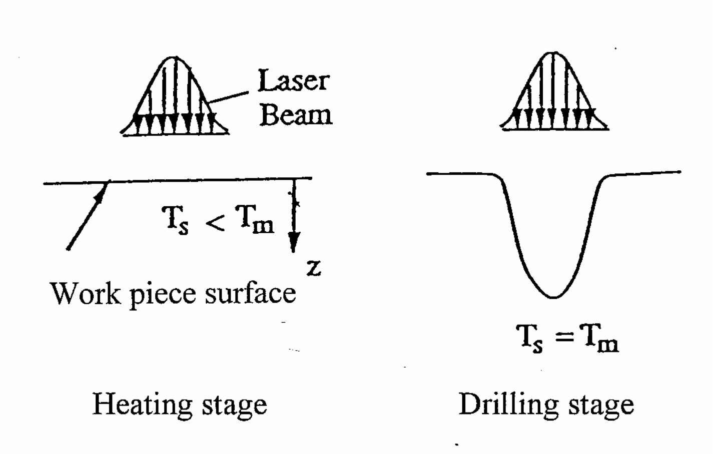

Fig. 4.3. Heating and material removal stages of laser drilling.

During the heating stage, the workpiece surface is not thermally eroded. It is difficult to obtain a simple analytical solution for drilling as a non steady process with three-dimensional heat transfer characteristics. Thus, it is assumed that drilling is a one-dimensional process and that the laser beam intensity is uniform. The boundary conditions are

$$\text{at } z = 0, \qquad -k\left(\frac{dT}{dz}\right)_{z=0} = I_0 , \tag{11}$$

$$\text{at } z \to \infty, \qquad T = T_0 , \tag{12}$$

where I_0 is the laser beam intensity, and T_0 is the initial temperature.

For the boundary conditions given by Eqs 11 and 12, the temperature distribution inside the workpiece can be derived, based on Eq. 2, to be (Chryssolouris, 1991)

$$T - T_0 = \frac{2I_0}{k}\left(\frac{\kappa t}{\pi}\right)^{1/2} e^{\frac{-z^2}{4\kappa t}} - \frac{I_0 z}{k}\left(1 - erf\frac{z}{2(\kappa t)^{1/2}}\right), \tag{13}$$

where κ is the thermal diffusivity and I_0 is the laser beam intensity. The temperature distribution given by Eq. 13 is valid under the condition that $(\kappa t)^{1/2} < \omega$, which can be achieved either through low diffusivities or short drilling times. The time for the workpiece surface to reach the solid-liquid phase transition temperature T_m can be determined from Eq. 13. Applying $T = T_s$ at $z = 0$, the following relation can be obtained:

$$T_m - T_0 = \frac{2I_0}{k}\left(\frac{\kappa t}{\pi}\right)^{1/2} . \tag{14}$$

The duration of the heating stage, t_h, can be calculated as

$$t_h = \frac{\pi}{\kappa}\left[\frac{k(T_m - T_0)}{2I_0}\right]^2 . \tag{15}$$

During the heating stage, a hole is not made because phase transition does not occur. After the surface temperature reaches the melting point, drilling starts.

In order to determine the hole depth as a function of time and process variables, a one-dimensional analysis is considered, Fig. 4.4. A laser beam is assumed to have a uniform intensity distribution I_0 defined as $I_0 = \frac{P}{\pi\omega^2}$.

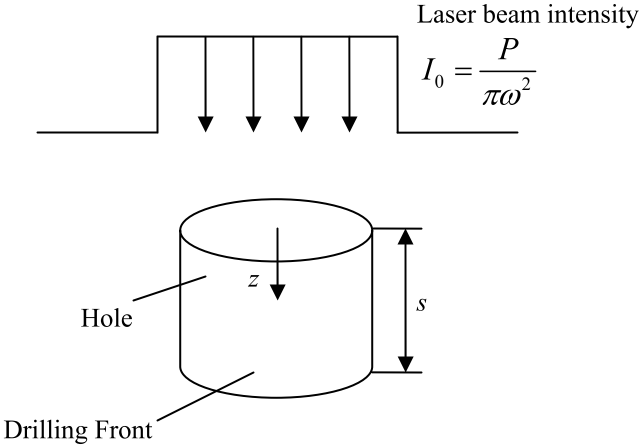

Fig. 4.4. One-dimensional drilling.

The energy balance at the drilling front can be expressed as

$$\alpha I_0 = \rho L_m \frac{\partial s}{\partial t} - k\left(\frac{dT}{dz}\right)_{z=0} , \tag{16}$$

where α is the absorptivity of the material, ρ is the density, L_m is the latent heat of fusion, k is the thermal conductivity, and T is the temperature. In order to determine the drilling velocity $\frac{\partial s}{\partial t}$, the temperature gradient at the drilling front should be known. The temperature distribution inside the solid is governed by the heat conduction equation

$$\frac{1}{\kappa}\frac{\partial T}{\partial t} = \frac{\partial^2 T}{\partial z^2} , \tag{17}$$

where κ is the thermal diffusivity. Equation 17 can be rewritten as

$$-\frac{1}{\kappa}\left(\frac{\partial s}{\partial t}\right)\frac{dT}{dz} = \frac{d^2 T}{dz^2} . \tag{18}$$

The boundary conditions are

at $z = 0$, $\qquad T = T_m$, (19)

at $z \to \infty$, $\qquad T = T_0$. (20)

By applying the boundary conditions given by Eqs 19 and 20, Eq. 18 can be solved for the temperature distribution inside the solid as

$$\frac{T - T_0}{T_m - T_0} = \exp\left[-\frac{1}{\kappa}\left(\frac{ds}{dt}\right)z\right] . \tag{21}$$

The temperature gradient at the drilling front can be determined, using Eq. 21, to be

$$\left(\frac{dT}{dz}\right)_{z=0} = -\frac{1}{\kappa}\left(\frac{ds}{dt}\right)\left(T_m - T_0\right) . \tag{22}$$

Substitution of the temperature gradient into the energy balance, given by Eq. 16, yields

$$\alpha I_0 = \rho L_m\left(\frac{ds}{dt}\right) + \rho c\left(\frac{ds}{dt}\right)\left(T_m - T_0\right) . \tag{23}$$

Using Eq. 23, the drilling velocity can be expressed as

$$\frac{ds}{dt} = \frac{\alpha I_0}{\rho\left[L_m + c\left(T_m - T_0\right)\right]} . \tag{24}$$

The hole depth can be determined by integrating Eq. 24

at $t \le t_h$, $\qquad s = 0$, (25)

at $t > t_h$,

$$s = \frac{\alpha I_0 (t - t_h)}{\rho (L_m + c(T_m - T_0))} = \frac{4 \alpha P (t - t_h)}{\pi \omega^2 \rho (L_m + c(T_m - T_0))} \quad . \tag{26}$$

Equation 26 shows that the hole depth is proportional to the laser beam power and the beam interaction time (Chryssolouris, 1991).

For laser percussion drilling processes of metals, drilling efficiency is strongly dependent on the phenomenon of laser-supported detonation waves. Plasma formation at the workpiece surface due to laser/material interaction severely decreases laser drilling effectiveness because it absorbs a significant portion of the incoming beam energy and shields the workpiece surface. A laser-supported detonation (LSD) wave occurs when the absorbing plasma layer is coupled to a shock wave occurring when material at the erosion front detonates. This transient phenomenon propagates the wave effects which can be minimized by using a shorter focal length lens, by increasing the beam intensity and by using a low density gas jet such as He instead of air. By minimizing the LSD wave effect, holes up to 65 mm in depth can be drilled in copper workpieces using energy densities between 300 J/cm^2 and 6000 J/cm^2 (Yu et al., 1998).

4.2.2. Energy transport in multiple phases

The physical model of the melting front at the initial stage of drilling is shown in Fig. 4.5. Evaporation from the surface molten material causes melt surface shift into the material with velocity v_v, which is directed normal to the melt surface. The temperature of the melt surface is different in different locations. Therefore, the evaporation rate and the related recoil pressure on the melt surface vary along the surface. In particular, the values of pressure at the opposite sides of the discretized finite element, p^{in} and p^{out}, are different. This causes the melt flow shown in Fig. 4.5. Because the melt flow accelerates or decelerates depending on the relative values of p^{in} and p^{out}, and the cross sections of the finite element volume at the flow entrance and exit are different, the quantities of melt entering and leaving the computational volume are not generally the same. Therefore, the melt thickness h decreases or increases, resulting in the motion of the melt surface with velocity v_m, which, like v_v, is normal to the melt surface. Note that the evaporation component of the melt surface velocity, v_v, is always directed into the sample, while the component of the melt surface velocity due to melt flow, v_m, can be directed either into the sample or in the opposite direction. The resulting velocity of the melt surface, v_d, the "drilling" velocity, is the sum of the two components, i.e.,

$$v_d = v_m + v_v\,. \tag{27}$$

Assuming incompressible liquid in the melt layer, independent thermophysical properties of the temperature for the workpiece material, and surface heat source for the laser power, the equations of conservation of mass, momentum, and energy can be written as

$$\operatorname{div} v = 0 \quad , \tag{28}$$

$$\rho\left(\frac{\partial v}{\partial t} + v\operatorname{grad}v\right) = -\operatorname{grad}p + \mu\Delta v \quad , \tag{29}$$

$$\frac{\partial T}{\partial t} + v\operatorname{grad}T = \frac{k}{c\rho}\nabla^2 T \quad , \tag{30}$$

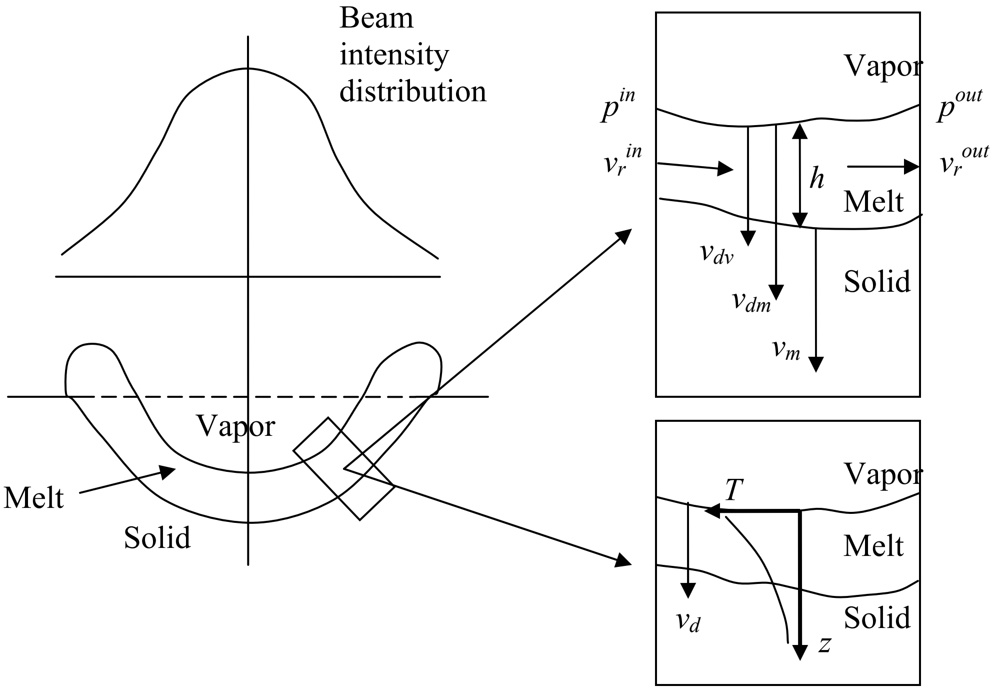

Fig. 4.5. Schematic of energy transport in multiple phases in laser drilling.

where v, ρ, c, T, and k are the velocity, density, specific heat, temperature, and thermal conductivity of solid or liquid material, μ is the melt viscosity, and p is pressure. The boundary condition at the liquid-vapor interface is

$$-k\frac{\partial T}{\partial z}\Big|_s + \rho v_v L_v = (1-R)I_s \quad , \tag{31}$$

where k is thermal conductivity of the solid or liquid phase, $\frac{\partial T}{\partial z}\Big|_s$ is the temperature gradient at the surface along the normal (z axis), ρ is the density of the solid or liquid phase, v_v is the component of boundary velocity due to evaporation, R is the reflectivity for the laser wavelength, and I_s is the intensity of the laser beam at the surface. For surface temperatures less than approximately half of the critical temperature the energy of evaporation per atom, U, can be assumed to be constant. Then the component of the boundary velocity due to evaporation v_v can be expressed by

$$v_v = V_0 \exp\left(\frac{-U}{T_s}\right) \quad , \tag{32}$$

where V_0 is a coefficient of the order of magnitude of the sound velocity, U is the energy of evaporation per atom, and T_s is the surface temperature.

The classic Stefan boundary condition is applied to the solid-liquid boundary (melting front $z=z_m$)

$$\rho L_m v_m = k_s \frac{\partial T_s}{\partial z}\bigg|_{z=z_m} - k_l \frac{\partial T_l}{\partial z}\bigg|_{z=z_m} \quad , \tag{33}$$

where L_m is the latent heat of melting, v_m is the melting front velocity, and subscripts "*s*" and "*l*" represent "solid" and "liquid", respectively. The Stephan boundary condition assumes an instant transition from solid to liquid at the melting temperature, T_m, and does not allow superheating at the melting front. The approximation is adequate for the slow velocities of melt front propagation typical of laser welding and drilling, where the melting kinetics can be disregarded.

Assuming the melt layer is a thin boundary layer, it allows one to model the melt flow using quasi-one-dimensional equations in conservative form, represented by a modification of the St. Venant equation for incompressible open-channel flow for the case of mass source due to melting and mass sink due to evaporation, i.e.,

$$\frac{\partial(h)}{\partial t} + \frac{1}{r}\frac{\partial(r v_r h)}{\partial r} = -v_v + v_m \quad , \tag{34}$$

$$\frac{\partial(v_r h)}{\partial t}+\frac{1}{r}\frac{\partial}{\partial r}\left[r\left(h{v_r}^2+\frac{ph}{\rho}\right)\right]=\frac{p}{\rho}\left(\frac{1}{r}\frac{\partial h}{\partial r}\right)+\frac{h{v_r}^2}{r}-(v_v-v_m)v_r-\frac{\mu}{\rho}\frac{v_r}{h} \quad , \tag{35}$$

where r is the direction along the melt surface, z is the direction normal to the melt surface, h is the melt thickness, v_r is the radial melt flow velocity averaged over the melt layer thickness, and μ is the melt viscosity. The second term on the right-hand side of Eq. 35 represents deceleration/acceleration due to mass addition/loss determined by the combined effect of melting and evaporation. The third term on the right-hand side of Eq. 35 represents effect of melt viscosity.

From Eq. 34 one can easily see that the second term on the left-hand side and the first term on the right-hand side represent the components of melt surface velocity determined by melt ejection, v_m, and melt evaporation, v_v, respectively. Thus the velocity of the melt surface, or the "drilling" velocity, v_d, is given by

$$v_d=-\frac{1}{r}\frac{\partial(rv_r h)}{\partial r}-v_v=-v_m-v_v \quad . \tag{36}$$

Application of the thin boundary layer assumption allows the pressure across the molten layer to be approximated by the evaporation recoil pressure, p_r, applied to the melt surface. It can be shown that the evaporation recoil pressure at the surface is related to the surface temperature, T_s, according to the equation

$$p_r=AB_0{T_s}^{-1/2}\exp\left(\frac{-U}{T_s}\right) \quad , \tag{37}$$

where A is an ambient pressure dependent coefficient in the range 0~0.54, and B_0 is the evaporation constant.

Taking into consideration the radial motion of the melt with an average velocity v_r determined by Eqs 34, 35, and normal to the melt surface motion of the melt-vapor interface with velocity v_d determined by Eqs 32, 35, and 36, one can write the heat transfer equations for the liquid and solid phases in the following form (Semak et al., 1999):

$$\frac{\partial T}{\partial t} + v_r \frac{\partial T}{\partial r} + v_d \frac{\partial T}{\partial z} = \frac{k_l}{\rho_l c_l}\left(\frac{\partial^2 T}{\partial r^2} + \frac{\partial^2 T}{\partial z^2} + \frac{1}{r}\frac{\partial T}{\partial r}\right) , \tag{38}$$

$$\frac{\partial T}{\partial t} + v_d \frac{\partial T}{\partial z} = \frac{k_s}{\rho_s c_s}\left(\frac{\partial^2 T}{\partial r^2} + \frac{\partial^2 T}{\partial z^2} + \frac{1}{r}\frac{\partial T}{\partial r}\right) , \tag{39}$$

where the subscripts "*l*" and "*s*" refer to the liquid and solid phases and ρ, c, T, and k and the density, specific heat, temperature and heat conductivity, respectively.

Combining Eqs 34, 35, 38, and 39 with the boundary conditions in Eqs 31 and 33, the transient model of the propagation of the melt layer can be established (Semak et al., 1999).

4.2.3. Material removal mechanism

The energy balance within the interaction zone between the laser beam and workpiece is the key point in modeling laser material processing, especially for laser machining on metals, losses due to high reflectance and greater thermal conductivity are significant. The laser parameters have to be balanced in metal drilling to the material properties like absorptivity and thermal diffusivity. The drilling process is influenced by melt expulsion, absorption, and refraction of laser radiation in the expanding vapor plasma. Figure 4.6 shows a block diagram for various processes of material removal and their mutual influence for laser drilling.

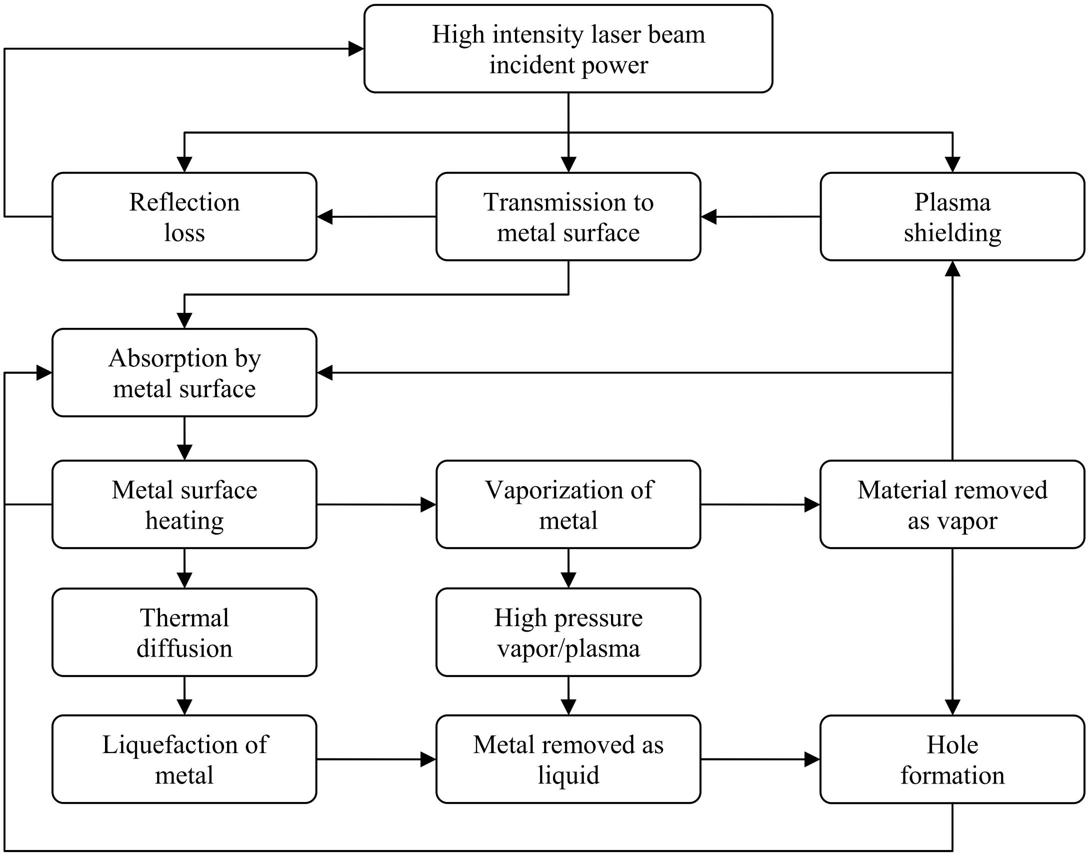

Fig. 4.6. Block diagram for the main processes of material removal and their mutual influences during laser drilling.

The metal surface is heated by the absorbed laser power up to the melting point and after a phase change finally to the vaporization temperature. The reflected radiation from the metal surface can influence the laser output via optical feedback. The threshold intensity, I_v, for material removal is determined by the losses due to surface reflection and heat conduction into the material. The threshold is a function of beam radius, w_0, at the metal surface, the processing time, t_p, the absorption coefficient, A, and the thermal diffusivity of the metal, κ. For a Gaussian intensity distribution the threshold intensity I_v is given by (Treusch and Herziger, 1986)

$$I_v = \frac{T_v k \sqrt{2\pi}}{A w_0 arctg \sqrt{8\kappa t_p / w_0^2}} \quad , \tag{40}$$

where T_v is the vaporization temperature, and k is thermal conductivity of the workpiece material.

Laser drilling is a material removal process, which has two major mechanisms of removal of material from the beam interaction zone and consequent propagation of the melt front into the metal bulk. They are: (1) melt evaporation (for high-power or short-pulse-duration drilling), (2) melt ejection by the vaporization-induced recoil force (for general cutting, welding, and drilling) (Semak and Matsunawa, 1997). The vaporization mechanism of melt removal can be the dominating mechanism for lower laser powers and consequently lower melt-surface temperatures in the case of short laser pulses, for which, due to inertia, the melt cannot be ejected from the interaction zone before its solidification. For higher melt surface temperatures generated either by higher absorbed laser intensities or by exothermic reaction with a chemically active assisting gas, such as oxygen, the vaporization recoil pressure becomes the primary factor removing melt from the interaction zone under the regime of hydrodynamic mechanism.

Among the two material removal mechanisms during laser drilling, that is, material removal via vaporization and physical ejection of molten material, melt ejection is a very efficient way since the latent heat of vaporization does not need to be absorbed when melt ejection occurs. For melt ejection to occur, a molten layer must form and the pressure gradients acting on the surface due to vaporization must be sufficiently large to overcome surface tension forces and expel the molten material from the hole. The energy required to remove material via melt ejection is about one quarter of that required to vaporize the same volume.

Detailed explanation of the melt ejection process in single pulse laser drilling is as following. Immediately after the start of the laser pulse, the substrate starts to heat up. After a time, the surface temperature reaches the melting point and a molten layer is formed. Vaporization produces a recoil pressure that acts on the molten layer, removing molten material from the region ahead of the ablation front. The recoil pressure initially overcomes the threshold required for melt ejection sometime shortly after the start of the pulse. At the initiation of melt ejection, the thermal gradients in the material and the vaporization rate at the surface, and hence the recoil pressure, will be at their highest and the molten layer will be at its thinnest. A large number of small droplets are, therefore, ejected at a relatively high velocity. As the pulse progresses, the molten layer thickens, resulting in a larger average droplet size. The recoil pressure decreases, reducing the ejection velocity, but continues to remove material from the ablation front. The molten material moves along the hole walls in a relatively smooth way, breaking up into discrete droplets under the influence of surface tension on exiting the hole. Surface tension effects may also increase the angle of ejection as the molten material follows the curve of the hole entrance on exiting it.

Since the recoil pressure plays an important role in laser drilling, detailed discussion of it and its relationship with the melting front is necessary. Consider a sectioned workpiece under the laser radiation with the laser spot diameter of $2w_0$, as shown in Fig. 4.7, for the material removal stage. Also, for the sake of simplicity, assume a uniform laser intensity distribution at the workpiece surface, i.e.,

$$I_{abs}(r) = I_{abs} . \tag{41}$$

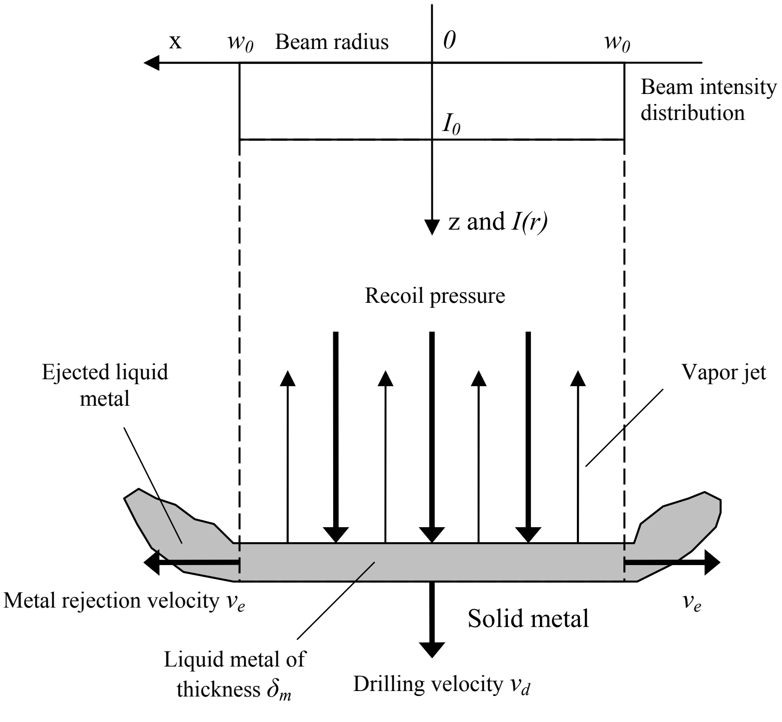

Fig. 4.7. Illustration of melt ejection from the laser-material interaction zone.

The absorption of the laser beam results in heating and melting of the solid metal, increases surface temperature, T_s, of the melt and produces recoil pressure and consequent ejection of the melt from the interaction zone. Melt ejection and evaporation result in a decrease in the melt thickness and melting of a new portion of the solid metal. If the steady-state regime of evaporation and melt ejection is reached then both the melting front and the melt-vapor interface propagate inside the material along the z axis with constant velocity v_d, which is called the "drilling" velocity for the material removal stage. In this case the rate of melting of solid metal equals the sum of the melt ejection and evaporation rates, then

$$\frac{dm_s}{dt} = \frac{dm_e}{dt} + \frac{dm_v}{dt} \quad , \tag{42}$$

where the left-hand side of the equation is the melting rate of the solid, the first term on the right-hand side of the equation denotes the melt-ejection rate and the second term denotes the melt-evaporation rate. Rewriting the mass-conservation Eq. 42 for a unit length along the axis of the laser spot gives

$$2w_0\rho_s v_d = 2\delta_m \rho_m v_e + 2w_0\rho_m v_v \quad , \tag{43}$$

where ρ_s and ρ_m are the densities of the solid and liquid phases, correspondingly, δ_m is the melt-layer thickness at the edge of the laser spot, v_e is the melt-ejection velocity along the x axis at the edge of the spot, and v_v is the velocity of the evaporation front, directed along the z axis similarly to v_d. Using Eq. 43, the "drilling" velocity for material removal stage can be expressed as

$$v_d = \frac{\rho_m}{\rho_s}\frac{\delta_m}{w_0}v_e + \frac{\rho_m}{\rho_s}v_v \quad . \tag{44}$$

The first term on the right-hand side of Eq. 44 is the component of "drilling" velocity due to ejection of melt from the interaction zone, v_{de}, that is,

$$v_{de} = \frac{\rho_m}{\rho_s}\frac{\delta_m}{w_0}v_e \quad , \tag{45}$$

and the second term represents the component of the "drilling" velocity due to evaporation of the melt

$$v_{dv} = \frac{\rho_m}{\rho_s}v_v \quad . \tag{46}$$

If we assumed that, during steady-state front propagation with velocity v_d, the melt thickness is approximately

$$\delta_m \approx \kappa_m / v_d \quad , \tag{47}$$

where κ_m is the thermal diffusivity of the melt metal. Equation 44 can be rewritten as in the following form:

$$v_d{}^2 - \frac{\rho_m}{\rho_s}v_d v_v - \frac{\kappa_m}{w_0}\frac{\rho_m}{\rho_s}v_e = 0 \quad . \tag{48}$$

Solving the quadratic relation given by Eq. 48 and taking only the positive solution gives

$$v_d = \frac{1}{2}\left\{\frac{\rho_m}{\rho_s}v_v + \left[\left(\frac{\rho_m}{\rho_s}v_v\right)^2 + 4\frac{\kappa_m}{w_0}\frac{\rho_m}{\rho_s}v_e\right]^{1/2}\right\} \quad . \tag{49}$$

The value of the evaporation front velocity, v_v, is the same as defined in Eq. 32 for the phase transformation stage, that is

$$v_v = V_0 \exp(-U/T_s) \ , \tag{50}$$

where the energy of evaporation per atom, U, is determined by

$$U = M_a L_v / (N_a k_b) \ , \tag{51}$$

and M_a is the atomic mass, L_v is the latent heat of vaporization, N_a is Avogadro's number, and k_b is Boltzmann's constant.

The evaporation-induced recoil pressure generates melt flow with the dominant direction being that in which the recoil-pressure gradient is the highest. For the case of a rectangular laser spot the melt will flow along the short axis. This means that, in laser welding or drilling, the recoil pressure will provide melt ejection to the sides of the weld pool or cut. Assuming that a steady state has been reached and the distribution of the recoil pressure along the x axis of the spot is close to uniform, then the melt flow is a one-dimensional flow and we can use Bernoulli's equation to relate the melt velocity v_e at the edge of the laser spot to the value of the recoil pressure p_r:

$$p_r = \frac{\rho_m v_e^2}{2} \ . \tag{52}$$

The recoil pressure is proportional to the saturated vapor pressure p_s, which in turn depends on surface temperature, T_s, of the melt as defined in Eq. 37, i.e.

$$p_r = A p_s(T_s) = A B_0 T_s^{-1/2} \exp(-U/T_s) \ , \tag{53}$$

where A is a numerical coefficient, B_0 is a vaporization constant and the parameter, U is the same as that defined in Eq. 51. According to the calculations performed by Anisimov, the coefficient A depends on the ambient pressure and its value varies from 0.55 for evaporation in vacuum to unity for the case of evaporation under a high ambient pressure (Anisimov and Khokhlov, 1995). Calculations also have shown that, for practical values of the ambient pressure, the coefficient A is close to its minimal value of 0.55.

Now let us consider the energy balance in the molten layer exposed to the laser beam when steady-state melt ejection from the interaction zone has been reached. In the coordinate system related to the melting front the solid metal is moving towards the melt front with velocity v_d, melts and then the melt is partially ejected by the recoil pressure towards the sides of the rectangular spot with velocity v_e and partially evaporated from the melt surface.

The input power per unit length of the molten layer is

$$P_{lin} = I_{abs} 2w_0 + \rho_s c_s T_m v_d 2w_0 \quad , \tag{54}$$

where I_{abs} is the absorbed laser beam intensity, ρ_s and c_s are the density and specific heat of the solid metal, respectively, T_m is the melting temperature, and w_0 is the laser beam radius. The first term on the right-hand side of Eq. 54 represents the laser heat input and the second term is the enthalpy flux which is carried into the considered area by the flow of solid metal heated to its melting temperature.

The output power per unit length of the molten layer consists of a conduction term P_{lcond}, convection term P_{lconv}, evaporation term P_{levap}, and a radiation term P_{lrad}. The estimations show that the radiation-related energy transfer from the molten layer is relatively small and can be neglected in our further considerations.

The conduction term can be estimated as the sum of “forwards” and “sideways” components. i.e.,

$$P_{lcond} \approx -k_s \nabla_{forw} T 2w_0 - k_s \nabla_{side} T 2w_0 \quad , \tag{55}$$

where k_s is the thermal conductivity of solid material and the gradients of temperature are taken at the melt front along ("forw") and perpendicularly ("side") to the motion of the solid metal. The "forwards" component can be expressed as

$$-k_s \nabla_{forw} T 2w_0 = k_s \frac{T_m - T_0}{\kappa_s / v_d} 2w_0 = \rho_s c_s (T_m - T_0) v_d 2w_0 \quad , \tag{56}$$

where κ_s is the thermal diffusivity of the solid metal. The estimation of the "sideways" component gives

$$-k_s \nabla_{side} T 2w_0 \approx k_s \frac{T_m - T_0}{\left[\frac{\kappa_s}{v_d}\left(w_0 + \frac{\kappa_m}{v_d}\right)\right]^{1/2}} 2w_0 \approx \frac{\rho_s c_s (T_m - T_0) v_d}{\left(\frac{\kappa_m}{\kappa_s} + \frac{v_d}{\kappa_s} w_0\right)^{1/2}} 2w_0 \quad , \tag{57}$$

where the melt thickness is determined by Eq. 47.

The convection term P_{lconv} is as follows:

$$P_{lconv} = 2\rho_m \left(c_m T^* + L_m\right) v_e \delta_m \approx 2\rho_m \left(c_m T^* + L_m\right) v_e \kappa_m / v_d \quad , \tag{58}$$

where T^* is the average temperature in the melt layer, defined as

$$T^* = T_m + \alpha \left(T_s - T_m\right) \quad , \tag{59}$$

where T_m is the melting temperature, T_s is the surface temperature of the melt, and α is a constant smaller than unity.

The power per unit length spent for the evaporation is

$$P_{levp} = \rho_m v_v L_v 2w_0 \quad , \tag{60}$$

where the velocity of the evaporation front, v_v, is determined by Eq. 50 and L_v is the latent heat of evaporation.

Combining Eqs 54 to 60 dividing both sides of the resulting equation by $2w_0$ and leaving the absorbed laser intensity I_{abs} on the left-hand side of the equation gives

$$I_{abs} = \left[\rho_m \left(c_m T^* + L_m \right) \frac{v_e \kappa_m}{v_d w_0} - \rho_s c_s T_0 v_d \right] + \frac{\rho_s c_s \left(T_m - T_0 \right) v_d}{\left(\frac{\kappa_m}{\kappa_s} + \frac{v_d}{\kappa_s} w_0 \right)^{1/2}} + \rho_m v_d L_v \quad , \tag{61}$$

where the "drilling" velocity v_d and the melt ejection velocity v_e can be expressed through the surface temperature T_s of the melt using Eqs 50 to 53 and the average temperature in the melt layer T_m is related to the surface temperature, T_s, of the melt according to Eq. 59. Is it easy to see that the first two terms within the first parenthesis on the right-hand side of Eq. 61 represent the part of the absorbed laser intensity that is expended for melting and heating the solid which crossed the melting front. Simultaneously this term represents an energy flux from the interaction zone due to melt flow (the convection term in the heat-transfer equation). The third term on the right-hand side of Eq. 61 is the energy loss from the interaction zone due to heat conduction and the last term is the evaporation-related loss.

Equation 61 gives an implicit dependence of the melting front velocity and its component, absorbed intensity, and the thermophysical parameters of the workpiece as the function of the melting surface temperature. Therefore, by selecting a proper range of the melting surface temperature, the range of the recoil pressure and the melting front can be calculated.

The mechanisms involved in melt ejection are rather complex and are at present poorly understood, and it was found that material removal is somewhat irregular and can lead to asymmetric, irregular hole shapes. The extent to which melt ejection occurs depends both on material properties and on laser conditions. A threshold beam intensity must be reached before melt ejection occurs. The proportion of material removed by melt ejection was observed to increase with further increase of intensity. It was noted that increasing the pulse intensity increases the pressure generated, hence increasing the flow velocity of molten material. Low intensity pulses tend to generate relatively thick molten layers, whereas high intensity pulses eject melt more efficiently. The control of melt ejection and pulse intensity can be achieved by temporally shaping the beam pulses or pulse trains.

Two types of melt ejection – an initial burst of slow particles (attributed to radial pressure gradients expelling material), followed about 0.1 ms after the start of the pulse, by finer, faster-moving particles, and then by larger, slower-moving ones. The second type of melt ejection is that nucleate boiling is occurring in the molten layer. This is predicted to occur about 120 μs after the start of the pulse. After an initial burst of melt ejection, there is an approximately exponential decay in drilling velocity from about 12 m/s as the molten layer reforms and thickens until an equilibrium is reached between the absorbed intensity and energy loss via material expulsion, resulting in a steady start drilling velocity of 1.0 to 1.5 m/s after 100 to 125 μs. The initial drilling velocity would, therefore, be significantly higher than that predicted by steady state models.

Liquid expulsion rate goes through a maximum as the power density increases. Low intensities produce a low liquid ejection rate, due to a lower rate of vaporization and hence recoil pressure, whereas the high thermal gradients generated by higher intensities lead to a thin molten layer, again reducing the rate of liquid expulsion. An initial burst of melt ejection was modeled as the flow of molten material, once pressure gradients in the drilled hole are great enough to overcome surface tension forces. This is followed by flow, driven by radial pressure gradients resulting from radial intensity gradients in the incident beam. However, no experimental evidence was presented for the dependence of the second type of melt ejection on a radially-varying intensity distribution.

Generally, MEF (melt ejection fraction) values of the order of 50% were obtained, and a high metal density (such as for tungsten) inhibits melt ejection. The MEF will increase when an increased pulse intensity increases the pressure gradients inside the hole, resulting in more complete expulsion of melt. Any increase in the thickness of the molten layer due to the higher energy input will also contribute to this effect. Conversely, an increased pulse intensity could increase temperature gradients at the ablation surface, so that the vaporization rate at the surface of the molten layer is increased so much that the thickness of the molten layer is reduced. This lowers the MEF, because there is simply less molten material available to eject.

The average particle size decreases with increasing pulse intensity. Examination of sectioned holes reveals a close correlation between the average droplet size and the observed resolidified layer thicknesses. The molten layer moves along the cavity walls smoothly, breaking up into droplets under the influence of surface tension forces on exiting the hole. The difference in ejected particle sizes of the two pulses with the same overall intensity in attributed to the greater total energy input during the longer pulse. This forms a thicker molten layer and results in the ejection of correspondingly larger droplets. The higher intensity pulse ejects the smaller droplets. This is due to the thinner molten layer generated by the higher thermal gradients and surface temperatures, as well as the increased vaporization rate.

Melt ejection aids the drilling process by removing molten material from the region directly ahead of the ablation front. Possible mechanisms of material removal are the recoil-driven flow of molten material along the walls of the hole, followed by a break-up into discrete droplets due to surface tension effects on leaving the hole. An alternative mechanism is that explosions due to nucleate boiling fling the material from the ablation front in the form of droplets. This second mechanism would produce an angular distribution limited by the geometry of the hole, with ejection mainly confined to a narrow solid angle centered on the hole axis. Some material would be expected to be ejected at greater angles, due to the shallower, lower aspect ratio, geometry of the hole during the early stages of drilling. The angular distribution results indicate that it is certainly not solely this second mechanism of melt removal that is active during melt ejection the cases studies. If the melt is considered to flow along the walls of the hole, and then break up under the influence of surface tension on exiting the hole, surface tension effects at the hole entrance could tend to deviate the molten material, curving its trajectory to follow the shape of the entrance hole, and thereby increasing the angle of ejection.

4.3. Laser welding

Laser welding represents a delicate balance between heating and cooling within a spatially localized volume overlapping two or more solids such that a liquid pool is formed and remains stable until solidification. The objective of laser welding is to produce the liquid melt pool by absorption of incident radiation, allow it to grow to the desired size, and then to propagate this melt pool through the solid interface eliminating the original seam between the components to be joined. Unsuccessful results are obtained if the melt pool is too large or too small or if significant vaporization occurs while it is present. The quality of the resulting weld may also be compromised by vaporization of alloy components, excessive thermal gradients that lead to cracking on solidification, and instabilities in the volume and geometry of the weld pool that can result in porosity and void formation.

Maintenance of the balance between heat input and heat output depends on constant absorption of laser radiation and uniform dissipation of heat inside the workpiece. The path taken by laser radiation toward the workpiece is often interrupted due to the evolution of hot gas from the laser focus. Under certain conditions this hot gas may turn into a plasma that can severely attenuate the laser beam due to absorption and scattering. Constant heat dissipation within the workpiece in the presence of a weld pool requires a stable geometry between the fusion front and the surrounding metal. The liquid-solid interface is rarely undisturbed, particularly when welding is performed on moving objects or with a moving laser beam. This introduces additional geometry-dependent terms into the cooling rate of the weld pool.

Despite the constraint that excitation and cooling be balanced in laser welding, a variety of thermal and mechanical time constants act to moderate this requirement, smoothing out fluctuations to a certain extent and allowing the establishment of stable welding conditions. A primary goal of research into laser welding has been to identify those parameters that influence the stability and reproducibility of laser welding and to develop ways to control these parameters. This begins with the laser source itself because of fluctuations in the weld pool and can lead to instabilities. The highly nonlinear nature of laser material interaction processes means that certain fluctuations may grow rapidly in amplitude. This also offers the possibility of control over the laser welding process through selective modulation of the laser output.

There are two fundamental modes of laser welding: (1) conduction welding, and (2) keyhole or penetration welding. The basic difference between these two modes is that the surface of the weld pool remains unbroken during conduction welding and opens up to allow the laser beam to enter the melt pool in keyhole welding.

Conduction welding offers less perturbation to the system because laser radiation does not penetrate into the material being welded. As a result, conduction welds are less susceptible to gas entrapment during welding. With keyhole welding, intermittent closure of the keyhole can result in porosity.

Conduction and penetration modes also are possible in spot welding. The transition from the conduction mode to that in which a keyhole is formed depends on the peak laser intensity and duration of the laser pulse applied to the workpiece. Tailoring of the time dependence of the laser pulse intensity can produce a change from one type of welding mode to the other. The weld can be initiated in the conduction mode and then converted to keyhole welding later in the interaction. It is also possible to tailor this interaction such that the keyhole, once created, can be withdrawn at the termination of the pulse in such a way that gas entrapment is minimized. The intensity temporal profile also can be adjusted to minimize the thermal gradients in the weld pool that lead to solidification cracking.

4.3.1. Thresholds of laser welding

The coupling of laser radiation into a metal to produce the localized heating required for spot or seam welding involved a delicate balance among many parameters. Some of these parameters, such as laser intensity, pulse shape, and beam polarization, are under the control of the operator, whereas others, such as metal reflectivity, thermal conductivity, and heat capacity, are not. Optimization of laser welding involves defining a set of experimental conditions that lead to stable and reproducible welding conditions and monitoring these conditions for quality assurance and possible real-time adaptive control.

4.3.1.1. Conduction welding

Under conduction limited conditions, the onset of surface melting can be estimated from the simple model. The temperature at the center of the beam focus (r=0) is

$$T(0,t)-T_0=\frac{AI(0)w}{k(2\pi)^{1/2}}\tan^{-1}\left(\frac{8\kappa t}{w^2}\right)^{1/2} \quad , \tag{62}$$

where k is the thermal conductivity, κ is thermal diffusivity, w is the Gaussian beam radius, T_0 is the ambient temperature, and t is time. If $T(0,t)=T_m$, the melting temperature, then the laser beam intensity, $I_m(0)$, required to produce melting in time t can be obtained with Eq. 62. $I_m(0)$ is found to be essentially independent of time when $t >> w^2/8\kappa$ or when the thermal diffusion length $l \sim (kt)^{1/2} >> w$. Because $AI_m(0)$ is obtained as a solution, it is apparent that with t specified, $I_m(0)$ can be reduced through an increase in the absorptivity A. The radius of the beam focus on the surface, w, will have a profound effect on $I_m(0)$ when t is long but essentially has no effect at short pulse lengths. These solutions do not take into account the latent heat of fusion and thus must be taken to be approximate.

An estimate of the depth of penetration, z_m, of the weld pool under spot welding conditions in which melting is included can be obtained, when consider t_m as the time at which $T(z=0)=T_m$, as (Duley, 1999)

$$z_m(t)\sim\frac{0.16AI}{\rho L_m}(t-t_m) \quad , \tag{63}$$

where ρ is the density of the melt and L_m is the latent heat of fusion. Equation 63 will be strictly valid only when $t_m < 8\kappa/w^2$.

4.3.1.2. Keyhole welding

The formation of a keyhole is of fundamental importance for penetration welding. The way in which this occurs is poorly understood, but begins with vaporization at the surface of a weld pool. For a planar surface and an incident beam with a Gaussian intensity profile, the solution is given by Eq. 57 with $T(0,t)=T_v$ as the vaporization temperature. Then

$$T_v - T_0 = \frac{A_v I(0) w}{k_v (2\pi)^{1/2}} \tan^{-1}\left(\frac{8\kappa_v t}{w^2}\right)^{1/2} , \tag{64}$$

where the subscripts refer to values at or near the vaporization temperature. In many cases, this information is not available, so approximate values must be used.

As for melting, the threshold for vaporization is found to depend on focal radius and pulse duration but becomes independent of time for long pulse lengths (Trappe et al., 1994). This again assumes that the surface absorptivity is independent of time. The disruption of the surface when vaporization begins will, in general, lead to enhanced coupling and the possibility of a "thermal runaway" effect at the laser focus.

In the initial stage of vaporization, the metal surface will be unperturbed and normal to the direction of incident laser radiation. Under these conditions, a simple one-dimensional vaporization model may be used. The mass evaporation rate, β, is related to vapor pressure $p(T)$ as follows:

$$\beta(T) = p(T)\left(\frac{\overline{m}}{2\pi k_b T}\right)^{1/2} , \tag{65}$$

where $\overline{m}$ is the average mass of an evaporation, k_b is Boltzmann's constant, and $T(K)$ is surface temperature. The vapor pressure is given by the Clausius-Clapeyron equation

$$p(T) = p(T_B)\exp\left[\frac{\overline{m}L_v}{\rho k_b}\left(\frac{1}{T_B} - \frac{1}{T}\right)\right] \quad , \tag{66}$$

where $T_B(K)$ is the boiling temperature and L_v is the latent heat of vaporization (J/m^3).

The linear vaporization rate is

$$v = \frac{\beta(T)}{\rho} \quad , \tag{67}$$

where ρ is the metal density.

For optimal vaporization, the kinetic vaporization rate, v, must be equal to that limited by conservation of energy. Then

$$\frac{\beta(\overline{T})}{\rho} = \frac{AI}{L_m + L_v + c(\overline{T} - T_0)} \quad , \tag{68}$$

where c is the heat capacity, T_0 is ambient temperature, L_m and L_v are the latent heats of melting and vaporization, respectively. The equality given by Eq. 68 defines a temperature $\overline{T}$ that need not be the normal boiling temperature, T_B. At high laser intensity, the linear speed of vaporization, v, approaches the speed of sound in the metal. At the typical laser intensities used in laser welding of metals, $v \sim 1 - 10^2 cm/\sec$, and the establishment of the keyhole can occur very rapidly., particularly when geometrical effects lead to enhanced coupling of incident laser radiation once vaporization begins.

The threshold for the formation of a keyhole also can be affected by surface tension and convective flow in the laser weld pool near the vaporization temperature.

Both processes can cause an upwelling of liquid at the periphery of the weld pool, which will facilitate self-focusing of incident laser radiation at the center of the weld pool. The enhancement in intensity at this point can be substantial and can assist in the initiation of a keyhole. Experimental evidence for the development of a concave liquid surface at the threshold for formation of a keyhole was reported (Duley, 1999).

An intrinsic instability in laser-irradiated surfaces also may be responsible for enhanced coupling at high laser intensity. The effect involves the production of a grating-like structure with periodicities comparable to the laser wavelength. This is accompanied by enhanced absorption of laser radiation, with coupling efficiencies approaching unity. It has been suggested that this increased coupling is responsible for the large drop in metal reflectivity seen hear the intensity threshold for laser welding.

4.3.2. Laser welding mechanism

Laser welding is a fusion process, where materials are joined by melting the interface between them and allowing it to solidify. Such processes produce three distinct regions: the base metal, which is material that has not been altered by the welding process, the fusion zone, composed of material that was melted during welding, and the heat affected zone (HAZ) composed of base metal that has been changed in some measureable way by heat associated with welding (Wojcicki and Pryputniewicz, 1997).

In welding, one is often concerned about performing the process with the minimum possible amount of heat. From this standpoint, the most efficient method of welding is called deep penetration or keyhole welding. To perform keyhole welding with a laser, a lens is used to focus the beam onto the surface of a metal workpiece. Although most metals are good reflectors of infrared light, the high irradiance of the focused beam heats the metal beyond its melting point. The liquid is usually a better absorber than the solid, and so heats up even further until some of it vaporizes. The vaporized metal opens a cylinder (called a keyhole) down through the workpiece, holding back the surrounding liquid with vapor pressure. This vapor ionizes and absorbs the incoming radiation, becoming incandescent and radiating energy to the molten metal along the side of the keyhole. The material at the edge of the hole also absorbs energy from the laser beam. Since energy is transferred to the workpiece along the entire depth of the keyhole, deep penetration can be achieved. Relative motion of the welding head and workpiece produces a seam weld by moving the keyhole through the material. As the keyhole moves, liquid metal flows from its forward surface to the back, where it solidifies. This flow is driven by temperature-induced variations in the surface tension of the molten metal. Keyhole welding is efficient because the vapor channel traps the laser beam, reducing loss of energy by reflection, and because the keyhole acts as a cylindrical heat source extending below the surface of the workpiece, reducing loss of energy by thermal conduction out of the fusion zone.

In laser welding, a weld pool is generated and the effect of weld pool fluid flow on the geometry of the resultant weld is necessity for understanding laser welding mechanism. The major driving forces for fluid flow in the weld pool generally include the buoyancy force, the shear stress induced by the surface tension gradient at the weld pool surface, and the shear stress acting on the pool surface by the plasma. For the buoyancy force, consider that the density of the liquid metal decreases with increasing temperature. Because the laser source is located above the center of the pool surface, the liquid metal is warmer at the center of the pool and cooler at the edge of the pool. Therefore, gravity causes the heavier liquid metal at the boundary of the pool to sink. Consequently, the liquid metal falls along the pool boundary and rises along the pool axis, as shown in Fig. 4.8a. The convection caused by buoyancy force produces the maximum velocity along the pool axis, and the pool surface is slightly above the workpiece surface because of the expansion of the metal upon heating and melting.

For the shear stress induced by surface tension gradient, for the case in the absence of a surface-active agent, the surface tension, γ, of the liquid metal decreases with increasing temperature, namely, $\partial\gamma/\partial T < 0$. As shown in Fig. 4.8b, the warmer liquid metal with a lower surface tension at the center of the pool surface is pulled outward by the cooler liquid metal with a higher surface tension at the boundary of the pool surface. In other words, an outward shear stress is induced at the pool surface by the surface tension gradient along the pool surface. This causes the liquid metal to flow from the center of the pool surface to the edge and return below the pool surface, as shown in Fig. 4.8b. Surface-tension-driven convection is also called the thermocapillary convection of Marangoni convection. Heiple et al, proposed another model that, when a surface-active agent is present in the liquid metal in a small but significant amount,

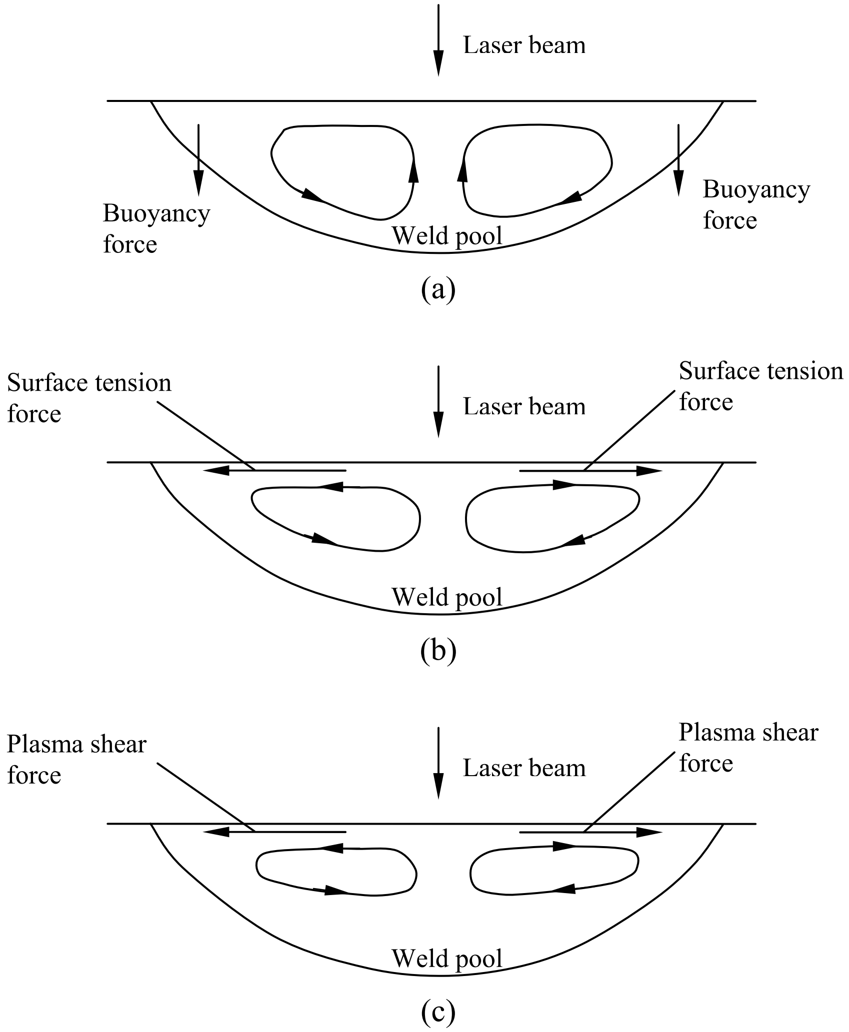

Fig. 4.8. Driving forces for weld pool convection: (a) buoyancy force, (b) shear stress caused by surface tension gradient, (c) shear stress caused by plasma.

$\partial \gamma / \partial T$ can be changed from negative to positive, thus reversing Marangoni convection occurs and making the weld pool much deeper (Kou, 2002). Examples of surface-active agents in steel and stainless steel are S, O, Se, and Te. In the reversing Marangoni convection, the cooler liquid metal of lower surface tension at the edge of the pool surface is pulled inward by the warmer liquid metal of higher surface tension near the center of the pool surface, and this model favors convective heat transfer from the heat source to the pool bottom (Zacharia et al., 1989).

For the shear stress induced by plasma, the plasma moves outward at high speed along a pool surface can exert an outward shear stress at the pool surface, as shown in Fig. 4.8c. This shear stress caused the liquid metal to flow from the center of the pool surface to the pool edge and return below the pool surface, as shown in Fig. 4.8c.

The effect of turbulence was also considered in some works for the fluid dynamics of the weld pool (Choo and Szekely, 1994). Assumption of laminar flow showed an over-prediction the pool depth, and turbulence was proved to be a more reasonable assumption, which included the increase of effective viscosity and the resultant slow down of convection.

4.3.3. Metallurgical aspects of laser welding

Laser welding is a process where the workpiece material experience heating, melting, and solidification and forms the fusion zone with modified grain structure. Solidification is a very complex procedure, as it depends on the material compositions, solidification modes (planer, cellular, or dendritic), cooling rate, etc. It is the grain structure developed in the fusion zone that has the most influence to the quality and performance of the laser welded parts, and usually the formation of fine equiaxed grains in the fusion zone are favorable since the fine grains can help reduce the susceptibility of the weld metal to solidification cracking during welding, and also fine grains can improve the mechanical properties of the weld, such as the ductility and fracture toughness. Therefore, much effort has been made to try to refine grain of the weld fusion zone.

Solidification cracking, which is observed frequently in casting and ingots, can also occur in fusion welding. Usually the cracking is intergranular, that is, along the grain boundaries of the weld metal. It occurs during the terminal stage of solidification, when the tensile stresses developed across the adjacent grains exceed the strength of the almost completely solidified weld metal. The solidifying weld metal tends to contract because of both solidification shrinkage and thermal contraction. The surrounding base metal also tends to contract, but not as much, because it is neither melted nor heated as much on the average. Therefore, the contraction of the solidifying metal can be hindered by the base metal, especially if the workpiece is constrained and cannot contract freely. Consequently, tensile stresses develop in the solidifying weld metal. The severity of such tensile stresses increases with both the degree of constraint and the thickness of the workpiece.

Metallurgical factors that have been known to affect the solidification cracking susceptibility of weld metals include the solidification temperature range, the amount and distribution of liquid at the terminal stage of solidification, the primary solidification phase, the surface tension of the grain boundary liquid, and the grain structure. All these factors are directly or indirectly affected by the weld metal composition. Beside the metallurgical factors, the presence of mechanical factors is necessary for the formation of solidification cracking, since there should be enough stresses acting on adjacent grains during solidification in order to let cracking occur. The stresses can be due to thermal contraction or solidification shrinkage or both. In addition, the degree of restraint of the workpiece is another mechanical factor of solidification cracking. For the same joint design and material, the greater the restraint of the workpiece, the more likely solidification cracking will occur.

Almost all laser welding is performed on metal, and all the rules of metallurgy continue to apply on laser welding. The metallurgical differences between laser beam welding and conventional processes are related to the small size and high intensity of the focused laser beam as a heat source. The fusion zone is small, and the part is heated (and cool down) rapidly. This is generally an advantage, as problems such as grain growth in high strength low alloy steels or the sensitization of austenitic stainless steels do not have time to appear. In addition, the relatively small volume of the fusion zone in comparison to conventional welding reduces the stresses associated with solidification shrinkage. Rapid solidification rates, however, can produce atypical microstructures and constituents in many common alloys.

4.3.3.1. Laser welding on stainless steel

Stainless steels are a class of Fe-base alloys that noted for their high corrosion and oxidation resistance. They usually contain from 12 to 27% Cr and 1 to 2% Mn by weight, with the addition of Ni in some grades. Stainless steels are classified into three major categories based on the structure: ferritic, martensitic, and austenitic. In this

Dissertation, stainless steel 304 was used, which belongs to the austenitic stainless steel class. The addition of Ni (fcc) into Fe-Cr alloys tends to widen the range over which austenite (fcc) exists and increase its stability at low temperatures. Generally speaking, austenitic stainless steel contain at least 15% Cr and enough Ni to maintain a stable austenitic structure over the temperature range from 1100^{o}C to room temperature without the formation of martensite.

Austenitic stainless steels weld easily. They are single phase, ductile materials with no volatile alloying elements. For identical weld parameters, the low thermal conductivity of stainless steel results in narrower and deeper welds than carbon steel. Because of the oxidation resistance of stainless steel, shield gas is not required in some cases.

The rapid heating and cooling characteristic of laser welding alters the behavior of stainless steel as compared to its reaction to welding processes with higher heat inputs. A common problem with conventionally welded stainless is sensitization: at temperatures ranging from 650 to 870^{o}C, residual carbon combines with chromium, reducing corrosion resistance of the alloy. Sensitization is rarely seen in laser welding because the metal is heated and cooled through the problem range so rapidly that significant chromium depletion cannot occur. This allows the use of less expensive grades of stainless without suffering a performance penalty.

A negative effect of rapid cooling on stainless steel is that it can cause cracking. When a molten metal alloy solidifies, certain constituents appear, producing characteristic structures. Austenitic stainless steels are so named because the predominant constituent of their normal microstructures is a phase called austenite. If the material is 100% austenite, however, it lacks strength in the temperature range from its solidification point down to about $1000^{o}C$. Stresses arising from thermal contraction can therefore cause microscopic cracks in the metal.

4.3.3.2. Laser welding on copper

While copper does not present metallurgical problems for laser welding, it reflects infrared light very well, so it is hard to get power from Nd:YAG laser into it. Its high thermal diffusivity also results in a lot of the absorbed energy being transferred away from the fusion zone and wasted. Alloys of copper such as brass and bronze, which generally have much lower thermal conductivity and reflectivity than the pure copper, do not present particular problems for laser welding.

4.3.4. Thermal stress problem for laser welding

In order to account for the thermomechanical effect during the heating process, the energy transport equation for a deformable solid body can be written for the specific enthalpy as

$$h \equiv h(T, e) \ , \tag{69}$$

where e is the strain. Equation 69 can be written as

$$\rho dh = \rho\left(\frac{\partial h}{\partial T}\right)_e dT + \rho\left(\frac{\partial h}{\partial e}\right)_T de \quad . \tag{70}$$

It can be shown that

$$\rho\left(\frac{\partial h}{\partial e}\right)_T \cong \left(\frac{\partial C_V}{\partial T}\right)_{T_0} T_0 \quad , \tag{71}$$

where C_V is the volumetric specific heat and T_0 is the reference temperature. However,

$$-\nabla \cdot q = \rho dh \ , \tag{72}$$

or

$$-\nabla \cdot q = C_p \frac{\partial T}{\partial t} + \alpha_\sigma T_0\left(\frac{\partial e}{\partial t}\right) \quad , \tag{73}$$

where α_σ is related to the coefficient of thermal expansion and it is

$$\alpha_\sigma \equiv \left(\frac{\partial C_V}{\partial T}\right) \quad . \tag{74}$$

Rearrangement of Eq. 73 yields

$$-\nabla \cdot q = C_p \frac{\partial T}{\partial t}\left[1 + \frac{\alpha_\sigma T_0(\partial e / \partial t)}{C_p dT}\right] \quad , \tag{75}$$

or

$$-\nabla \cdot q = C_p \frac{\partial T}{\partial t}\left[1 + \eta\left(\frac{\partial e / \partial t}{\alpha_e dT}\right)\right] \quad , \tag{76}$$

where

$$\eta = 3G\alpha_e^{\ 2} T_0 / C_p \quad , \tag{77}$$

$$\alpha_e = \alpha_\sigma / 3G \quad , \tag{78}$$

$$G = \frac{E}{3(1-2\nu)} \quad , \tag{79}$$

and η is called the thermomechanical coupling factor, which is shown to be small for most metals at room temperature.

The stress component can be written as (Hetnarski, 1986)

$$\sigma_x = Ee_x - E\alpha_e T \quad , \tag{80}$$

$$\sigma_y = Ee_y - E\alpha_e T \quad , \tag{81}$$

$$\sigma_z = Ee_z - E\alpha_e T \quad , \tag{82}$$

with

$$e_x = \frac{\partial U}{\partial x} \quad , \tag{83}$$

$$e_y = \frac{\partial U}{\partial y} \quad , \tag{84}$$

$$e_z = \frac{\partial U}{\partial z} \quad , \tag{85}$$

where U is the thermal displacement. In the stress field the equilibrium condition yields

$$\nabla \cdot \sigma = \rho \frac{\partial^2 U}{\partial t^2} \quad . \tag{86}$$

Therefore,

$$\nabla^2 U - \alpha_e (\nabla \cdot T) = \frac{\rho}{E} \frac{\partial^2 U}{\partial t^2} \quad . \tag{87}$$

Using Eqs 74 to 76, and combining Eqs 73 and 77, we obtain

$$-\nabla \cdot q = C_p \frac{\partial T}{\partial t} + \left(\frac{C_p \eta}{\alpha_e} \right) \frac{\partial}{\partial t} (\nabla \cdot U) \quad . \tag{88}$$

The equation describing the energy transport due to electro-phonon interaction can be written as

$$-\nabla \cdot q = k\left(\nabla^2 \cdot T\right) + \frac{C_p \lambda^2}{f}\frac{\partial}{\partial t}\left(\nabla^2 \cdot T\right) + I_{surf}\,\delta \exp\left(-\delta|x|\right) \ . \tag{89}$$

Combination of Eqs 88 and 89 yields

$$\frac{\partial T}{\partial t} = \alpha\left(\nabla^2 \cdot T\right) + \frac{\lambda^2}{f}\frac{\partial}{\partial t}\left(\nabla^2 \cdot T\right) - \left(\frac{\eta}{\alpha_e}\right)\frac{\partial}{\partial t}\left(\nabla \cdot U\right) + I_{surf}\frac{\delta}{C_p}\exp\left(-\delta|x|\right) \ . \tag{90}$$

Equation 90 is the general energy transport equation, which includes the thermomechanical effect. Note that the initial condition is: at *t=0*, *T=0* and *U=0*. The boundary conditions are: since the laser pulse length and heating duration are short, there is no convective or radiation losses are considered from the surface, therefore

at $t > 0$ and at the surface, $\frac{\partial T}{\partial x}\Big|_{surface} = 0$,

at t>0 and $x = y = z = \infty$, $T = 0$ and $U = 0$.

During laser materials processing, the heating is localized and, therefore, a very large temperature variation occurs over a small region. Owing to this temperature gradient, large thermal stresses are generated in the substrate, which can lead to the defects in the material such as the formation of cracks and fractures in the material. The stress is related to strains by

$$\{\sigma\} = [D]\{\varepsilon^e\} \ , \tag{91}$$

where $\{\sigma\}$ is the stress vector, and $[D]$ is the elasticity matrix.

$$\{\varepsilon^e\} = \{\varepsilon\} - \{\varepsilon^{th}\} \ , \tag{92}$$

where $\{\varepsilon\}$ is the total strain vector and $\{\varepsilon^{th}\}$ is the thermal strain vector.

Equation 92 may also be written as

$$\{\varepsilon\} = [D]^{-1}\{\sigma\} + \{\varepsilon^{th}\} \quad . \tag{93}$$

Since the present case is axially symmetric, and the material is assumed to be isotropic, Eqs 91 to 93 can be written as in Cartesian coordinates as

$$\varepsilon_{xx} = \frac{1}{E}\left[\sigma_{xx} - \nu\left(\sigma_{yy} + \sigma_{zz}\right)\right] + \alpha_e \Delta T \quad , \tag{94}$$

$$\varepsilon_{yy} = \frac{1}{E}\left[\sigma_{yy} - \nu\left(\sigma_{xx} + \sigma_{zz}\right)\right] + \alpha_e \Delta T \quad , \tag{95}$$

$$\varepsilon_{zz} = \frac{1}{E}\left[\sigma_{zz} - \nu\left(\sigma_{yy} + \sigma_{xx}\right)\right] + \alpha_e \Delta T \quad , \tag{96}$$

$$\varepsilon_{yx} = \frac{1+\nu}{E}\sigma_{xy} \quad , \tag{97}$$

$$\varepsilon_{xz} = \frac{1+\nu}{E}\sigma_{xz} \quad , \tag{98}$$

$$\varepsilon_{yz} = \frac{1+\nu}{E}\sigma_{yz} \quad , \tag{99}$$

where *E*, ν, and α_e are the modulus of elasticity, Poisson's ratio, and coefficient of thermal expansion, respectively. ΔT represents the temperature rise at a point (*x,y,z*) at time = *t* with respect to that at *t* = 0 corresponding to a stress free condition. A typical component of thermal strain from Eqs 94 to 99 is

$$\varepsilon^{th} = \alpha_e \Delta T = \alpha_e\left(T - T_{ref}\right) \quad , \tag{100}$$

where T_{ref} is the reference temperature at *t* = 0.

When α_e is a function of temperature, Eq. 100 becomes

$$\varepsilon^{th} = \int_{T_{ref}}^{T} \alpha_e(T)dT \quad . \tag{101}$$

The present study uses a mean, or weighted-average, value of α_e such that (Yilbas et al., 2000)

$$\varepsilon^{th} = \overline{\alpha_e}(T)(T - T_{ref}) \quad , \tag{102}$$

where $\overline{\alpha_e}(T)$ is the mean value of coefficient of thermal expansion and is given by

$$\overline{\alpha_e}(T) = \frac{\int_{T_{ref}}^{T} \alpha_e(T)dT}{T - T_{ref}} \quad . \tag{103}$$

The principle stresses $(\sigma_1, \sigma_2, \sigma_3)$ are calculated from the stress components by the cubic equation

$$\begin{vmatrix} \sigma_{xx} - \sigma_p & \sigma_{xy} & \sigma_{xz} \\ \sigma_{xy} & \sigma_{yy} - \sigma_p & \sigma_{yz} \\ \sigma_{xz} & \sigma_{yz} & \sigma_{zz} - \sigma_p \end{vmatrix} = 0 \tag{104}$$

where σ_p is the principle stress.

The von Mises or equivalent stress, σ', is computed as

$$\sigma' = \sqrt{\frac{1}{2}\left[(\sigma_1 - \sigma_2)^2 + (\sigma_2 - \sigma_3)^2 + (\sigma_3 - \sigma_1)^2\right]} \quad . \tag{105}$$

The equivalent stress is related to the equivalent strain through

$$\sigma' = E\varepsilon' \quad , \tag{106}$$

where ε' is the equivalent strain.

The boundary conditions for stresses are: since there is no surface tractions are involved in the problem under consideration the corresponding boundary and initial conditions are introduced:

at t=0, $\sigma = 0$,

at t>0 and at the surface, $\sigma_{surface} = 0$,

at t>0 and $x = y = z = \infty$, $\sigma = 0$.

4.4. Theoretical considerations

Laser materials processing is a very complex procedure including various physical phenomena such as fluid flow, thermalmechanical, and electro-magnetic effect due to the existence of plasma plume. In this section, some aspects for the physical phenomena during laser materials processing are discussed in details, as they all have pronounced influence on the results of laser materials processing.

4.4.1. Consideration of laser beam properties

A focused laser beam is one of the highest power density sources available to industry. Properties of the laser beam itself are complicated, since they involve the distribution of the laser power in both spatial and temporal domains. Depending on the laser beam power distribution that is used in the computational model, different temperature and stress/strain distributions can be obtained and will affect overall configuration and quality of laser micromachined workpieces. Usually power is assumed to be uniform in analytical and computational studies for simplicity, however for the Nd:YAG laser, a single-mode TEM_{00} beam close to a Gaussian profile occur for most of the industrial applications.

The Gaussian is a radially symmetric distribution whose electric field variation is given by

$$E_S = E_0 \exp\left(-\frac{r^2}{{w_0}^2}\right) \quad . \tag{107}$$

The Gaussian source distribution remains Gaussian at every point along its path of propagation through the optical system. This makes it particularly easy to visualize the distribution of the fields at any point in the optical system. The intensity is also Gaussian:

$$I_S = \eta E_S {E_S}^* = \eta E_0 {E_0}^* \exp\left(-\frac{2r^2}{{w_0}^2}\right) \quad . \tag{108}$$

The Gaussian has no obvious boundaries to give it a characteristic dimension like the diameter of the circular aperture, so the diameter of the size of a Gaussian is somewhat arbitrary. The Gaussian intensity distribution for a typical laser can be expressed as

$$I(r) = I_0 \exp\left(-\frac{2r^2}{{w_0}^2}\right) \quad . \tag{109}$$

The parameter w_0, usually called the Gaussian beam radius, is the radius at which the intensity has decreased to $1/e^2$ or 0.135 of its value on the axis. Another point to note is the radius of half maximum, or 50% intensity, which is 0.59 w_0. At 2 w_0, or twice the Gaussian radius, the intensity is 0.0003 of its value on axis, usually completely negligible.

The power contained within a radius *r*, *P(r)*, is easily obtained by integrating the intensity distribution from 0 to *r*:

$$P(r) = P_\infty\left[1 - \exp\left(-\frac{2r^2}{w_0^{\,2}}\right)\right] \quad . \tag{110}$$

When normalized to the total power of the beam, $P(\infty)$ in Watts, the curve is the same as that for intensity, but with the ordinate inverted. Nearly 100% of the power is contained in a radius $r = 2w_0$. One-half the power is contained within 0.59 w_0, and only about 10% of the power is contained with 0.23 w_0, the radius at which the intensity has decreased by 10%. The total power, $P(\infty)$ in Watts, is related to the on-axis intensity, *I(0)* (Watts/m^2), by

$$P_\infty = \left(\frac{\pi w_0^{\,2}}{2}\right) I(0) \quad , \tag{111}$$

$$I(0) = P_\infty\left(\frac{2}{\pi w_0^{\,2}}\right) . \tag{112}$$

The transverse distribution intensity remains Gaussian at every point in the system; only the radius of the Gaussian and the radius of curvature of the wavefront change. Imagine that we create a coherent light beam with a Gaussian distribution and a plane wavefront at a position *x=0*. The beam size and wavefront curvature will then vary along axis *x*, as shown in Fig. 4.9.

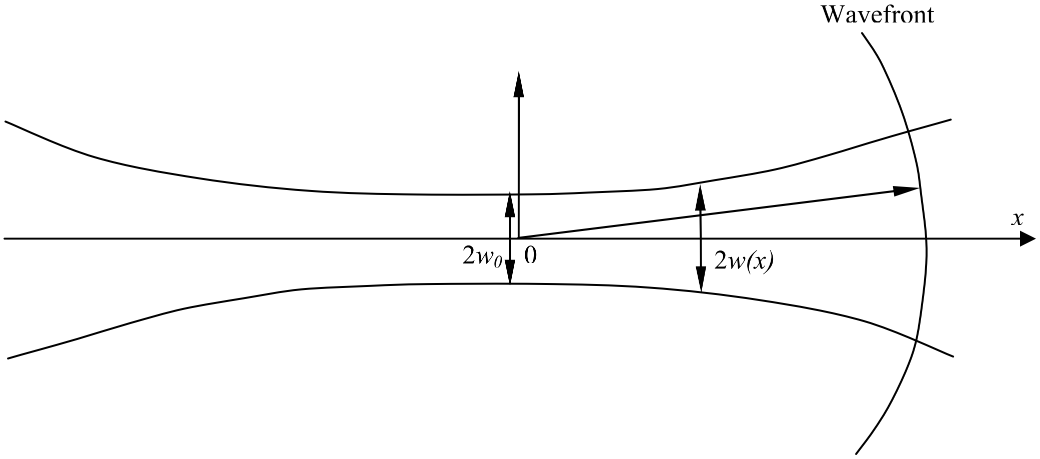

Fig. 4.9. Schematic of a wavefront of a laser beam.

The beam size will increase, slowly at first, then fast, eventually increasing proportionally to *x*. The wavefront radius of curvature, which was infinite at *x=0*, will become finite and initially decrease with *x*. At some point it will reach a minimum value, then increase with larger *x*, eventually becoming proportional to *x*. The equations describing the Gaussian beam radius *w(x)* and wavefront radius of curvature *R(x)* are

$$w^2(x) = {w_0}^2\left[1+\left(\frac{\lambda x}{\pi {w_0}^2}\right)^2\right] \quad , \tag{113}$$

$$R(x) = x\left[1+\left(\frac{\pi {w_0}^2}{\lambda x}\right)^2\right] \quad , \tag{114}$$

where w_0 is the beam radius at *x=0* and λ is the wavelength. The entire beam behavior is specified by these two parameters, and because they occur in the same combination in both equations, they are often merged into a single parameter, x_R, the Rayleigh range:

$$x_R = \frac{\pi w^2}{\lambda} \quad . \tag{115}$$

In fact, it is at $x = x_R$ that R has its minimum value.

At large distances from a beam waist, the beam appears to diverge as a spherical wave from a point source located at the center of the waist. Note that "large" distances mean where $x >> x_R$ is typically very manageable considering the small area of most laser beams. The diverging beam has a full angular width θ (again, defined by $1/e^2$ points) defined as

$$\theta = \frac{4\lambda}{2\pi w_0} \quad . \tag{116}$$

We have invoked the approximation $\tan\theta = \theta$ since the angles are small. Since the origin can be approximated by a point source, θ is given by geometrical optics as the diameter illuminated on the lens, *D*, divided by the focal length of the lens, *f*, as

$$\theta = \frac{D}{f} = \left(f/\#\right)^{-1} \tag{117}$$

where *f/#* is the photographic *f*-number of the lens.

Equating Eqs 116 and 117 allows us to find the beam waist diameter in terms of the input beam parameters, i.e.,

$$2w_0 = \left(\frac{4\lambda}{\pi}\right)\left(\frac{f}{D}\right) \quad . \tag{118}$$

We can also find the depth of focus from the formulas above. Usually the depth of focus is defined as the distance between the values of *x* where the beam radius is $\sqrt{2}$

times larger than it is at the beam waist, then using the equation for *w(x)* we can determine the depth of focus, *DOF*, as

$$DOF = \left(\frac{8\lambda}{\pi}\right)\left(\frac{f}{D}\right)^2 \quad . \tag{119}$$

The variations of the laser power distribution have significant effects on the resultant thermal and mechanical behaviors of the workpiece during laser material processing. In fact, beam divergence and aberrations at the focus and changing the size of the beam near the waist need to be studied in details in order to simulate the real condition, as they showed strong effect on the profile of the drilled holes (Olson and Swope, 1992).

4.4.2. Consideration of energy absorption

According to thermodynamic theory, the general expression of energy required for laser micromachining process can be determined as (Duley, 1999; Pryputniewicz, 2004)

$$E = \rho V\left[c_s\left(T_m - T_{amb}\right) + c_l\left(T_v - T_m\right) + L_m + L_v\right] \quad , \tag{120}$$

where E is the required energy, V is the volume of the melted material, c_s and c_l are the specific heats of the workpiece material in solid and liquid phases, respectively, T_m is the melting temperature, T_{amb} is the ambient temperature, T_v is the vaporization temperature, L_m and L_v are the latent heats of melting and vaporization, respectively. For laser microwelding, which has no material removal, the terms for $c_l\left(T_v - T_m\right)$ and the latent heat of vaporization L_v, in Eq. 120, should be considered zero since there is no vaporization introduced. For rough estimate, the volume of the melted workpiece material can be considered as a cylindrical volume that has the radius of the laser beam spot radius ω, and the height of the thickness of the workpiece.

Using Eq. 120, orders of magnitude of energies needed to bring a “volume” of material from its initial temperature to melting temperature, to melt this volume, to bring the molten volume to vaporization temperature, and finally to vaporize it can be determined. For example, for a copper workpiece of 0.1 mm thick, the first three energies are about one order of magnitude lower than the last energy, i.e., the energy needed to vaporize the volume. Therefore, it is important to know the fraction of the volume that is vaporized, in a specific process, in order to determine the amount of energy needed for the process.

For the energy absorption at the workpiece surface, absorption by electrons need to be considered as for the case of laser radiation incident on the surface of a metal. An electron that absorbs a laser photon makes a transition from one continuum state, E_i, to another state, E_f, with $E_f - E_i = h\nu$, the energy of the laser photon. The absorption of laser photons may be considered to instantaneously deposit energy at the site at which absorption occurs. In metals, this corresponds to a depth δ where

$$\delta = \frac{\lambda}{4\pi k} \quad , \tag{121}$$

where λ is the laser wavelength, k is the imaginary part of the refractive index m, that is

$$m = n - ik \quad , \tag{122}$$

where n is the real part of the refractive index.

If S is the area of the laser beam on the metal surface, then only electrons within the volume $V \sim S\delta$ absorb laser photons. These electrons will have speeds of $v \sim 10^8$ cm/sec and will lose their excess energy over a distance of $l - 10^{-6}$ cm through collision with other electrons. Because $l \leq \delta$, the energy absorbed from the laser beam is deposited with a distance δ from the surface. The heat source on absorption of Nd:YAG laser radiation by a metal therefore can be considered to be localized at the surface.

Part of the laser beam irradiated on the surface of the workpiece is reflected back into ambient due to reflectivity, which for some metals can be very high. For an opaque material such as a metal the absorptivity A is (Duley, 1999; Ordal et al., 1985)

$$A = \frac{4n}{(n+1)^2 + k^2} \quad . \tag{123}$$

Because both n and k are usually >>1 for metals at infrared wavelengths, A is small, and therefore only a small fraction of incident laser radiation is initially absorbed.

The surface reflectivity R can then be calculated as

$$R = 1 - A \quad . \tag{124}$$

Therefore, the amount of energy required for micromachining process, E_{req}, can be determined as

$$E_{req} = \frac{E}{A} \quad . \tag{125}$$

The values of the complex refractive index for stainless steel irradiated using the wavelength of 1.06 μm are k=4.44 and n=3.81, and k = 6.93 and n = 0.15 for copper (Steen, 1991). Therefore, the absorptivities, based on Eq. 123, were calculated to be

0.356 and 0.012 for stainless steel and copper, respectively. These values were used in the analytical and computational investigations in this Dissertation.

The absorptivity may be enhanced by a variety of factors, including temperature, surface roughness, oxidation, and changes in morphology. It also changes at the melting point, as shown in Fig. 4.10 (Steen, 1998). The effect of an increase in absorptivity is to accelerate the deposition of energy from an incident laser beam, which in turn can result in a singularity in the overall heating process at specific combinations of laser intensity and irradiation time. This effect can be useful in tailoring laser pulse profiles for particular welding operations.

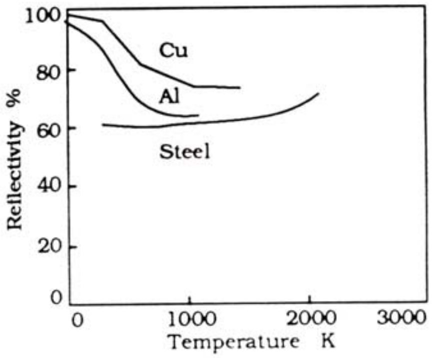

Fig. 4.10. Reflectivity for different metals as the function of temperature.

Thinner films also can enhance coupling of laser radiation to the surface if they are strongly absorbent. The absorption coefficient α can be calculated as

$$\alpha = \frac{4\pi k}{\lambda} \quad . \tag{126}$$

If I_0 is the laser intensity at the surface of the film, then the intensity at the depth z is

$$I(z) = I_0 e^{-\alpha z} \cong (1 - \alpha z) I_0 \quad . \tag{127}$$

Oxidation of a heated metal surface occurs rapidly at the temperatures reached during laser welding. This effect can be minimized through the use of an inert shielding gas such as He or Ar but likely occurs to some extent even with shielding. Because the enhancement in laser coupling provided by an absorbing thin film is important primarily in the initial heating phase, these oxide layers will not have much effect during welding but can influence the threshold intensity for surface melting and vaporization.

Surface roughness can have an important effect on laser coupling when the root-mean-square roughness $\sigma \geq \lambda$. The reflectivity R^* of an opaque surface at normal incidence becomes

$$R^* = R \cdot e^{-\left(\frac{4\pi\sigma}{\lambda}\right)^2} , \tag{128}$$

where R is the normal incidence reflectivity of the smooth surface. The reduction in reflectivity arises from a diffusely scattered component that redirects incident laser radiation at a range of angles away from the normal to the surface.

4.4.3. Consideration of plasma formation

In laser micromachining, a plume is usually produced as the result of the ejection of material from the micromachined area. The vaporized material is ejected and moves through the incident beam where it may be heated to temperatures in excess of the vaporization temperature. This heating arises, in large part, through collisions with energetic electrons. Under certain conditions, the overall effect is to produce a rapid increase in the level of ionization within the plume with the formation of the plasma (Duley, 1999).

Location of the plasma in laser micromachining is time and intensity dependent. Under certain conditions, the plasma appears to evolve from inside the keyhole into the ambient medium. At a relatively low laser intensity, the plasma remains attached to the entrance of the keyhole and is not important in attenuating incident laser radiation. At higher laser intensity, the plasma separates from the surface, but still is relatively stable. Further heating produces instabilities as the plasma is sufficiently heated to interrupt the laser beam. The plasma then explosively separates from the surface. At very high laser intensities, a stable plasma geometry is observed to extend back from the entrance to the keyhole toward the laser. Such plasmas are strong absorbers of incident laser radiation and can dissipate a significant fraction of laser power before it arrives at the target.

Plasmas can be an important part of micromachining with high power laser radiation and they modify coupling of laser radiation into the workpiece, often on a rapidly varying time scale. Plasmas are a potential source of micromachining defects such as lack of penetration, porosity, and compositional changes. Existence of a plasma, however, provides radiation that can be sampled using optical and acoustic detectors and represents a useful monitor of micromachining conditions. In this Dissertation, characteristics of the plasma formed during laser micromachining processes, such as the density of the plasma and the excitation temperature, will be discussed, as they can be used to estimate absorption coefficient of the laser beam power on the workpiece surface.

A plume commonly accompanies laser welding under other than conduction-limited conditions. This plume is the result of the ejection of material from the area of the weld and is due to laser heating. In an ideal welding system, no vaporization would be produced, even when the surface of the material has been disturbed in response to melting at the focus of the laser beam. In practice, some vaporization always occurs at the laser intensities required for welding. This vaporized material is ejected at a thermal velocity and moves through the incident beam, it may be heated to temperatures greatly in excess of the vaporization temperature. This heating arises, in large part, through collisions with energetic electrons. Under certain conditions, the overall effect is to produce a rapid increase in the level of ionization within the plume with the formation of a plasma.

The conversion of a plume into a plasma can occur only if a mechanism exists for energy deposition on a time scale that is fast compared with the expansion time of the plume. In general, this cannot occur via direct absorption of incident laser photons by atoms because usually no resonance exists between the photon energy and atomic transition energies. A resonance does exist, however, for transitions between continuum states of electrons in the field of a nearby ion. Such transitions are allowed for all photon energies and provide the means by which electrons may be rapidly excited to states of high kinetic energy through absorption of laser photons. This inverse Bremsstrahlung process removes energy from the incident laser beam and redirects this energy into heating of the gas. At high electron densities, inverse Bremsstrahlung leads to rapid heating and a large attenuation coefficient for incident laser radiation. Decoupling of laser radiation from the surface of the target may occur under these conditions, and this can be responsible for an interruption in the welding process.

Plasma heating by inverse Bremsstrahlung is initiated through the presence of a low density of “seed” electrons in the plume. These electrons are produced through thermal ionization of vaporizing atoms and through thermionic emission. The density of these electrons may be estimated from the equilibrium between ionization and recombination at the vaporization temperature and typically is many orders of magnitude smaller than the electron densities measured in laser-produced plasmas.

The location of the plasma in laser welding is time and intensity dependent. Under certain conditions, the plasma appears to evolve from inside the keyhole into the ambient medium. At a relatively low laser intensity, the plasma remains attached to the entrance of the keyhole and is not important in attenuating incident laser radiation. At higher laser intensity, the plasma separates from the surface but still is relatively stable. Further heating produces instabilities as the plasma is sufficiently hated to interrupt the laser beam. The plasma then explosively separates from the surface. At very high laser intensities, a stable plasma geometry is observed to extend back from the entrance to the keyhole toward the laser. Such plasmas are strong absorbers of incident laser radiation and can dissipate a significant fraction of laser power before it arrives at the target.

Plasmas can be an integral part of laser machining with high power laser radiation and that they modify the coupling of laser radiation into the workpiece, often on a rapidly varying time scale. Plasmas are a potential source of welding defects such as lack of penetration, porosity, and compositional changes. The existence of the plasma, however, provides radiation that can be sampled using optical and acoustic detectors and represents a useful monitor of welding conditions.

Plasmas are characterized by their level of ionization and their excitation (Cambel, 1963). The level of ionization is given by the ratio of electron density n_e to the total gas density n. In plasmas above the laser focus during laser welding of metals, n_e is typically 10^{15} to 10^{17} cm^{-3} at atmospheric pressure ($n_0 = 2.7 \times 10^{19}$ cm^{-3}). The level of ionization then is at most 0.5%. The plasma that is formed within the keyhole during welding may have a higher degree of ionization in response to laser heating via inverse Bremsstrahlung, although measurements suggest that even under keyhole conditions, the plasma is less than completely ionized. In such weakly ionized plasmas, $n_e = n_i$, where n_i is the density of singly ionized atoms. With the assumption of local thermodynamic equilibrium (LTE), the relative population of excited states can be described by a Boltzmann distribution at an excitation temperature T_e that is assumed to apply to all plasma components. Under these conditions, the densities of plasma species are given by the Saha equation

$$\frac{n_e n_i}{n_0} = \frac{g_i g_e}{g_0} \frac{(2\pi m_e k T_e)^{3/2}}{h^3} \exp\left(\frac{-E_i}{kT_e}\right) \quad , \tag{129}$$

where m_e is the electron mass, and g_e, g_i, and g_0 are the degeneracy factors for electrons, ions, and neutral atoms, respectively, E_i is the ionization potential for the neutral atoms in the gas. Equation 129 is subject to its limitations, can be used to relate n_e and T_e to the intensity of spectral lines emitted from the laser plasma. With $n_e = n_i$, Eq. 129 can be rewritten as

$$n_e = A n^{1/2} T_e^{3/4} \left[\exp\left(-\theta / T_e\right)\right]^{1/2} \ , \tag{130}$$

Numerical values for A and θ for several elemental gases are given in Table 1. Both g_i and g_0 can be large for atoms such as Fe that have many energy levels near the ground state.

Table 1. Atomic constants for various atoms and ions and values for A and θ in Eq. 130. (Note: g_e=2).

Element	g_i	g_0	A ($\mathrm{cm^{-3/2}\ {}^\circ K^{-3/4}}$)	θ (°K)
He	2	1	9.8×10^7	285,300
Ar	2	1	9.8×10^7	182,900
Al	1	6	2.8×10^7	69,400
Fe	30	25	7.6×10^7	91,700
Zn	2	1	9.8×10^7	109,000

Equation 130 can be used to estimate the initial concentration of electrons that are the seed electrons that initiate plasma heating via inverse Bremsstrahlung. With T_e replaced by T_v, the vaporization temperature, n_e, is about $1.45 \times 10^8\ \mathrm{cm^{-3}}$ for Fe (T_v=3300°K).

The absorption and scattering of incident radiation by a weakly ionized plasma are determined by the electron density with the refractive index approximately given by

$$n = \left(1 - n_e n_c\right)^{1/2} \ , \tag{131}$$

where n_c is a critical electron density:

$$n_c = \frac{m_e \varepsilon_0 w^2}{e^2} = 3.14 \times 10^{-10} w^2 \left(cm^{-3}\right) \quad , \tag{132}$$

where ε_0 is the permittivity of free space, and w is angular frequency. For CO_2 laser radiation, $w = 1.78 \times 10^{14}$ rad/sec, and $n_c = 10^{19} cm^{-3}$. When $n_e < n_c$, the refractive index is real and radiation can propagate through the plasma; it is only when $n_e = n_c$ that radiation is prevented from entering the plasma. Thus, it is evident that the reflection of 10.6 and 1.06 μm laser radiation is unimportant at the electron densities commonly observed during laser welding of metals. As a result, incident laser radiation will be transmitted through such plasmas. Absorption of this transmitted radiation by electron-ion pairs leads to plasma heating with a increase in n_e and T_e.

The absorption and dissipation of incident laser radiation by the laser plasma can be obtained from the following time-dependent equations:

$$\frac{dn_e}{dt} = R_i - R_d - R_r \quad , \tag{133}$$

$$n_e \frac{d\bar{\varepsilon}}{dt} = \alpha I - P_C - P_L \quad , \tag{134}$$

where R_i, R_d, and R_r are electron production, diffusion, and recombination rates, respectively; $\bar{\varepsilon}$ is average electron energy, α is the absorption coefficient for laser radiation, I is laser intensity, P_c is the power loss from elastic collisions, and P_L is the power loss from inelastic collisions. The condition for rapid plasma heating is that the rate of energy input αI exceeds the power loss due to elastic collisions. This requirement can be written as (Miyamoto, 1986)

$$\alpha I = 2n_e \frac{m_e}{M} v\bar{\varepsilon} \quad , \tag{135}$$

where M is the mass of a neutral atom, and v is the collision frequency. The mean electron energy will be some fraction of E_i. With $\bar{\varepsilon} \approx 0.1E_i$,

$$\alpha I \sim \frac{n_e m_e}{5M} v E_i \quad . \tag{136}$$

The inverse Bremsstrahlung absorption coefficient is (assuming LTE conditions)

$$\alpha\left(m^{-1}\right) = \frac{n_e n_i Z^2 e^6 2\pi}{6\sqrt{3} m \varepsilon_0{}^3 c h w^3 m_e{}^2} \left[\frac{m_e}{2\pi k T_e}\right]^{1/2} \left[1 - \exp\left(-\frac{w}{kT_e}\right)\right] \bar{g} \quad , \tag{137}$$

where Z is the average ionic charge in the plasma, h is Planck's constant, c is the speed of light, and $\bar{g}$ is the quantum mechanical Gaunt factor, which typically is 1.3 to 1.6 for laser welding plasmas at 10.6 µm. For CO_2 or YAG laser radiation and plasma with $T_e \sim 8 \times 10^3\ {}^{o}\mathrm{K}$, $1 - \exp\left(-hw/kT_e\right) \sim hw/kT_e$, the equation above becomes

$$\alpha\left(m^{-1}\right) = \frac{n_e n_i Z^2 e^6 \bar{g}}{6\sqrt{3} m \varepsilon_0{}^3 c w^2 (2\pi)^{1/2}} \left[\frac{1}{\left(m_e k T_e\right)^{3/2}}\right] \quad . \tag{138}$$

For weakly ionized plasma with Z=1, $\bar{g}$=1.5, m=1.0, and $w = 1.78 \times 10^{14}$ rad/sec, Eq. 138 becomes

$$\alpha\left(m^{-1}\right) \sim \frac{3.3 \times 10^{-39} n_e{}^2}{T_e^{3/2}} \quad , \tag{139}$$

where n_e is given in meters^{-3} and T_e is given in K. Therefore, with $n_e = 10^{23} m^{-3}$ and $T_e = 10^4 K$, $\alpha = 33.3 m^{-1}$, or 0.33 cm^{-1}.

4.4.4. Consideration of shielding gas

During the procedure of laser beam interaction with metals, the shielding gas can prevent oxidation of the machined spots and create the slag in the vicinity of the fusion zone, it can also affect formation of plasma which may block the beam and thus reduce the absorption of the beam into the workpiece. The formation of plasma is thought to occur through the reaction of the metal vapors from the keyhole with the shielding gas. The plasma formed above the keyhole with the shielding gas will be absorbing to an extent determined by the temperature and the ionization potential of the gases involved.

The plasma blocking effect will be less for those gases having a high ionization potential. Thus helium is favored, in spite of its high cost, as the top shroud gas in laser machining. The shroud underneath the cut/drill/weld would be of a less expensive gas, e.g., A_r, N_2, or CO_2. The difference in penetration can be significant (Steen, 1991). The plasma blocking is higher with higher powers. At slow speeds there is an advantage for helium, but at high speeds there is an advantage for argon. The explaination is that the plasma is both good and bad in aiding absorption. If the plasma is near the workpiece surface or in the keyhole it is beneficial. If, however, it is allowed to become too thick to leave the surface, its effect is to block or disperse the beam (Steen, 1991).

To eject the molten material, coaxial and non-coaxial nozzles are usually used (Penz et al., 1998). An axial nozzle leads to a high pressure in the area of the erosion front, a very small pressure gradient, and a low gas velocity. Thus, this arrangement is not sufficient and leads to a low ablation rate. One simple solution to improve the process efficiency is to move the center of the nozzle out of the center-line of the laser beam.

A further solution to obtain a higher ablation rate is to incline the workpiece in respect to the gas flow to move the stagnation zone out of the erosion front. Experiments show that the ablation rate increases significantly with an increasing angle. The laser planing process uses an off-axis gas nozzle. On the other hand, for a tangential gas flow the ablation rate is very low because the gas detaches above the erosion front. Above the erosion front a region with high pressure will be formed, thus the gas flow bends away from the interaction zone. To reduce this effect, the off-axis nozzle has to be shifted behind the erosion front.

4.4.5. Consideration of surface emissivity

The absorption of laser beam energy and heat loss due to radiation at the workpiece surface strongly depend on the surface emmisivity, ε. In most of the passed researches, the value of surface emmisivity ε has been considered as a constant for simplification. However, the surface emissivity is complicated as it is a function of the temperature of the workpiece, the wavelength and the monochromatic hemispherical emissivity of the real surface, which can be expressed as

$$\varepsilon(T) = \frac{1}{\sigma T^4} \int_0^\infty E_\lambda(\lambda, T) d\lambda = \frac{1}{\sigma T^4} \int_0^\infty \varepsilon_\lambda E_{b,\lambda} d\lambda \ , \tag{140}$$

where σ is the Stefan-Boltzmann constant, ε_λ is the weighted average of the monochromatic hemispherical emissivity, $E_{b,\lambda}$ is the blackbody monochromatic emissive power (Bejan, 1993).

In many instances, the measured $\varepsilon_\lambda(\lambda,T)$ value of a real surface is a complicated function of wavelength. The simplest approximation of this function is to take the emissivity constant with wavelength so that

$$\varepsilon_\lambda(\lambda,T) \equiv \varepsilon_\lambda(T) \ . \tag{141}$$

Under this simplification, the temperature, named the gray body temperature, T, is the surface temperature whose monochromatic hemispherical emissivity is independent of wavelength. Therefore, in the consideration of real procedure of laser interaction with metals, it should be noted that the surface emissivity is the function of temperature, so that the variation of this value with repect to the change of temperature needs to be included in calculations.

5. COMPUTATIONAL INVESTIGATIONS

In this chapter, first the solution of Eq. 1 is accomplished using an explicit finite difference approximation and the corresponding boundary conditions, as discussed in Section 5.1. Then, the heat transfer equations are solved with finite element method (FEM), as discussed in Section 5.2. Finally, the representative results for computational investigations are presented and discussed.

5.1. Finite difference method

In order to solve Eq. 1, finite difference method was used, and the approximations to model the governing equation were based on forward-difference in time and central-difference in space.

5.1.1. Finite difference process

To facilitate solution by finite difference method, the workpiece was subdivided into an array of nodes, Fig. 5.1 (Nowakowski, 1990; Han, 1999). There are four typical nodal elements that needed to be distinguished in order to describe the processes of heat transfer. These typical nodal elements are internal nodes, wall nodes, edge nodes, and corner nodes, as shown in Fig. 5.2.

For the most general case, the first law of thermodynamics and the Fourier's Law applied to the interior node give

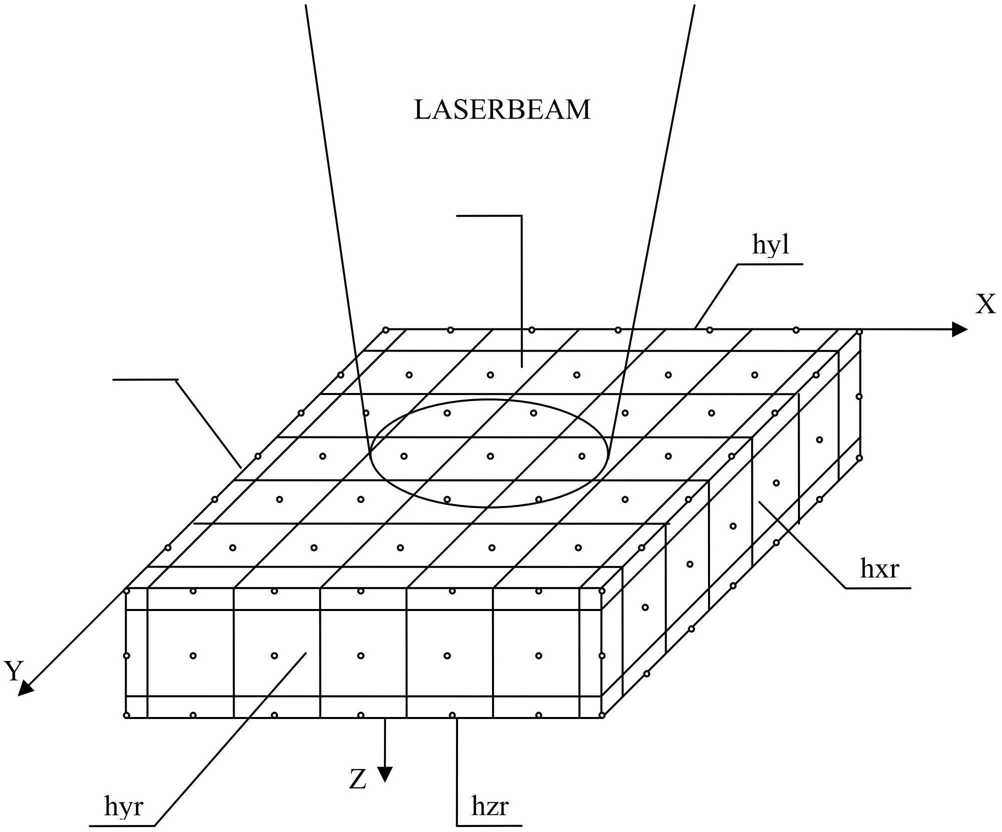

hxl – sum of convection and radiation coefficients on the workpiece surface with surface normal pointing in the negative x-direction,

hyl – sum of convection and radiation coefficients on the workpiece surface with surface normal pointing in the negative y-direction,

hzl – sum of convection and radiation coefficients on the workpiece surface with surface normal pointing in the negative z-direction,

hxr – sum of convection and radiation coefficients on the workpiece surface with surface normal pointing in the positive x-direction,

hyr – sum of convection and radiation coefficients on the workpiece surface with surface normal pointing in the positive y-direction,

hzr – sum of convection and radiation coefficients on the workpiece surface with surface normal pointing in the positive z-direction,

Fig.5.1. Three-dimensional finite difference subdivision of the workpiece.

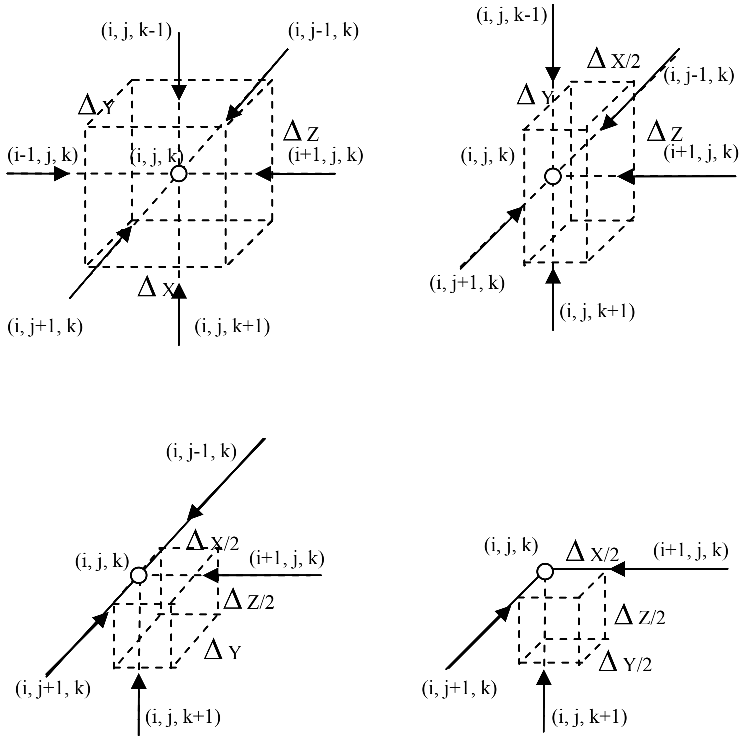

Fig. 5.2. The four typical nodal elements of a workpiece.

$$0 = (q_{i-1,j,k} + q_{i+1,j,k})\Delta y \Delta z + (q_{i,j-1,k} + q_{i,j+1,k})\Delta x \Delta z$$

$$+ (q_{i,j,k-1} + q_{i,j,k+1})\Delta x \Delta y + u^{'} \Delta x \Delta y \Delta z \quad , \tag{142}$$

where

$$q_{i-1,j,k} = -k \frac{T^{t}{}_{i-1,j,k} - T^{t}{}_{i,j,k}}{\Delta x} \quad , \tag{143}$$

$$q_{i+1,j,k} = -k \frac{T^{t}{}_{i+1,j,k} - T^{t}{}_{i,j,k}}{\Delta x} \quad , \tag{144}$$

$$q_{i,j-1,k} = -k \frac{T^{t}{}_{i,j-1,k} - T^{t}{}_{i,j,k}}{\Delta x} \quad , \tag{145}$$

$$q_{i,j+1,k} = -k\frac{T^t{}_{i,j+1,k} - T^t{}_{i,j,k}}{\Delta x} \quad , \tag{146}$$

$$q_{i,j,k+1} = -k\frac{T^t{}_{i,j,k+1} - T^t{}_{i,j,k}}{\Delta x} \quad , \tag{147}$$

$$q_{i,j,k-1} = -k\frac{T^t{}_{i,j,k-1} - T^t{}_{i,j,k}}{\Delta x} \quad , \tag{148}$$

$$u^{'} = \frac{\Delta u}{\Delta T} = \rho c\frac{T^{t+\Delta t}{}_{i,j,k} - T^t{}_{i,j,k}}{\Delta t} \quad . \tag{149}$$

The heat fluxes shown in Eqs 143 to 148 are defined as conduction energy flux per unit area in the positive x direction, negative x direction, positive y direction, negative y direction, positive z direction, and negative z direction, respectively. Therefore, the governing relationship given by Eq. 142 can be written as

$$\begin{aligned} &\rho c\frac{T^{'}{}_{i,j,k} - T_{i,j,k}}{\Delta t}(\Delta x\Delta y\Delta z) = k\frac{T_{i-1,j,k} + T_{i+1,j,k} - 2T_{i,j,k}}{\Delta x}(\Delta y\Delta z) \\ &+ k\frac{T_{i,j-1,k} + T_{i,j+1,k} - 2T_{i,j,k}}{\Delta y}(\Delta x\Delta z) + k\frac{T_{i,j,k-1} + T_{i,j,k+1} - 2T_{i,j,k}}{\Delta z}(\Delta x\Delta y) \end{aligned} \quad . \tag{150}$$

Rearranging Eq. 150 yields

$$\begin{aligned} T^{'}{}_{i,j,k} - T_{i,j,k} = &\frac{\kappa\Delta t}{\Delta x^2}(T_{i-1,j,k} + T_{i+1,j,k}) + \frac{\kappa\Delta t}{\Delta y^2}(T_{i,j-1,k} + T_{i,j+1,k}) + \frac{\kappa\Delta t}{\Delta z^2}(T_{i,j,k-1} + T_{i,j,k+1}) \\ &- \left[2\kappa\Delta t\left(\frac{1}{\Delta x^2} + \frac{1}{\Delta y^2} + \frac{1}{\Delta z^2}\right)\right]T_{i,j,k} \quad , \end{aligned} \tag{151}$$

where κ is the thermal diffusivity defined as

$$\kappa = k / \rho c \quad . \tag{152}$$

Equation 151 is the general equation for the interior node based on the assumption that thermal conductivity is not a function of temperature.

The finite difference method (FDM) equations for all possible nodes are included in Appendix A in the Dissertation. In addition, the consideration of the case when thermal conductivity depends on temperature was included in the FDM model. Furthermore, the stability analysis for this FDM model will be discussed in order to guarantee the convergence of the solution.

5.1.2. Computer solution

The solution procedure adopted in this Dissertation was an explicit finite difference formulation of Eq. 1 and its corresponding boundary conditions of convection and radiation heat loss. The solution of Eq. 1 will be discussed in the following sections in this Dissertation. The resulting set of finite difference equation were solved using the algorithm outlined in Fig. 5.3.

For the derivation of equation for the general element, examination of the model geometry illustrated in Fig. 4.1 indicates that the inclusion of finite model dimensions introduces variations on the general discretization mesh illustrated in Fig. 5.1. As shown in Fig. 5.1, these variations produce volume elements corresponding to interior, wall, edge, and corner nodes. The general interior volume element is included for comparison. Note that in addition to changing boundary conditions for each element, the definition of interior, wall, edge, and corner nodes placed on the region boundaries leads to elements of varying sizes.

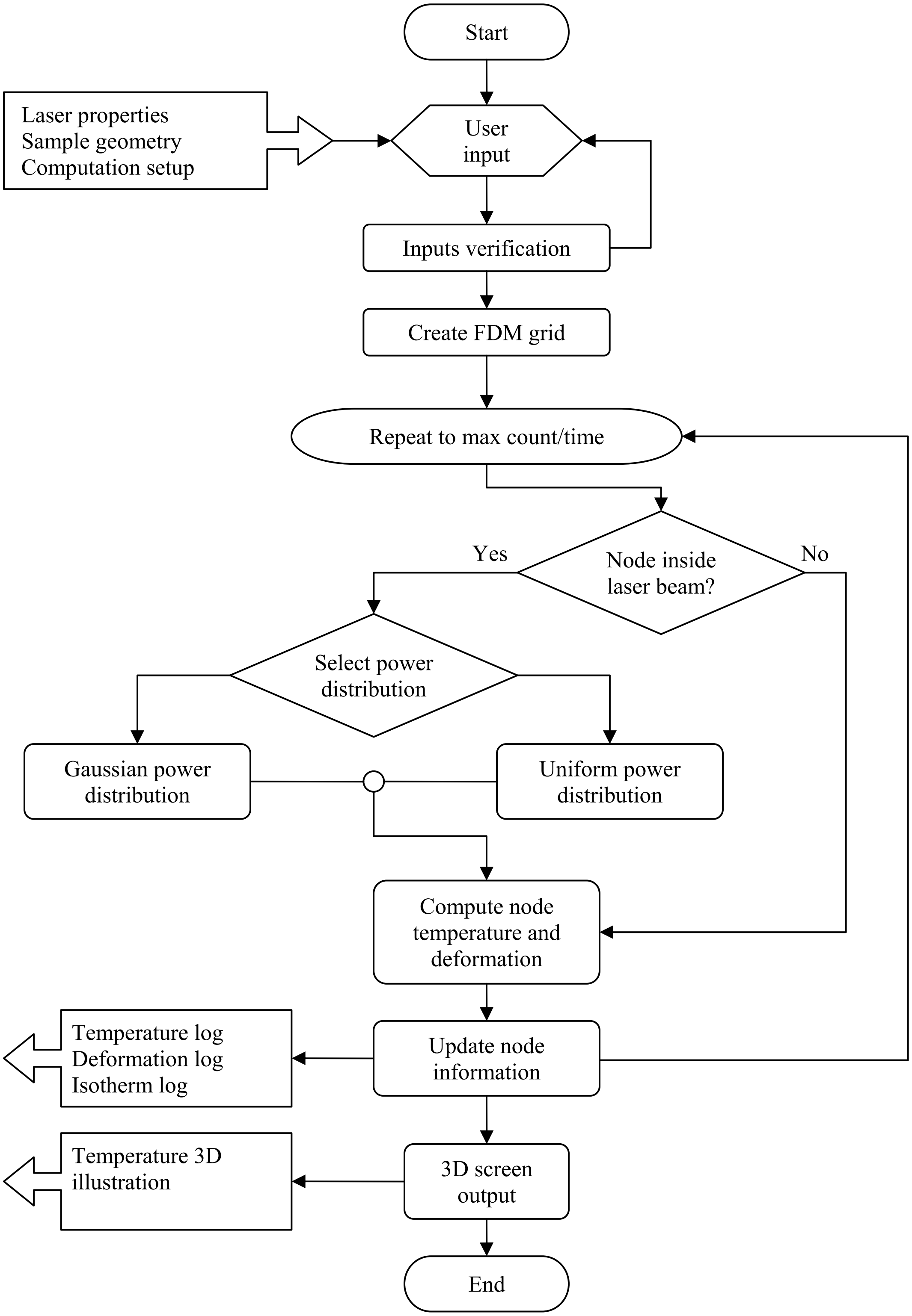

Fig. 5.3. Flow chart for the FDM process.

As a first step to develop a general node equation, consider the solution of Eq. 1 with constant thermal conductivity; the effects of variable thermal conductivity will be included later. Examination of the results of energy balances performed on the various volume elements shown in Fig. 5.1 offers insight to the form of this general equation. The detail of these calculations can be found in Appendix A. In this section, only the results are listed. According to Eq. A.12, temperature of an interior node can be determined as

$$\begin{aligned} T'_{i,j,k} - T_{i,j,k} &= \frac{\kappa\Delta t}{\Delta x^2}(T_{i-1,j,k} + T_{i+1,j,k}) + \frac{\kappa\Delta t}{\Delta y^2}(T_{i,j-1,k} + T_{i,j+1,k}) \\ &+ \frac{\kappa\Delta t}{\Delta z^2}(T_{i,j,k-1} + T_{i,j,k+1}) - \left[2\kappa\Delta t\left(\frac{1}{\Delta x^2} + \frac{1}{\Delta y^2} + \frac{1}{\Delta z^2}\right)\right]T_{i,j,k} \end{aligned} . \qquad (153)$$

Similiarly, for the wall node, temperature can be obtained from Eq. A.27 as

$$\begin{aligned} T'_{i,j,k} - T_{i,j,k} &= \frac{2\kappa\Delta t}{\Delta x^2}(T_{i+1,j,k}) + \frac{\kappa\Delta t}{\Delta y^2}(T_{i,j-1,k} + T_{i,j+1,k}) + \frac{\kappa\Delta t}{\Delta z^2}(T_{i,j,k-1} + T_{i,j,k+1}) \\ &- \left[2\kappa\Delta t\left(\frac{1}{\Delta x^2} + \frac{1}{\Delta y^2} + \frac{1}{\Delta z^2} + \frac{h_1}{k\Delta x}\right)\right]T_{i,j,k} \end{aligned} , \qquad (154)$$

where $$h_1 = h_{xl} + h_{i,j,k}{}^R = h_{xl} + \sigma\varepsilon T_{i,j,k}{}^3 . \qquad (155)$$

For the edge node, temperature can be obtained from Eq. A.20 as

$$\begin{aligned} T'_{i,j,k} - T_{i,j,k} &= \frac{2\kappa\Delta t}{\Delta x^2}(T_{i+1,j,k}) + \frac{2\kappa\Delta t}{\Delta y^2}(T_{i,j+1,k}) + \frac{\kappa\Delta t}{\Delta z^2}(T_{i,j,k-1} + T_{i,j,k+1}) \\ &- \left[2\kappa\Delta t\left(\frac{1}{\Delta x^2} + \frac{1}{\Delta y^2} + \frac{1}{\Delta z^2} + \frac{h_1}{k\Delta x} + \frac{h_2}{k\Delta y}\right)\right]T_{i,j,k} \end{aligned} , \qquad (156)$$

where

$$h_2 = h_{yr} + h_{i,j,k}{}^{R} = h_{yr} + \sigma\varepsilon T_{i,j,k}{}^{3} \ . \tag{157}$$

For the corner node, temperature can be obtained from Eq. A.19 as

$$\begin{aligned} T'_{i,j,k} - T_{i,j,k} = {} & \frac{2\kappa\Delta t}{\Delta x^2}(T_{i+1,j,k}) + \frac{2\kappa\Delta t}{\Delta y^2}(T_{i,j+1,k}) + \frac{2\kappa\Delta t}{\Delta z^2}(T_{i,j,k+1}) \\ & - \left[2\kappa\Delta t \left(\frac{1}{\Delta x^2} + \frac{1}{\Delta y^2} + \frac{1}{\Delta z^2} + \frac{h_1}{k\Delta x} + \frac{h_2}{k\Delta y} + \frac{h_3}{k\Delta z} \right) \right] T_{i,j,k} \end{aligned} , \tag{158}$$

where

$$h_3 = h_{zl} + h_{i,j,k}{}^{R} = h_{zl} + \sigma\varepsilon T_{i,j,k}{}^{3} \ . \tag{159}$$

Solution of this final formulation of Eq. 1 was obtained using computer software developed in this Dissertation. The effectiveness of this solution was subject to parameters defining operating characteristics of the laser beam, such as energy per pulse, pulse duration, and laser beam diameter. These characteristics were measured during the course of this Dissertation.

5.1.3. Model geometry

A typical FDM geometry of the problem is illustrated in Fig. 5.1. The origin of the Cartesian coordinate system is located at the top left corner of the workpiece and each face of the model has a unique heat transfer coefficients. Note that the elements corresponding to the surface, edge, and corner nodes are smaller than a typical interior element. This is due to the fact that nodes corresponding to these elements are placed on the boundaries defining the workpiece. Note also that the center of the irradiating laser beam is placed in the center of the top surface of the workpiece.

5.1.4. Simulation of laser beam intensity

In laser machining, the internal energy generation, Q, is commonly thought of as the rate of laser energy absorbed per unit volume of the irradiated medium. In the case of metals, this absorption occurs in a very thin layer at the surface of the workpiece and, for many practical cases, can be considered as a boundary condition to Eq. 1. For partially transparent media (e.g., thin layers of metal), this absorption process may be quantified using Beer's (or Lambert's) law (Nowak, 1990), i.e.,

$$I(z) = \varepsilon I(0) e^{-\alpha z} \quad , \tag{160}$$

where $I(z)$ is the power density of the incident radiation at a given distance, z, into the absorbing medium from the irradiated surface, $I(0)$ is the laser beam power density at $z = 0$, ε is the surface emissivity of the medium, and α is the absorption coefficient, a measure of the absorption of radiation propagating through the medium. Note that both ε and α are functions of local temperature and the wavelength of the incident radiation.

5.1.5. Convergence analysis

The first step in the convergence analysis is to get a finite difference equation into the form

$$T'_{i,j,k} - T_{i,j,k} \le G(\Omega - T_{i,j,k}) \ , \tag{161}$$

where G represents a collection of time and space terms, Ω represents a collection of space and temperature terms, and other parameters are defined in the nomenclature. To determine stability of Eq. 161, G must be evaluated (Conte and De Boor, 1980; Ferron, 1984). Therefore, using Eq. 156, it can be obtained that

$$G \ge \frac{T'_{i,j,k} - T_{i,j,k}}{\Omega - T_{i,j,k}} \ . \tag{162}$$

When G of Eq. 162 satisfies $0 \le G \le 1$, the stable condition can be obtained. Parameter G represents time and space terms and is defined as (Chanberland, 1988)

$$G = 2\kappa\Delta t\left(\frac{1}{\Delta x^2} + \frac{1}{\Delta y^2} + \frac{1}{\Delta z^2}\right) , \tag{163}$$

while Ω, containing space and temperature terms, is defined as

$$\Omega = \left[\frac{T_{i-1,j,k} + T_{i+1,j,k}}{\Delta x^2} + \frac{T_{i,j-1,k} + T_{i,j+1,k}}{\Delta y^2} + \frac{T_{i,j,k+1} + T_{i,j,k-1}}{\Delta z^2}\right]$$

$$\cdot\left[2\left(\frac{1}{\Delta x^2} + \frac{1}{\Delta y^2} + \frac{1}{\Delta z^2}\right)\right]^{-1} \ . \tag{164}$$

Then, using Eqs 163 and 164, Eq. 161 can be rewritten as

$$T'_{i,j,k} - T_{i,j,k} \le G(\Omega - T_{i,j,k}) \ . \tag{165}$$

For the stable conditions, $0 \le G \le 1$ is needed, i.e.,

$$2\kappa\Delta t\left(\frac{1}{\Delta x^2} + \frac{1}{\Delta y^2} + \frac{1}{\Delta z^2}\right) \le 1 \ . \tag{166}$$

Finally, solution of Eq. 166 yields

$$\Delta t \le \left[2\kappa \left(\frac{1}{\Delta x^2} + \frac{1}{\Delta y^2} + \frac{1}{\Delta z^2} \right) \right]^{-1} . \tag{167}$$

Equation 167 shows that in order for results for Eq. 161 to converge, the time increment Δt must not exceed the value based on the thermal diffusivity κ of the material of the work piece and the spatial size of the work piece defined by Δx, Δy, and Δz.

Since the real model is under the combination of conduction, convection, and radiation heat transfer, the convection and radiation heat loss on the six surfaces should be included in the finite difference model. Using the same method as that leading to Eq. 167, the critical time intervals for the different typical nodes can be determined to be

interior node
$$\Delta t \le \frac{1}{2\kappa \left(\frac{1}{\Delta x^2} + \frac{1}{\Delta y^2} + \frac{1}{\Delta z^2} \right)} , \tag{168}$$

corner node
$$\Delta t \le \frac{1}{4\kappa \left[\left(\frac{1}{\Delta x^2} + \frac{1}{\Delta y^2} + \frac{1}{\Delta z^2} \right) + \frac{1}{2\kappa} \left(\frac{h_1}{\Delta x} + \frac{h_2}{\Delta y} + \frac{h_3}{\Delta z} \right) \right]} , \tag{169}$$

edge node
$$\Delta t \le \frac{1}{4\kappa \left[\left(\frac{1}{2\Delta x^2} + \frac{1}{\Delta y^2} + \frac{1}{\Delta z^2} \right) + \frac{1}{2\kappa} \left(\frac{h_2}{\Delta y} + \frac{h_3}{\Delta z} \right) \right]} , \tag{170}$$

wall node
$$\Delta t \le \frac{1}{2\kappa \left[\left(\frac{1}{\Delta x^2} + \frac{1}{\Delta y^2} + \frac{1}{\Delta z^2} \right) + \frac{1}{\kappa} \left(\frac{h_2}{\Delta y} \right) \right]} , \tag{171}$$

where κ is the thermal diffusivity of the material of the work piece and h_1, h_2, and h_3 are the heat transfer coefficients in the directions parallel to the x, y, and z axis of the coordinate system, respectively, defined as

$$h_i = h_{c_i} + h_{r_i} . \tag{172}$$

In Eq. 172, subscript i denotes the specific coordinate axis, h_c is the convective heat transfer coefficient of the specific node, and h_r is the radiation heat transfer coefficient of the specific node. The convective heat transfer coefficient is defined, based on Eq. 7, as

$$h_c = N_u \frac{k_{air}}{L} , \tag{173}$$

while the radiation heat transfer coefficient h_r is defined as

$$h_r = 5.67 \cdot 10^{-8} \cdot \varepsilon \cdot (T^3 - T_{amb}{}^3) . \tag{174}$$

The parameters N_u, k_{air}, L, and ε are defined in Section 4.1.2.

5.2. Finite element method

In order to solve the governing equation of the heat transfer problem of the laser micromachining processes, finite element analysis was performed using thermal analysis system (TAS) software (Rotaso, 2002). Because of symmetry of the workpiece utilized in the experiments (1 cm by 1 cm by 0.1 mm), and the significant temperature gradient at the spot under the laser beam irradiance, the quarter-model of the center-piece with the dimensions of 2.5 mm by 2.5 mm by 0.1 mm was used in the FEM analysis.

Convergence analysis was first performed, with 1% convergent criteria is setup for the temperature calculation, which results in 36,000 elements that were used in the FEM model. The temperature distributions of the workpiece were calculated for the spatial and temporal variations. In addition, the thermal stresses and deformations due to the laser beam interaction with the workpiece were determined based on the calculated temperature distributions in the workpiece (Fan et al., 1998; Guan, 1998). Furthermore, for the study of two-part laser microwelding process, TAS is used with the variation of the materials on the bottom layer, as presented in the later sections.

5.3. Results of computational investigations

The material used in the study of laser microwelding is copper, and the dimensions of the workpiece are 1 cm by 1 cm by 0.1 mm. The density of the material is 8600 kg/m^3, the specific heat is 381 $J/kg°C$, and the thermal conductivity at 20 $°C$ is 0.389 *W/mm°K*.

5.3.1. Results of FDM calculations

Using Microsoft Visual C++, the finite difference algorithm was implemented in graphical interface application. Because of symmetry of the workpiece utilized in the experiments (1 cm by 1 cm by 0.1 mm), and the significant temperature gradient at the spot under the laser beam irradiance, the workpiece with the dimensions of 2.5 mm by 2.5 mm by 0.1 mm was used in the FDM computation. The user first needs to input the mesh size in three-dimensions, the interface would calculate and output the minimum time step in order to achieve convergence, as described in Section 5.2. Then, the user can input a time step which is less than the calculated minimum time step, also input the power, surface emissivity, laser pulse length, and number of iterations to compute. Also there are several selectable icons to choose for whether or not to consider Gaussian beam distribution, automatically adjust surface energy absorption coefficient due to temperature change, based on the data in Fig. 4.10, and also have the choice to track the temperature change as the function of time for a specific node by inputting its coordinate. Then the program will compute the overall temperature profiles, and output the temperature, convection and radiation heat loss of top central nodes, and melting isotherms into files. In addition, at the end of each computation, the quarter-model of temperature profiles at the end of the laser pulse is shown as a 3D graphic, and the temperatures are illustrated using a color palette, as shown in Fig. 5.4.

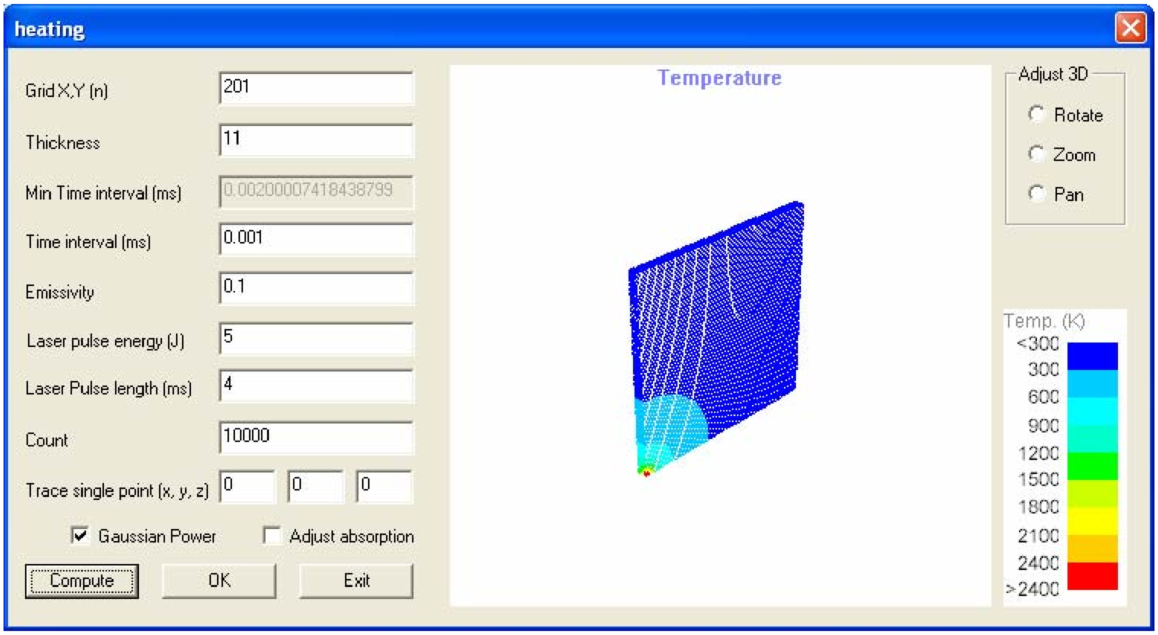
heating

Grid X,Y (n): 201
Thickness: 11
Min Time interval (ms): 0.00200007418438799
Time interval (ms): 0.001
Emissivity: 0.1
Laser pulse energy (J): 5
Laser Pulse length (ms): 4
Count: 10000
Trace single point (x, y, z): 0 0 0
☑ Gaussian Power ☐ Adjust absorption

Fig. 5.4. Computer interface of FDM computation, for temperature profile at the end of the laser pulse.

In order to obtain the FDM results, the convergence analysis was first conducted for the conditions of laser beam energy of 5 J and pulse length of 4 ms, and laser spot diameter of 80 μm. The temperature was calculated and summarized for the highest temperature at the time steps when the laser pulse was turned off, that is, when t = 4 ms for welding conditions. The convergence plot is shown in Fig. 5.5.

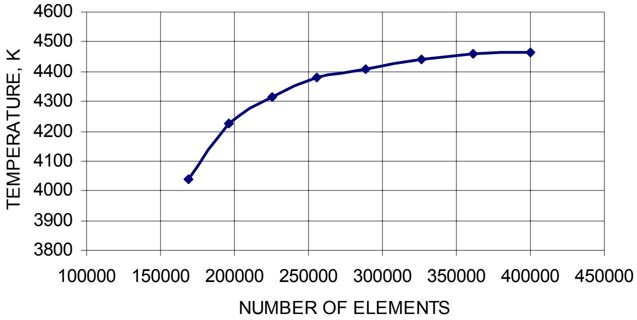

Fig. 5.5. Convergence analysis for the temperature distribution in the workpiece during laser microwelding process, based on the FDM computations for the workpiece.

Using 400,000 elements, the temperature of the workpiece of dimensions of 2.5 mm by 2.5 mm by 0.1 mm was first calculated for uniform power distribution. The laser energy used was 5 J with the pulse length of 4 ms, the energy absorption coefficient was 0.012, and the laser beam was focused to a spot of 80 μm in diameter. The temperature variations of the central nodes on top, middle, and bottom layers are shown in Fig. 5.6.

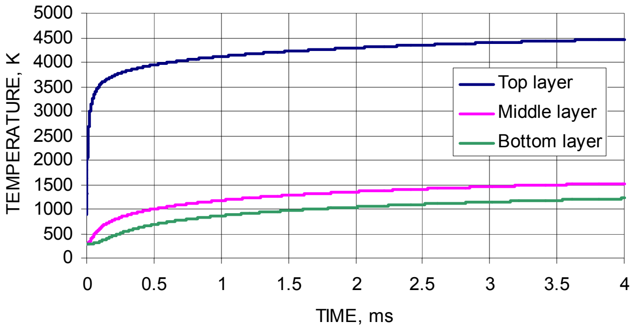

Fig. 5.6. Computational results of temperature variation of central nodes in the three layers, for uniform power distribution.

As shown in Fig. 5.6, at the beginning of laser beam irradiation, the temperature of the top central node increases dramatically. At the same time, temperatures of the middle and bottom layer nodes also increase, because of the conductive heat transfer. With the continuous laser beam irradiation, the temperatures of all the nodes on the workpiece increase. Since the central node on the top surface absorbs the laser beam directly, it has the highest temperature among the workpiece so that melting first occurs at this point. Note that the time for the top central node to reach melting temperature was very short, and this was verified using Eq. 11 in Chapter 4 for the estimation of the time for heating stage under the laser power used in the FDM model. While the top central node experiences melting, the workpiece continuously absorbs energy. After the input energy exceeding the latent heat of solid-liquid and liquid-vapor phase changes, the top central node vaporizes, so that plasma forms and the central node on the middle layer will indirectly absorb energy according to Beer’s Law, Eq. 41. This procedure will repeat for the central nodes on the middle and bottom layers. After the laser pulse time, there is no heat source input on the workpiece any more, so that the temperature of the top surface starts to drop. However, the middle and bottom layer nodes still absorb the heat conducted from the top surface, due to the temperature difference between them. After the nodes on top drop to the temperature equal to the temperature of the middle layer nodes, no more conduction heat will be transferred between them, so that they drop at exactly the same temperature gradient.

For different locations on the workpiece, the temperatures were calculated and compared. Because the laser power intensity is very high and the interaction time is very short, it has very little effects of the temperature change at the location of more than 1 mm away from the laser beam center. Figure 5.7 shows the calculated temperature difference on top layer between the central node and other nodes along the radial directions. Figure 5.7a shows representative temperature variations of the nodes within the laser beam radius, and Fig. 5.7b shows the difference between the central node and the nodes which are outside the laser beam radius.

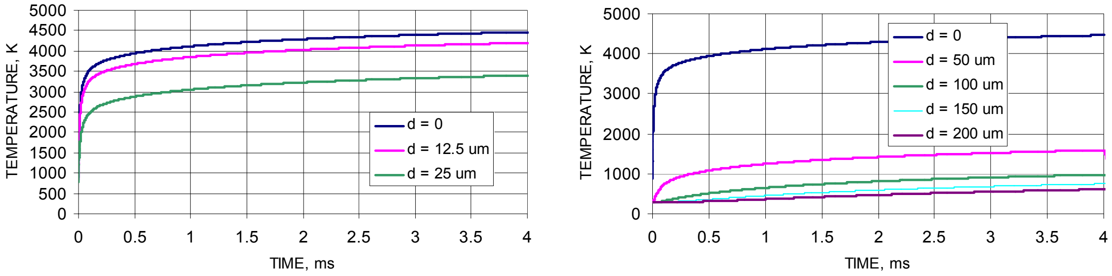

(a) (b)

Fig. 5.7. Computational results of temperature change at different locations on top layer, for uniform power distribution: (a) for the range of 25 μm, (b) for the range of 200 μm.

Figure 5.8 shows the calculated temperature difference on middle layer between the central node and other nodes along the radial directions. Figure 5.8a shows representative temperature variations of the nodes within the 25 μm range, and Fig. 5.8b shows the temperature history of the nodes along the radial direction for 200 μm range. In addition, the temperature histories for the nodes on the bottom layer are shown in Fig. 5.9.

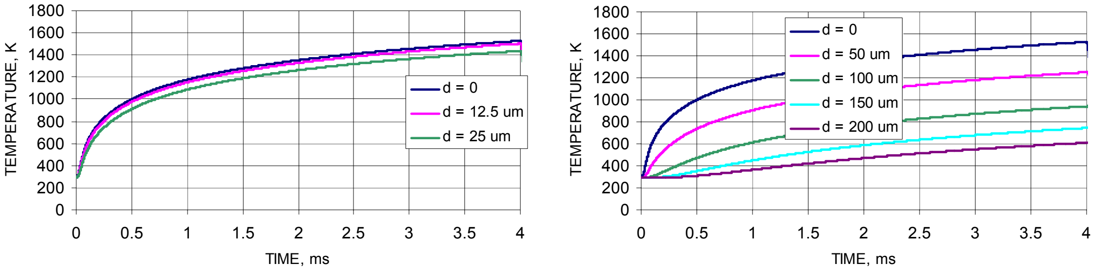

Fig. 5.8. Computational results of temperature change at different locations on middle layer, for uniform power distribution: (a) for the range of 25 μm, (b) for the range of 200 μm.

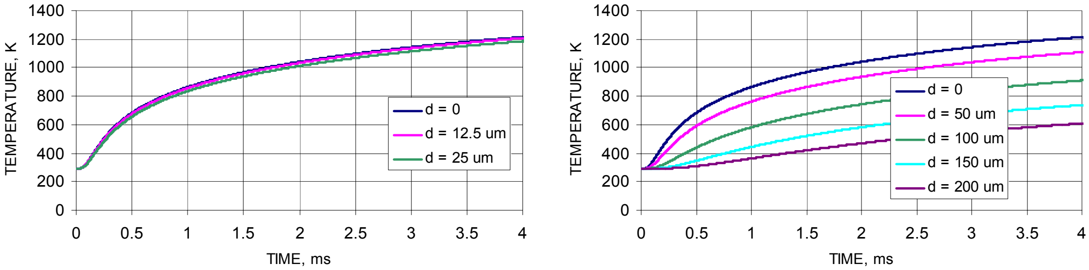

Fig. 5.9. Computational results of temperature change at different locations on bottom layer, for uniform power distribution: (a) for the range of 25 μm, (b) for the range of 200 μm.

According to the laser microwelding experiments performed in this Dissertation, laser energy of 5 J with the pulse length of 4 ms were used. Therefore, it is important to study the temperature distributions along the axial direction, that is, the bottom layer need to reach melting temperature in order to provide a fusion zone with the workpiece to be welded. The examination of axial temperature distributions were calculated at different time steps, as shown in Fig. 5.10. Note that at the end of laser pulse, the central node on bottom layer reached 1425°K, while the melting temperature for copper is 1173°K , indicating that melting occurs at this node, therefore, it can provide enough heat flux to the workpiece that need to be welded.

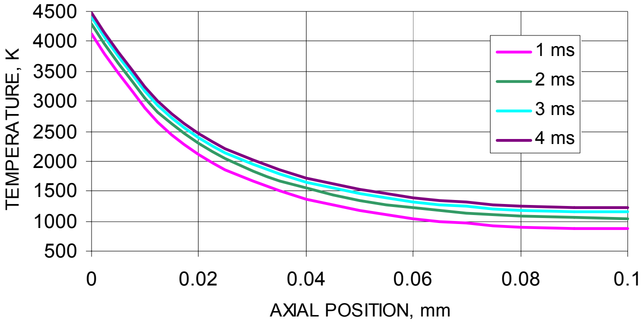

Fig. 5.10. Computational results of temperature distribution along the axial direction for different time steps inside the workpiece, for uniform power distribution.

The temperature gradients during laser micromachining are usually very large, due to the high power density and small focal area provided by the laser. Figure 5.11 shows the large temperature gradients at the workpiece top surface at different time steps, and it can be viewed that very high temperatures occur at the center of the workpiece, and it decrease very significantly as propagating along the radial direction, and for the nodes that more than 1 mm away from the center, the temperature drop down to very close to room temperature, indicating that most of the heat affected zone are localized within the 1 mm range.

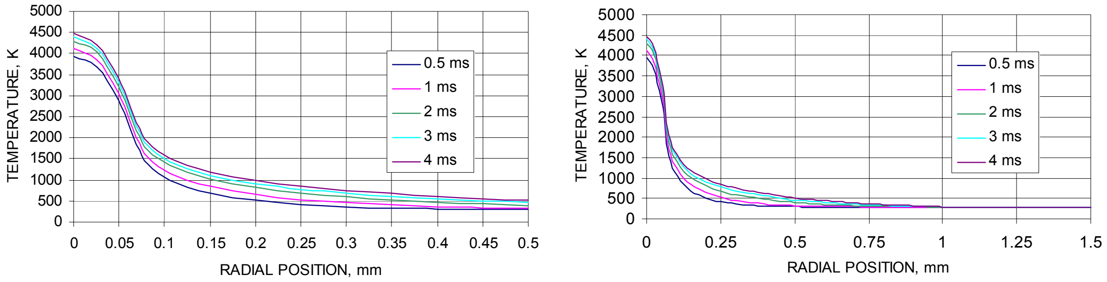

(a) (b)

Fig. 5.11. Computational results of temperature distribution along the radial direction for different time steps on top surface of the workpiece, for uniform power distribution: (a) for 0.5 mm in radial direction, (b) for 1.5 mm in radial direction.

For the temperature gradients in the middle and bottom layers, as shown in Fig. 5.12, the highest temperature in these layers are much lower than those in the top layer, and the temperature gradients for the middle and bottom layers are not as pronounced as in the top layer.

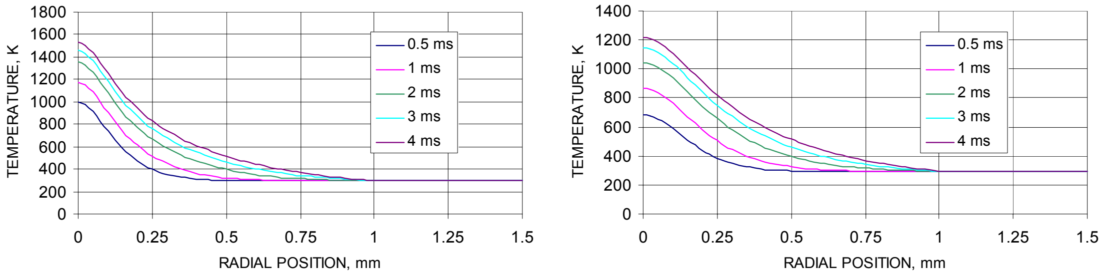

Fig. 5.12. Computational results of temperature distribution along the radial direction for different time steps within the workpiece, for uniform power distribution, for 1.5 mm in radial direction: (a) middle layer (b) bottom layer.

In the temperature output files, the isotherms of the nodes that are at the edge of the melting zone are recorded at different time steps, as shown in Fig. 5.13, which gives an estimate of how much material may experience melting, and the isotherms can be compared with the experimental results when using etching to view the modification of microstructure in the HAZ.

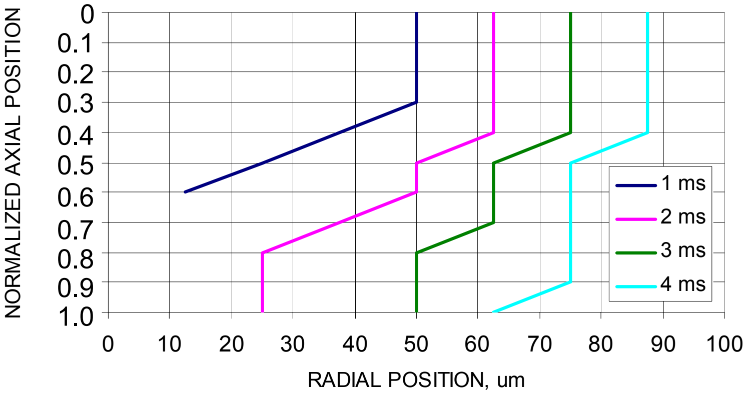

Fig. 5.13. Computational results of isotherms at melting temperature for different time steps within the workpiece, for uniform power distribution.

During the time the laser interacts with the workpiece, the control volume receives the energy input from the laser beam, and also it losses heat by the convection and radiation from the surfaces. As discussed in Chapter 4, both the convection and radiation heat loss are functions of temperature. Therefore, during the laser pulse, the convection and radiation heat losses of the workpiece increase as the temperature increase. From Eqs 3 to 7, the convection heat loss is proportional to the first power of temperature change. From Eq. 8, the radiation heat loss is proportional to the fourth power of the nodal temperature. Therefore, at the beginning when the laser starts to heat the workpiece, the convection heat loss is greater than the radiation heat loss. However, after reaching a certain temperature, the radiation heat loss will equal the convection heat loss, and after that, it will increase much more dramatically then the convection heat loss. The comparison of the convection and radiation heat losses of the top central node is shown in Fig. 5.14. The plateaus in the radiation heat loss curve were due to the consideration of the constant temperature when the workpiece was absorbing latent heat of melting and vaporization, respectively, and the radiation heat loss is proportional to the forth power of the nodal temperature.

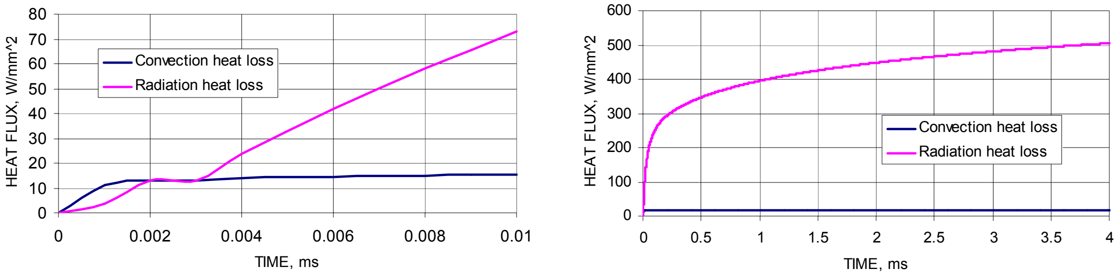

Fig.5.14. FDM result of convection and radiation heat losses on top central node, calculated for uniform power distribution, (a) for the first 0.01 ms, (b) for the 4 ms.

In addition, in the FDM computation developed in this Dissertation, effect of power distributions were considered for both uniform and Gaussian distributions, that is, for Gaussian distribution,

$$P(r) = P_0 \exp\left(-\frac{2r^2}{w_0{}^2}\right) \quad , \tag{175}$$

where $r=(x^2+y^2)^{0.5}$ is the distance of each node from the center of the laser beam. The temperature variations of the center nodes in top, middle, and bottom layers as the function of time are shown in Fig. 5.15, and the axial temperature profiles are shown in Fig. 5.16.

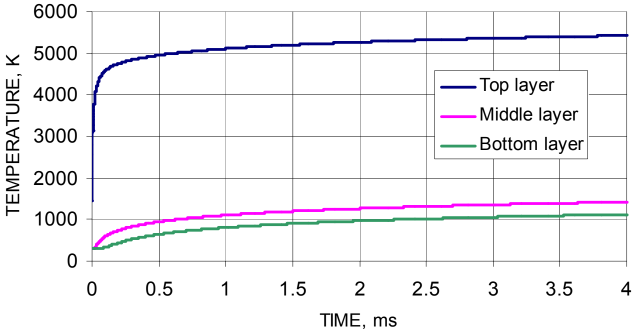

Fig. 5.15. Computational results of temperature variation of central nodes in the three layers, for Gaussian power distribution.

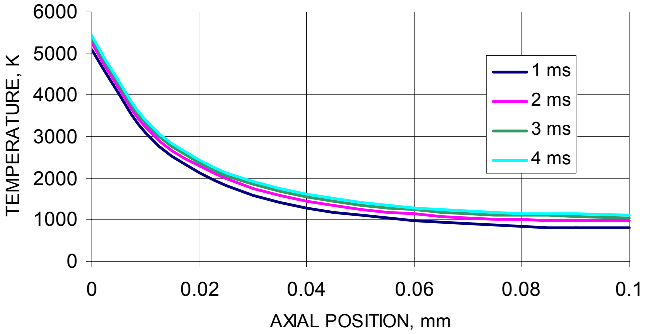

Fig. 5.16. Computational results of temperature distribution along the axial direction for different time steps inside the workpiece, for Gaussian power distribution.

The comparisons of the temperature profiles between the Gaussian and uniform power distributions are shown in Figs 5.17 and 5.18. Note that for both conditions, laser beam energy of 5 J and pulse length of 4 ms were used in the FDM calculations, based on the laser operation parameters used in the microwelding experiments, and laser spot diameter used in the FDM calculations was 80 μm. Figure 5.17a illustrates the temperature difference between the highest temperature within the workpiece, the maximum temperatures for uniform and Gaussian power distributions were about 4466°K and 5422°K, respectively. Figure 5.17b shows the temperature difference along the axial direction on top surface (where the temperature has its largest gradient among all the layers within the workpiece), where it can be viewed that the Gaussian beam profile increases the maximum temperature within the workpiece, but leads to the lower temperatures for the nodes toward the bottom, which produces a larger temperature gradient along the axial direction than the uniform power distribution. Figure 5.18 shows the comparison between uniform and Gaussian power distributions for the temperature gradients along radial direction on the top surface of the workpiece, where it can be observed for the similar phenomena as for the axial temperature gradients, that is, Gaussian power distribution results in larger temperature gradients than the uniform power distribution.

5.3.2. Results of FEM calculations

Based on the material properties the workpiece and the laser beam properties of the Nd:YAG laser used in the experiments, FEM results for the temperature distribution

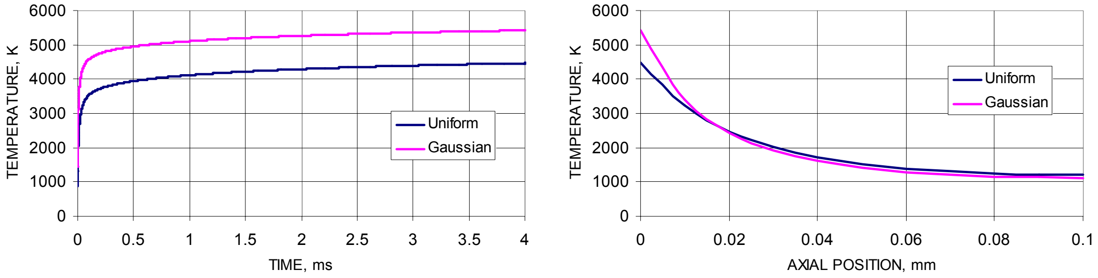

(a) (b)

Fig. 5.17. Comparison of FDM results of temperature distributions for uniform and Gaussian power distributions: (a) for central node on top surface, (b) for nodes along the axial direction at the end of the pulse (t = 4 ms).

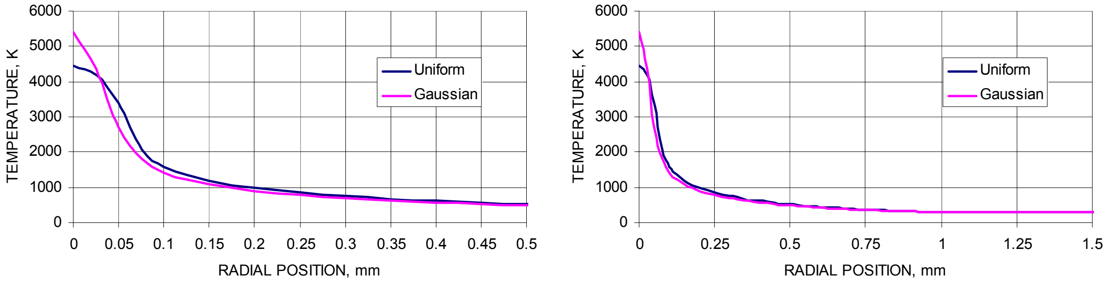

Fig. 5.18. Comparison of FDM results of temperature distributions for uniform and Gaussian power distributions for temperature gradient along radial direction on top surface at the end of the pulse (t = 4 ms): (a) for 0.5 mm in radial direction, (b) for 1.5 mm in radial direction.

of the laser microwelding process are calculated using Thermal Analysis System (TAS) software (Rosato, 2002). The dimensions used in the FEM calculation are 2.5 mm by 2.5 mm by 0.1 mm, the laser energy was 5 J, pulse duration was 4 ms, energy absorption coefficient was 0.012, and the laser beam was focused to a spot of 80 µm in diameter. A uniform power distribution was first used in TAS calculation. For the temperature calculation, convergence analysis was first performed, Fig. 5.19, which resulted in 36,000 elements that were used on the quarter-model of the workpiece. Therefore, the temperature variation within the quarter-model of the workpiece is shown in Fig. 5.20.

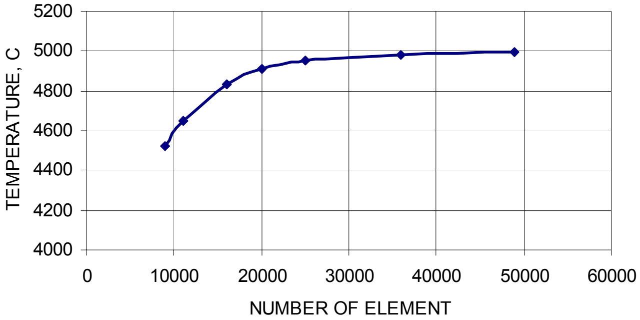

Fig. 5.19. Convergence analysis for the temperature distribution in the workpiece during laser microwelding process, based on the quarter-model computations using TAS.

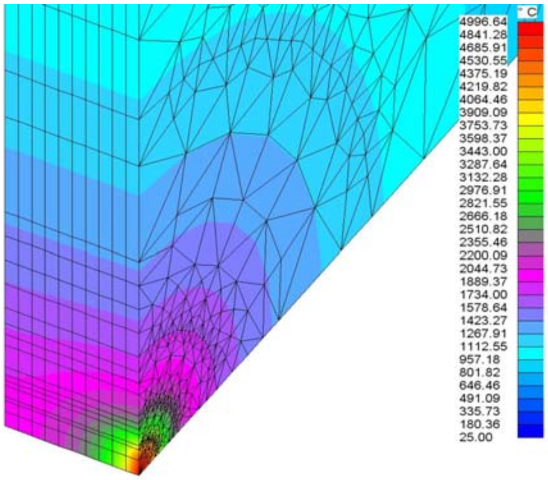

Fig. 5.20. Overall temperature distribution in the workpiece during laser microwelding process, based on the quarter-model computations using TAS, with uniform power distribution.

Also in the FEM calculation using TAS, effect of power distributions were further considered for both uniform and Gaussian distributions. The temperature distribution with Gaussian power distribution was calculated as shown in Fig. 5.21. Furthermore, the detailed temperatures with Gaussian and uniform distributions along the radial direction and axial direction are compared and shown in Figs 5.22 and 5.23, respectively.

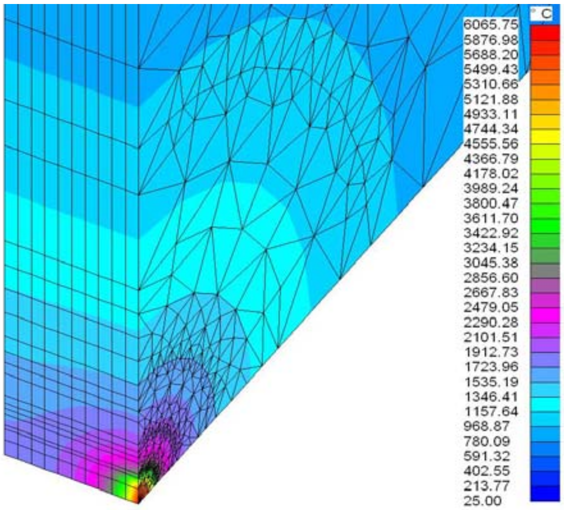

Fig. 5.21. Overall temperature distribution in the workpiece during laser microwelding process, based on the quarter-model computations using TAS, with Gaussian power distribution.

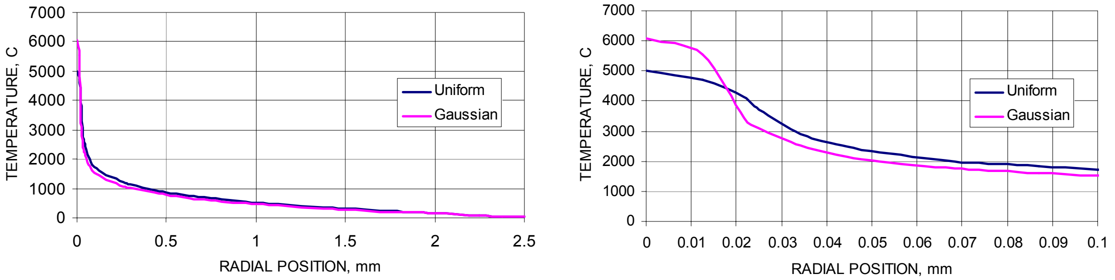

(a) (b)

Fig. 5.22. Temperature profiles in radial direction for laser microwelds, calculated for Gaussian and uniform power distributions, using TAS: (a) for 2.5 mm in radial direction, (b) for 0.1 mm in radial direction.

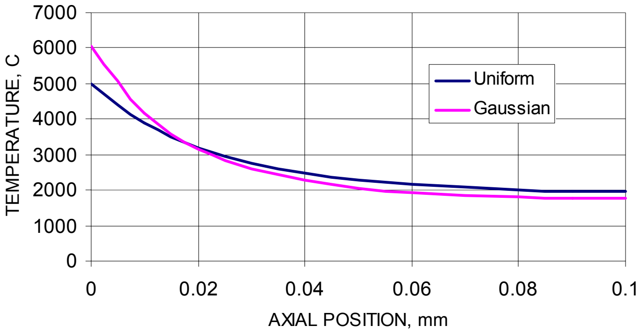

Fig. 5.23. Temperature profiles in axial direction for laser microwelds, calculated for Gaussian and uniform power distributions, using TAS.

Although stages of development of the FDM and TAS software used in this Dissertation are different, at this time, because FDM model includes latent heats of melting and vaporization but TAS does not, it is possible to compare results obtained at temperatures below the melting temperature of the material of a workpiece used. For example, using 0.1 mm thick copper workpiece subjected to a single laser pulse of 1 J with 4 ms pulse duration, FDM resulted in the maximum temperature of the workpiece of 864°C while TAS resulted in the maximum temperature of 872°C. This is only 6°C temperature difference between the results produced by the two methods and was considered acceptable. That is, both FDM and TAS produced similar results.

For stress/deformation calculations, based on the temperature calculation for the quarter-model, von Mises stress, strain, and deformation were calculated, as shown in Figs 5.24 and 5.25, for uniform and Gaussian power distributions, respectively.

As can be seen in Fig. 5.24, for uniform power distribution, the maximum von Mises stress was about 1.195×10^3 lbf/mm^2, which is about 770 kpsi, while the yield strength of copper is about 54 kpsi, indicating that the workpiece would undergo plastic

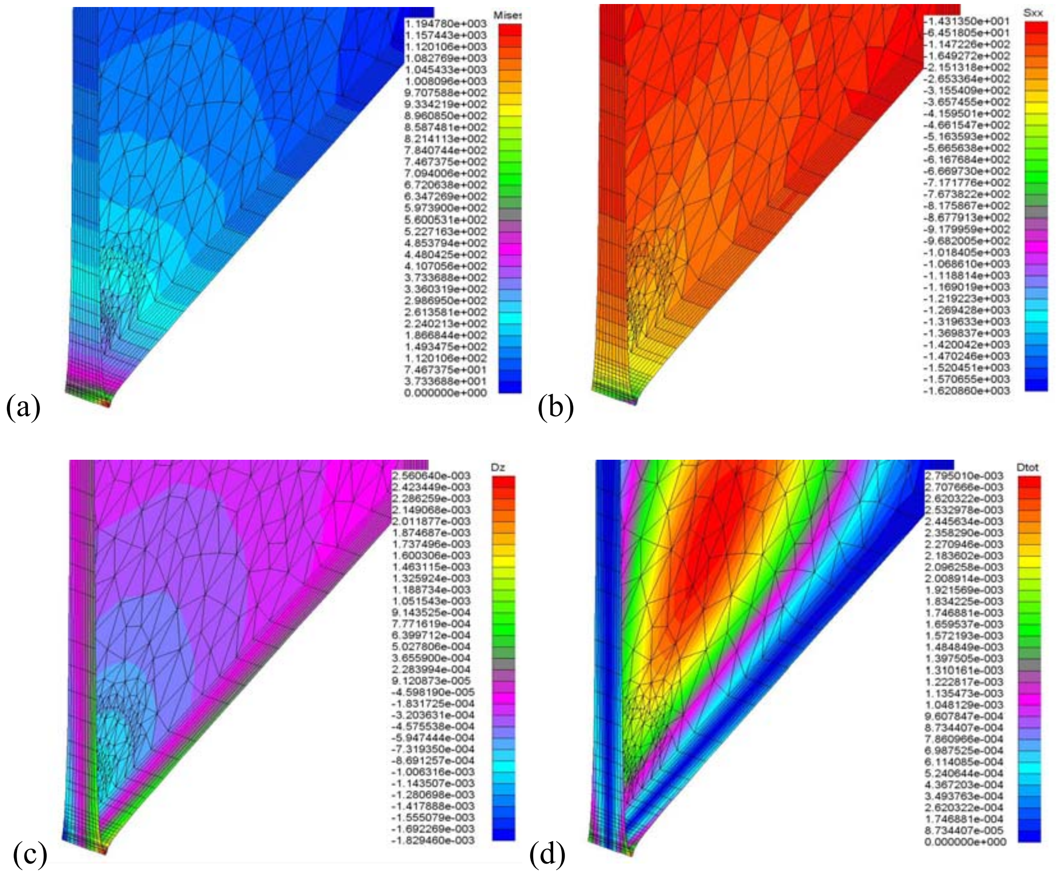

Fig. 5.24. Stress calculations for the quarter-model workpiece during laser microwelding process, for uniform power distribution, using TAS: (a) von Mises stress, (b) stress along the radial direction, (c) deformation along the direction of the laser beam, (d) total deformation.

deformations. Due to the increase of temperature in the workpiece and the clamped boundary conditions which assumed that no lateral expansion was allowed, the stresses along the lateral direction of the workpiece showed the compressive values, with the maximum compressive stress occurred at the spot under the laser beam, Fig. 5.24b. For the thermal deformations, the maximum deformation along the direction of the laser beam is about 2.56 μm, Fig. 5.24c. Furthermore, consider the assumed clamped boundary condition, which didn't allow lateral expansions, the overall thermal deformation of the workpiece has the maximum value of 2.795 μm, Fig. 5.24d.

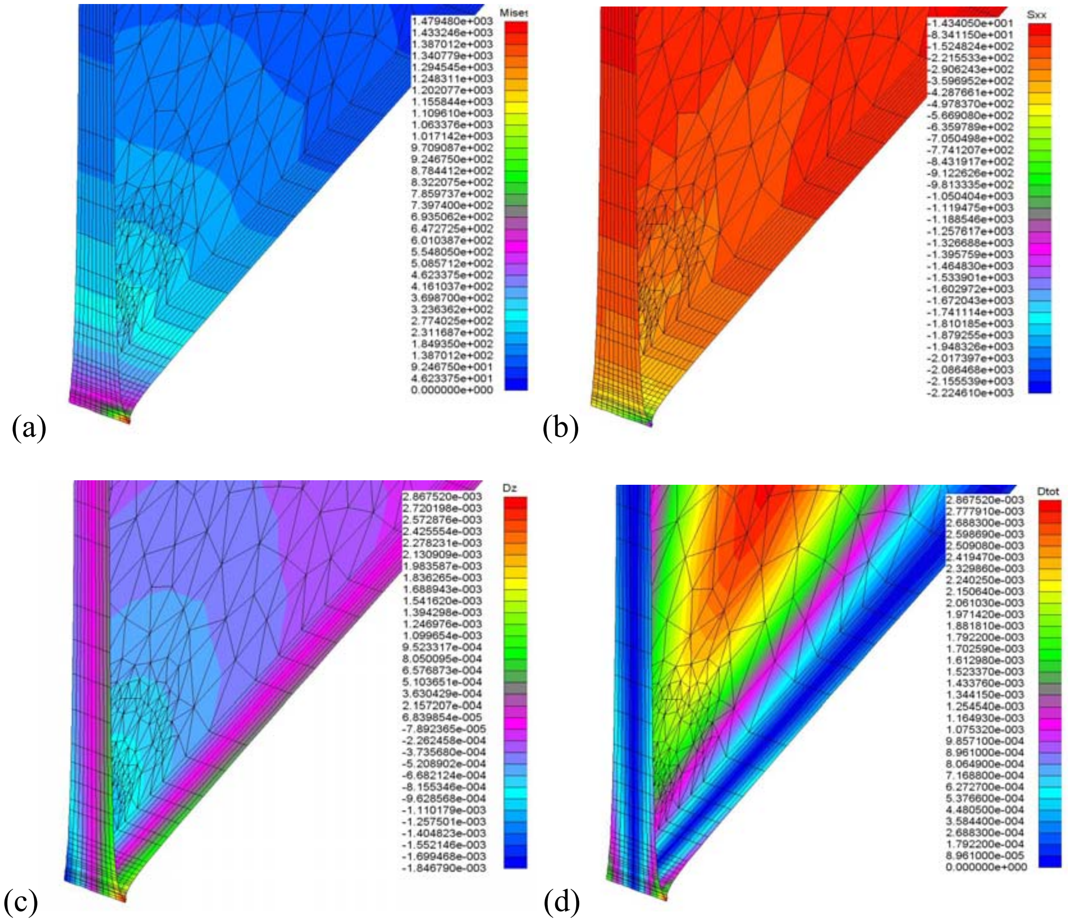

Fig. 5.25. Stress calculations for the quarter-model workpiece during laser microwelding process, for Gaussian power distribution, using TAS: (a) von Mises stress, (b) stress along the radial direction, (c) deformation along the direction of the laser beam, (d) total deformation.

TAS analysis of the thermal stress and deformation in the workpiece under Gaussian power distribution, Fig. 5.25, show a higher maximum stress value of 1.479×10^3 lbf/mm^2, which is about 954 kpsi, than the maximum stress level for the uniform power distribution. Also the maximum thermal deformation in the workpiece with Gaussian distribution was 2.887 μm, Fig. 5.25c, indicating a larger thermal deformation than the case with uniform power distribution. This is because the Gaussian power distribution produced a higher maximum temperature than the case with uniform power distribution, as shown in Fig. 5.17, therefore leads to a larger temperature gradient in the workpiece.

Furthermore, temperature distributions during laser two-part microwelding processes were calculated using TAS. The materials used for microwelding were copper (top layer) and various materials (bottom layer), i.e., aluminum, zinc, beryllium copper, and stainless steel. Thermal conductivities of the materials used in TAS models are listed in Table 2. Both layers have the dimensions of 2.5 mm by 2.5 mm by 0.1 mm, Fig. 5.26.

Table 2. Thermal conductivities of materials (at 20 °*C*)

	Cu	Al	Zn	BeCu	S. Steel
W/mm°K	0.389	0.237	0.115	0.083	0.016

The temperature fields on the microwelded workpiece are shown in Fig. 5.26, and the axial temperature profiles along the direction of the laser beam propagation for the different combinations are summarized in Fig. 5.27. As can be seen in Figs 5.26 and 5.27, at the interface between the top and bottom layers, the slope of the temperature curve changes due to the different thermal conductivities of the two different materials. As the thermal conductivities of aluminum, zinc, beryllium copper, and stainless steel

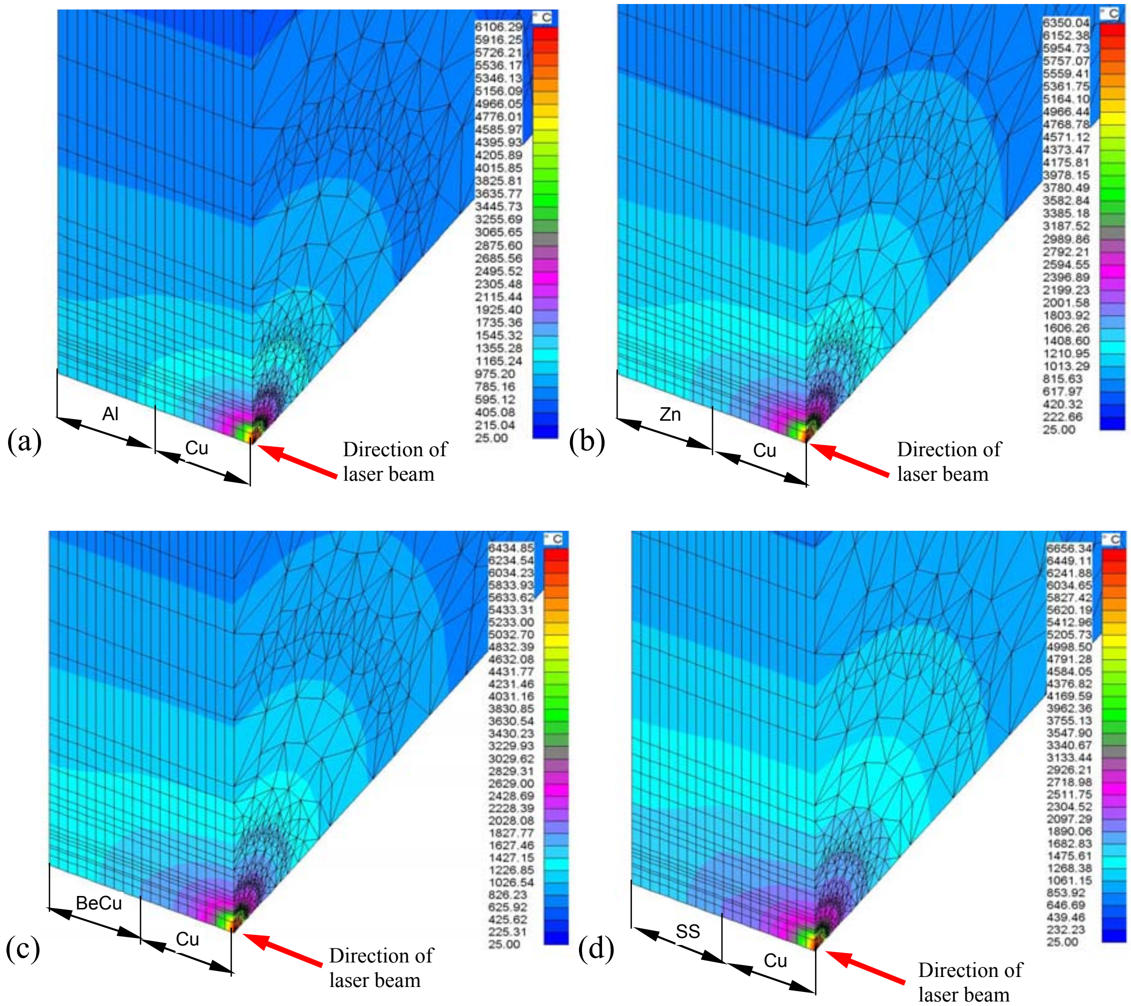

Fig. 5.26. 3D temperature profiles for the two-part laser microwelds, calculated using TAS: (a) copper and aluminum, (b) copper and zinc, (c) copper and beryllium copper, (d) copper and stainless steel.

decrease, Table 1, the changes of the slope of the temperature curve become more significant, and the overall maximum temperatures of the welded workpiece increase. Furthermore, based on the calculated temperature for two layers of material, stresses and deformations can be calculated, as shown in Figs. 5.28 for the representative results for welding copper with stainless steel.

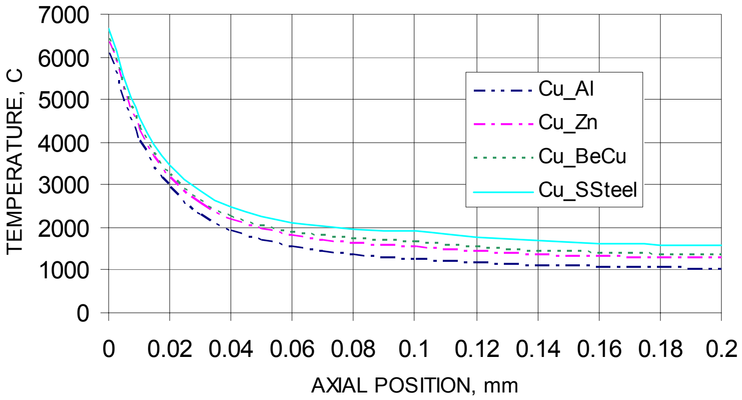

Fig. 5.27. Summary of temperature profiles for the two-part laser microwelds, calculated along the direction of the laser beam using TAS.

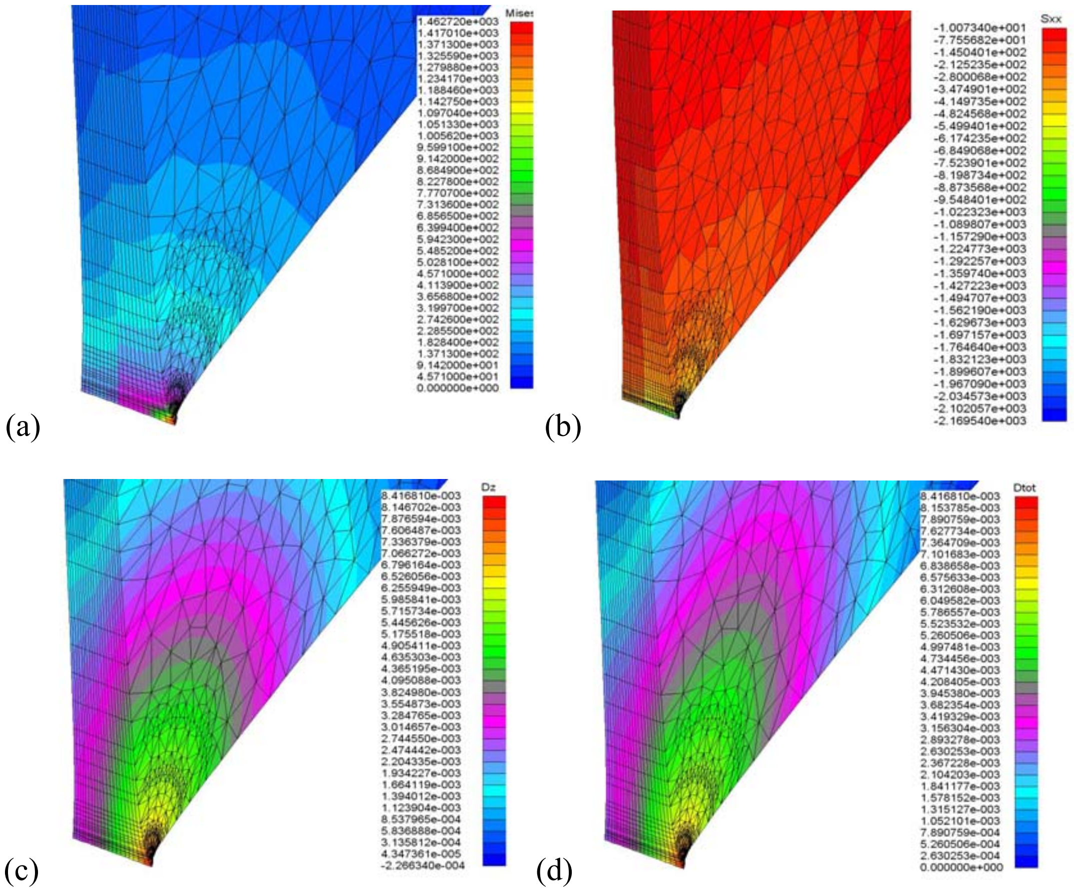

Fig. 5.28. Stress calculations for the quarter-model workpiece during laser microwelding process, for welding copper with stainless steel:
(a) von Mises stress, (b) stress along the radial direction, (c) deformation along the direction of the laser beam, (d) total deformation.

As can be seen in Figs 5.28 for laser welding of copper and stainless steel, the maximum thermal stress in the welded workpiece was about 1.463×10^3 lbf/mm^2, which is about 943 kpsi, while the yield strengths of copper and stainless steel are about 54 kpsi 75 kpsi, respectively. Therefore, the welded workpiece would undergo plastic deformations. In addition, the slope of the stress curves showed significant discontinuities at the interface between the copper and stainless steel layers, due to the significant difference in thermal conductivities of the two different materials, and this discontinuity may lead to undesired failure mode in the future. In addition, the maximum thermal deformation along the direction of the laser beam for welding copper and stainless steel was about 8.42 μm, shifted toward the source of the laser beam, as shown in Fig. 5.28c, and the layer with copper has the most contribution to the overall thermal deformation due to the much higher thermal conductivity of copper than that of stainless steel.

6. EXPERIMENTAL INVESTIGATIONS

The purpose of this chapter is to present and discuss some representative results of the experimental work on interaction of pulsed laser beam with metal workpiece, obtained during this Dissertation. First, characteristics of the laser system used in the experiments through the preparation of this Dissertation are presented in Section 6.1. Secondly, representative results of laser microdrilling on thin metal sheets are presented and discussed in Section 6.2 for the effect of laser parameters on the microdrilling results. Thirdly, laser microwelding experiments as the function of different laser parameters are presented and discussed in Section 6.3, with discussions of representative evaluation techniques that were used to characterize the laser microwelded workpiece. Finally, correlations between computational and experimental investigations for laser material processing are included in Section 6.4.

6.1. The Nd:YAG laser system

The type KLS 126 pulsed Nd:YAG laser system was used in the experimental study of this Dissertation (Lasag, 1997). Norminal performance characteristics of the laser system provided by the manufaturer include 130 J maximum pulse energy, 200 W maximum average output power, 0.1 to 10 ms pulse duration, and 1.06 μm wavelength. The typical laser spot diameter is about 80 μm.

With the Nd:YAG solid-state laser, the rod-shaped laser crystal is lit ("pumped") with visible light. The source of the pumping energy is a plasma flashlamp (electrical duscharge in a quartz tube filled with inert gas). The laser rod stores the pumping light energy for a short time in the form of pumped electron levels and then emits them once again in the infrared wavelength of 1064 nm (fluorescent effect).

The optical resonator, which consists essentially of the laser crystal and two papallel mirrors, enables multipe passages through the crystal, which lead to induced light emission and, therefore, to coheret (phase-constant) light. The laser radiation emerges through a partially reflecting outputting mirror.

The outstanding feature of the laser compared with other powerful sources of light is its ability to concentrate its beam energy onto a very small focal spot. This characteristic is due to minimum divergence, i.e., the minimum spreading out of the laser beam, which has in fact parallel wavefronts (Namba, 1998). Typical divergence values for lasers are 1 to 5 mrad (millimeters per meter).

The distribution of intensity in the laser beam is yet another quality feature. It must be optimized to suit the application. Usually, a so-called fundamental mode beam has the smallest possible divergence, while the multi-mode beams have several peaks of lower intensity (Chryssolouris, 1991).

The lens focuses the almost parallel laser beam onto the workpiece, Fig. 6.1. The following equation is used to evaluate approximately the spot diameter:

$$2\omega \approx \frac{2 \cdot f \cdot \theta}{M} \ , \tag{176}$$

where f is the focal length of the lens, θ is the divergence of the laser beam before the expander, and M is the expansion factor of the beam expander.

A reduced spot diameter (and, consequently, a high intensity at the place of machining) is, therefore, achieved with a focal length f as small as possible, a good beam quality (minimum divergence θ) and a high expansion factor M for the beam expander.

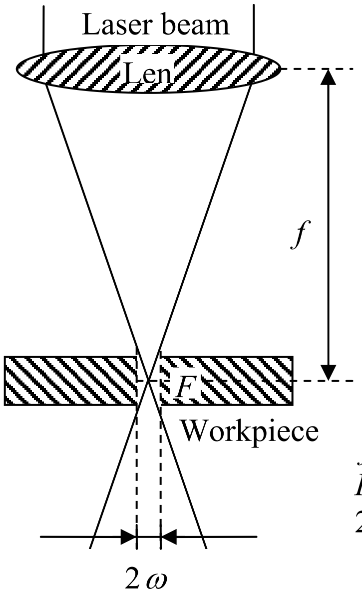

f: focal length of lens
F: focal point
2ω: Spot diameter at the focal point

Fig. 6.1. Beam focusing onto the workpiece.

Lenses with longer focal lengths have the advantage that, because of the greater distance, it is much easier to position the workpiece and protect the lens from material spatters. To achieve the best possible compromise for the application in question, lenses are used with focal lengths ranging from 100 to 300 mm. Conventional lens protection usually consists of easily replaceable glass covers.

6.2. Experimental investigations of laser microdrilling

A pulsed Nd:YAG laser emitting at 1.06 μm wavelength was used in the experiments. The variable parameters for the laser system include: peak power (1.5 to 4.0 kW), energy per pulse (1.75 to 4 J), pulse frequency (1 to 10 Hz), and pulse width (0.5 to 2 ms). The laser beam was focused with a lens of 100 mm focal length. The focal plane position was placed at the workpiece material surface giving a beam spot size of approximately 80 μm in diameter.

Laser microdrilling experiments were carried out with various laser parameters on flat stainless steel 304 sheets, which has the thickness of 30 mils. Typical axial shape and characteristic dimensions of the laser microdrilled holes are illustrated in Fig. 6.2, and the characteristic dimensions of the laser microdrilled holes were measured using the microscope. These dimensions show the entrance diameter on the top surface, *D_front*, where the laser impinges on the workpiece surface, the minimum hole diameter, *D_min*, i.e., minimum diameter within the through hole, which was measured using a light source on the back of the hole and measured for the minimum area that the light would go through, and exit diameter on the bottom surface, *D_back*. These dimensions give a general idea of what is the shape of the hole when looked in the direction of propagation of the laser beam (Han, 1999).

Several parameters, such as the laser peak power, laser pulse length, laser pulse frequency, number of pulses, and laser focal position, were adjusted to obtain different hole profiles. At each setting, ten microholes were drilled repetitively on the stainless steel 304 sheets, with 5 mm hole pitch so that the effect of one hole does not influence

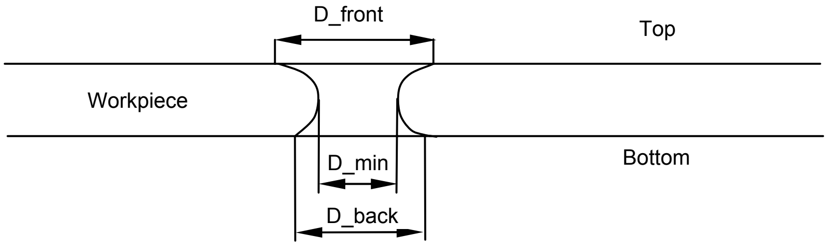

Fig. 6.2. Typical shape and characteristic dimensions of the laser microdrilled hole.

the microdrilling conditions of the next adjacent hole, and the final values were taken from the average hole dimensions.

6.2.1. SEM characterization of surface topography for microdrilling

Every laser microdrilled test sample was first taken to the SEM to study its surface topography. Figures 6.3a shows the representative SEM picture of a laser microdrilled hole, where the entrance and minimum hole diameters can be viewed as well as the materials ejected to the side of the entrance of the spot and therefore formed the crater during the material removal and ejection period. The workpiece was then cut, ground, and polished to view the cross sectional profile using an optical microscope. Figure 6.3b shows an optical image of the cross sectional view of a laser microdrilled hole in the flat sheet, where dimensions of the maximum hole diameter, minimum hole diameter, which indicates the penetration diameter within the workpiece, and exit diameter on the bottom surface, can be measured.

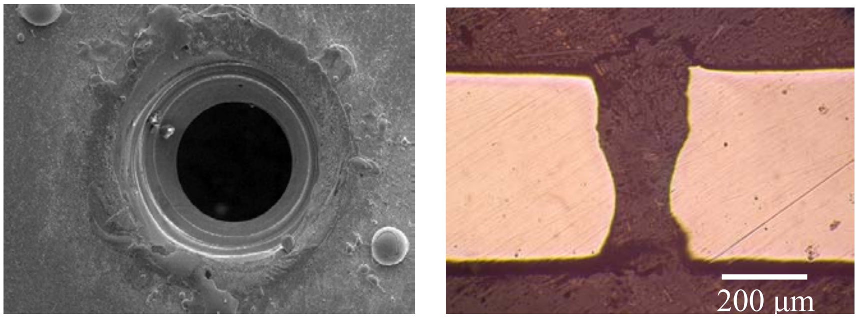

(a) (b)

Fig. 6.3. Characterization of a laser drilled microhole on stainless steel 304 sheet: (a) SEM image of the top, (b) optical image of the cross section.

6.2.2. Effect of laser power

The amount of laser power required for laser microdrilling process is determined by examining the optical and thermal properties of the workpiece material, as discussed in Section 4.4.2. When sufficient energy is applied on the surface of the workpiece so that its temperature is beyond boiling point, vaporization occurs and a recoil pressure is generated. The pressure ejects the melt from the interaction zone, and a cavity is formed as a result. In order to study the effect of laser peak power on the resultant dimensions of the hole, continuously increased laser peak power was applied from 1.75 kW to 4 kW, with a constant pulse width of 1 ms, and the laser beam focal plane position (*fpp*) was zero, i.e., the laser was focused on the surface of the workpiece, note that the zero *fpp* condition was determined experimentally using computer controlled micropositioner, with the uncertainty of ±0.08 mm. As shown in Fig. 6.4, the power at the beam breakthrough (i.e., the onset of a through hole) was 2.25 kW. For the hole entrance diameter *D_front*, as the laser peak power increased, *D_front* first increased significantly

(~20%) when power increased from 2.25 kW to 3.5 kW, then increased slightly (~2%) when power increased from 3.5 kW to 4 kW. For the hole minimum diameter *D_min* and exit diameter *D_back*, as the laser peak power increased, they first increased slightly (<5%) when power increased from 2.25 kW to 3.5 kW, then increased significantly (~20%) when power increased from 3.5 kW to 4 kW. It should be noted that for a single pulse condition, the exit diameter was always very close to the minimum hole diameter.

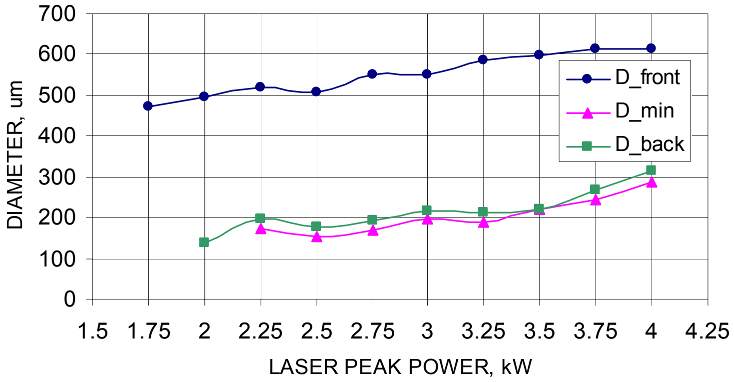

Fig. 6.4. Effect of laser power on the dimensions of laser drilled microholes in stainless steel 304 sheets, *f* = 5 Hz, *t* = 1 ms, *N* = 1, and *fpp* = 0.

The amount of laser power required is determined by examining the optical and thermal properties of the workpiece material. The thermal properties can be divided into two basic categories: fixed and loss properties. The first category determines the amount of energy required to melt and vaporize the material. This includes heat capacity, latent heat, and heat of vaporization. Loss properties are important because they determine the energy transmitted to the surrounding material during processing. Thermal diffusivity is most important in transient operations, while thermal conductivity is more important in steady-state applications.

Optical properties of the laser affect the surface of the workpiece where the laser beam impinges. Of the optical material properties, the absorptivity of the material has the largest influence on laser power requirements. The material absorptivity determines the fraction of the impinging radiation energy that is actually absorbed by the material. The remainder of the beam energy is reflected back into the environment. Thus, laser power must be adjusted so that the required amount of power for achieving the desired material removal at the desired processing rate is absorbed by the surface, instead of only impinging on the surface. The absorptivity value can vary depending on the wavelength of the beam impinging on the surface, surface roughness, temperature, phase of the material, and the use of surface coatings. The process rate also is related to the required laser power, however, this relationship is complex, since the process rate will also affect the energy losses of the process and the power will affect the material/laser coupling. Estimation of power requirements can be performed by using model of the specific laser machining process to relate the material properties, operating parameters such as laser power and process rate, and material removal characteristics such as depth of cut, hole dept, and the shape of the cut.

As can be seen from the experimental results in Fig. 6.4, for single shot cases, an increase in laser peak power has less effect on the entrance hole diameter than the minimum and exit diameters. This is because of the balance between the recoil pressure and the surface tension which creates the material ejection.

6.2.3. Effect of laser pulse length

Holding a fixed laser peak power (3.5 kW), through microholes were drilled to study the effects of pulse width on the dimensions of the holes. Increasing the pulse width at a fixed peak power effectively increases the energy per pulse of the laser. Therefore, using a longer pulse width effectively causes longer duration of vapor pressure (recoil pressure) build up inside the hole and thereby generating more material ejection. However, at long pulse width, when $t = 1.75$ ms, there was no through hole drilled, as shown in Fig. 6.5. A possibility for this phenomenon could be the presence of laser-supported absorption (LSA) wave due to exceeding long pulse width. LAS wave can cause blockage of laser energy from the material surface as an absorbing plasma is generated at or near the surface and propagates up the laser beam. In general, the optimum pulse width for material removal is dependent on the target material. If the pulse width exceeds the optimum value for the particular material, laser energy is wasted in the LSA wave. Therefore, if the presence of LSA wave occurred during the experiments, the material removal process would be prematurely shielded and thus reducing the amount of material being removed per pulse. Also, due to the upward propagation of the LSA wave towards the laser beam, the angle of material ejection could be altered and more likely to one of vertical. These phenomena could then contribute to less material removal at long pulse width ($t > 1.5$ ms for this workpiece).

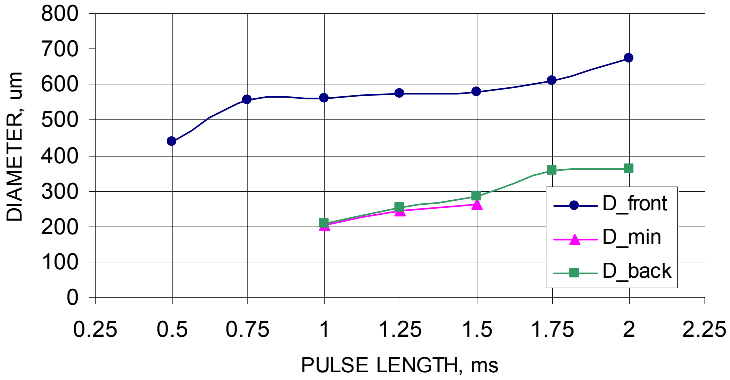

Fig. 6.5. Effect of laser pulse length on the dimensions of laser drilled microholes in stainless steel 304 sheets, *f* = 5 Hz, *P* = 3 kW, *N* = 1, and *fpp* = 0.

6.2.4. Effect of number of pulses

Laser percussion drilling is the process where the workpiece is subjected to a series of laser pulses at the same spot at a specific setting, which results in melt ejection and consequently forming a hole.

Due to the nonlinear nature of laser/material interaction, the ejection of matter is an unstable process, with the ejection rate and mechanism subject to a variety of instabilities. These instabilities include fluctuations in the position and shape of the keyhole, fluctuations in laser output, and interruption of the beam by attenuation and scattering in the plasma plume.

In laser drilling, the temperature of the solid workpiece rises to become molten state, leading to vaporization. This vapor generates a recoil pressure on the workpiece surface with a force much greater than the surface tension of the melt. At the same time, there exists a pressure gradient in the radial direction of the beam due to the decreasing laser intensity, such that the liquid melt would move in the direction of decreasing pressure. Together, the pressure forces the liquid at the bottom of the forming crater to displace in the radial direction, which is then driven along the wall of the crater and is expelled from the entrance of the drilled hole.

Investigations of the effect of total laser energy/number of pulses are performed at various laser peak power levels, Fig. 6.6, and the diameters of the entrance, exit, and minimum of the holes were recorded starting at the beam breakthrough (i.e., the onset of a through hole). Before the beam breakthrough, there was consistent ejection of material to the side of the entrance of the spot, which indicates that not enough recoil pressure is obtained so that to overcome the surface tension on the melt to create a through hole. After beam breakthrough, most of the material ejection due to each laser pulse is predominantly ejected downwards through the exit end of the hole, in which some of the materials tend to cling on the rim of the exit hole forming dross. After the first pulse of the beam breakthrough level, there indicates significant uncertainty of the circularity of the through hole, as shown in Fig. 6.7a and Fig. 6.8a, where in Fig. 6.7 a back light source was used to view the minimum area that the light could go through, and in Fig. 6.8 the SEM was used to view the profiles of the holes from the top view. In addition, the exit diameter of the hole at beam breakthrough was found very close to the minimum diameter of the hole, and the ratios between *D_front* and *D_back* are very large, with respect to the subsequent through holes in its range (Han et al., 2004).

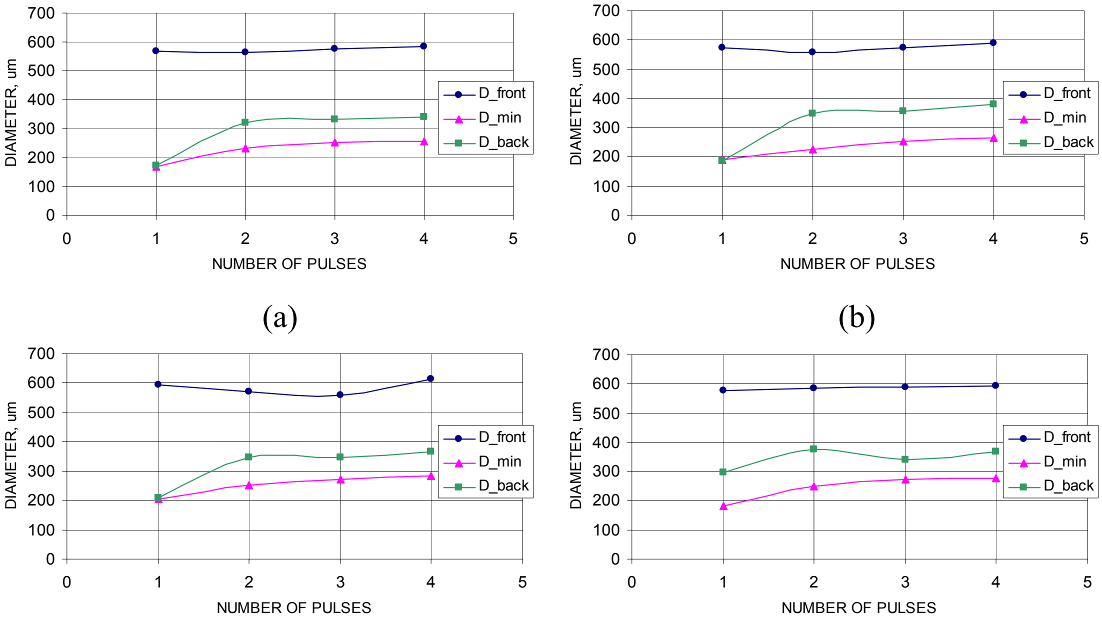

(a) (b)

(c) (d)

Fig. 6.6. Effect of number of pulse on the size of laser drilled microholes in stainless steel 304 sheets for different laser peak power levels, $f = 5$ Hz, $t = 1$ ms, $fpp = 0$: (a) $P = 2.75$ kW, (b) $P = 3$ kW, (c) $P = 3.25$ kW, (d) $P = 3.5$ kW.

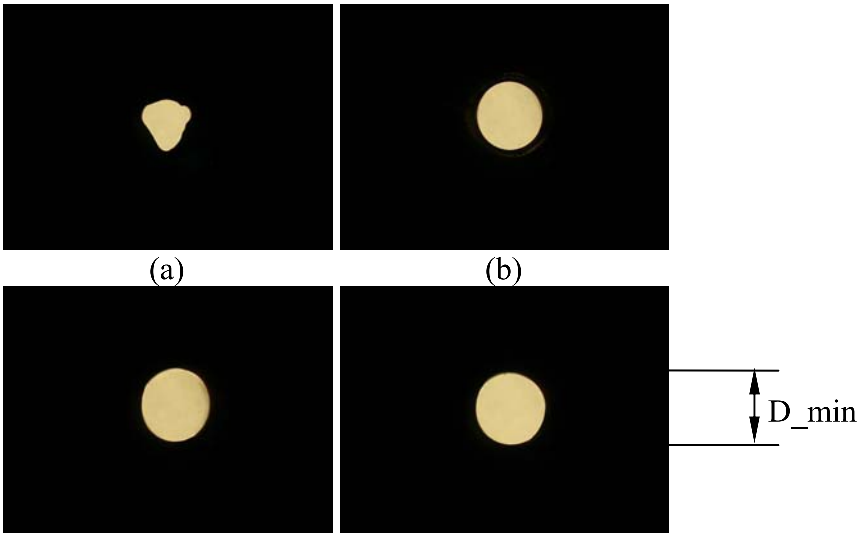

(a) (b)

(c) (d)

Fig. 6.7. Effect of number of pulse on the circularity of laser drilled microholes in stainless steel 304 sheets, $f = 5$ Hz, $t = 1$ ms, $E = 3.5$ J, $fpp = 0$: (a) $N = 1$, (b) $N = 2$, (c) $N = 3$, (d) $N = 4$.

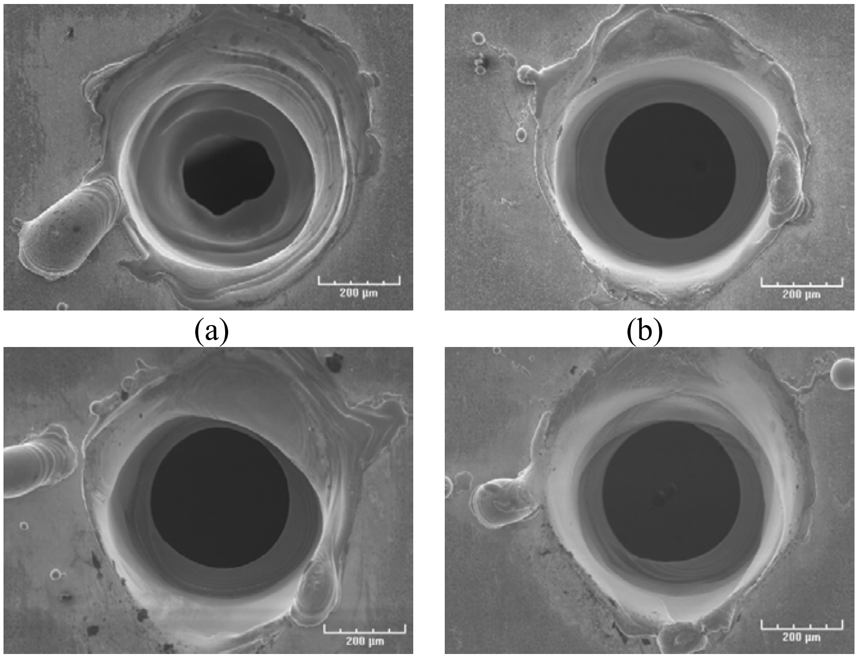

(a) (b)

(c) (d)

Fig. 6.8. SEM pictures of laser drilled microholes in stainless steel 304 sheets for different number of pulse, *f* = 5 Hz, *t* = 1 ms, *E* = 3.5 J, *fpp* = 0: (a) *N* = 1, (b) *N* = 2, (c) *N* = 3, (d) *N* = 4.

In order to further investigate the effect of multiple pulses on laser microdrilling process, the workpieces were hot-mounted, ground, and finely polished to view the cross sectional profiles, as shown in Fig. 6.9. After the first pulse, the minimum hole diameter is about located at the bottom of the hole, which indicates the same dimensions for the minimum and exit hole diameters, Fig. 6.9a. With the subsequent pulses, the sharp edge at the bottom of the hole was removed and moving the minimum hole diameter further up. At the same time, as the number of pulses increased, the resolidified material adhered to the periphery of the entrance was removed, therefore there shows a more even side wall profile.

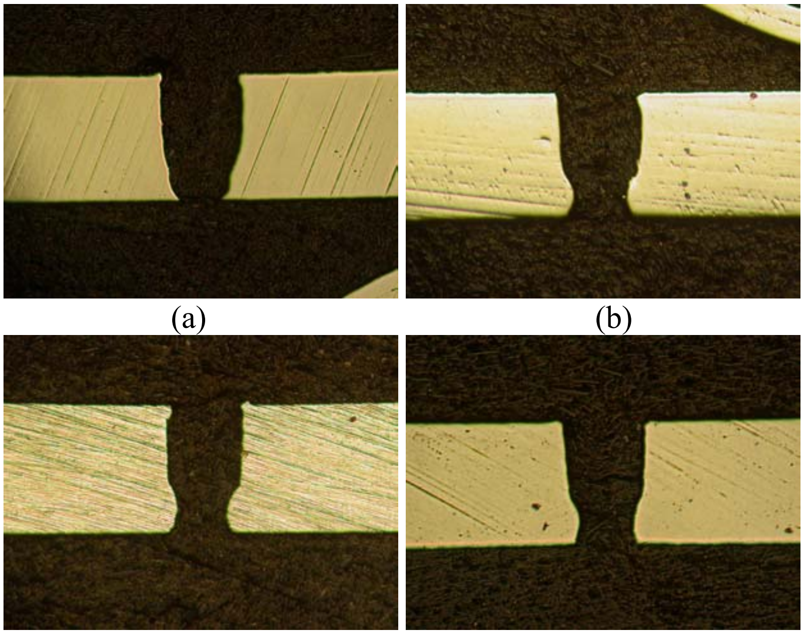
(a) (b)
(c) (d)

Fig. 6.9. Cross sectional pictures of laser drilled microholes in stainless steel 304 sheets for different number of pulse, $f = 5$ Hz, $t = 1$ ms, $E = 3.5$ J, $fpp = 0$: (a) $N = 1$, (b) $N = 2$, (c) $N = 3$, (d) $N = 4$.

6.2.5. Effect of laser pulse frequency

Laser percussion drilling involves the superposition of a series of pulses over the same focal area. During each laser pulse, erosion takes place in the interaction time between the liquid melt and the parent material. The liquid material that is not completely expelled during the removal process remains attached to the sidewall of the hole, and re-solidification occurs between each pulse, and the extend of resolidification strongly depends on the pulse frequency. When higher pulse frequency was used, less melted material is resolidified, and more of the melt pool is pushed over the rim of the entrance hole in the direction of the laser beam, which results in the more significant effect of material removal in the direction of the laser beam. Therefore, straighter sidewall profile is usually obtained with higher pulse frequency. However, when the laser pulse frequency is too high (approximately equal to the reciprocal of the time constant of the material), the reduce of the pulse gap could cause an interaction between the successive laser pulses and the ongoing ejecting material, therefore the material removal can be less significant and the straightness of the sidewall of the laser drilled holes can get worse. Figure 6.10 shows the results of varying the pulse frequency at a fixed laser power of 3 kW, and the number of pulses ranged from $N = 2$ to $N = 4$. At the lower laser pulse frequencies, the materials were ejected freely without interaction with successive laser pulses, and D_min reached the maximum value at 5 Hz, while D_front and D_back were at the relatively smaller value, indicating that the best straightness of the sidewall of the holes was obtained. For higher laser pulse frequencies, i.e., $f > 5$ Hz, D_min showed the decreasing values while D_front and D_back increased slightly, the possible explanation is that higher frequencies caused pulse gap shorter than the time required for free material ejection (Han, 2004). Detailed investigations including the characterization of the dimensions and paths of the ejected melt particles for the specific workpiece material can be performed in order to fully understand the effect of the laser pulse frequency on the dimensions of the resultant laser drilled microholes.

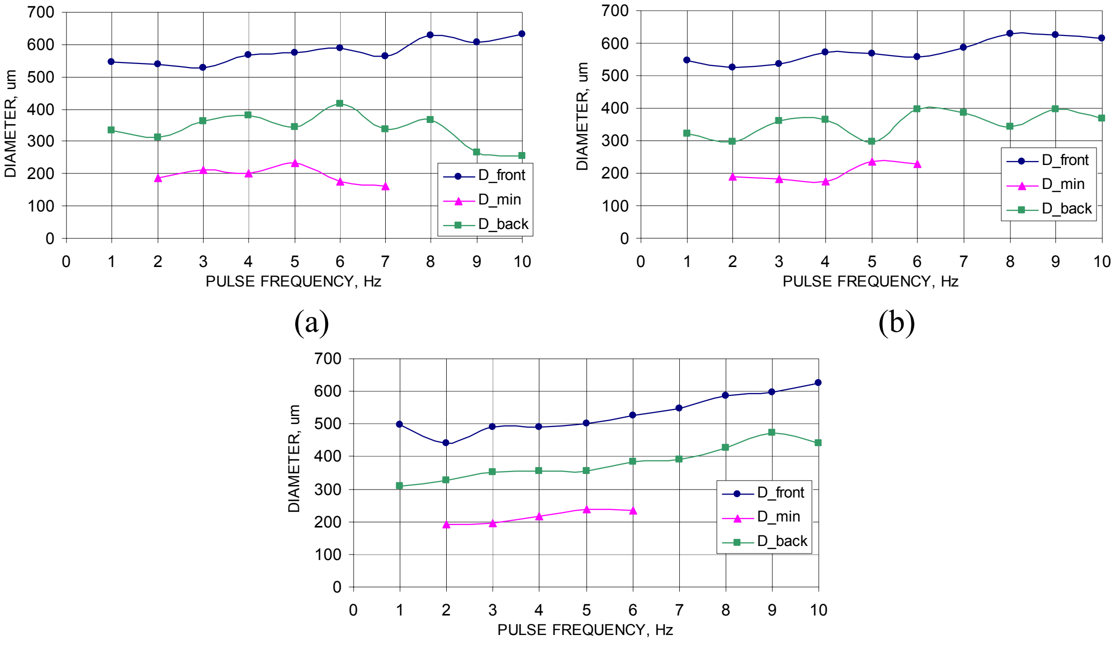

(a) (b)

(c)

Fig. 6.10. Effect of laser pulse frequency on the size of laser drilled microholes, $t = 1$ ms, $E = 3$ J, and $fpp = 0$: (a) $N = 2$, (b) $N = 3$, (c) $N = 4$.

6.2.6. Effect of laser focal position

The holes produced by laser microdrilling are not of the same quality as other processes (e.g., EDM, ECM). Since the laser microdrilling operation is a thermal process, formation of a recast layer on the surface of the hole is to be expected.

In laser processing, intensity (power per unit area) of the laser beam at the material surface is of prime importance. Intensity great enough to melt or vaporize any material can be generated by focusing a laser beam. The maximum irradiance is obtained at the focal point of a lens, where the beam is at its smallest diameter. The location of this minimum diameter is called the focal spot. Intensity values of billion of Watts per square centimeter can be obtained at the focal spot. The imperfections of the optical components and diffraction effects limit the size of the obtainable focal spots.

Several factors influence focal spot size. First, focal spot size is directly related to the quality of the incoming beam, which can be quantified by the divergence of the beam. A laser beam with a small divergence can be focused to a smaller spot than a beam with high divergence. Second, focal spot size is influenced by diffraction. When focusing a diffraction-limited laser beam with a lens, a longer focal length or higher *f*-number corrsponds to a larger focused spot diameter. Finally, the diameter of the incoming laser beam affects the focal spot size. When restricted to specific optics, the only method of producing smaller focal spot sizes is to increase the incoming laser beam diameter (Nowak and Pryputniewicz, 1992). The effects of focus is shown in Fig. 6.11, note that (d) is the best focal condition for drilling (Ruselowski, 1987).

In general, the focal plane position (*fpp*) of the laser beam has a significant effect on the resultant hole geometry. The *fpp* was considered zero when it was set on the workpiece surface, and above or below the surface was considered positive and negative *fpp*, respectively. In the experiments, the workpiece of stainless steel 304 sheet with the thickness of 30 mils was used, the *fpp* was varied between +1.0 mm (above the workpiece surface) and -3.0 mm (below the workpiece surface) with the constant laser power of 3.5 kW and pulse frequency of 5 Hz, and the characteristic dimensions of laser drilled microholes were measured for the diameters of the front, minimum, and back, as summarized in Fig. 6.12. Note that the zero *fpp* condition was determined experimentally using computer controlled micropositioner, with the uncertainty of ±0.08 mm.

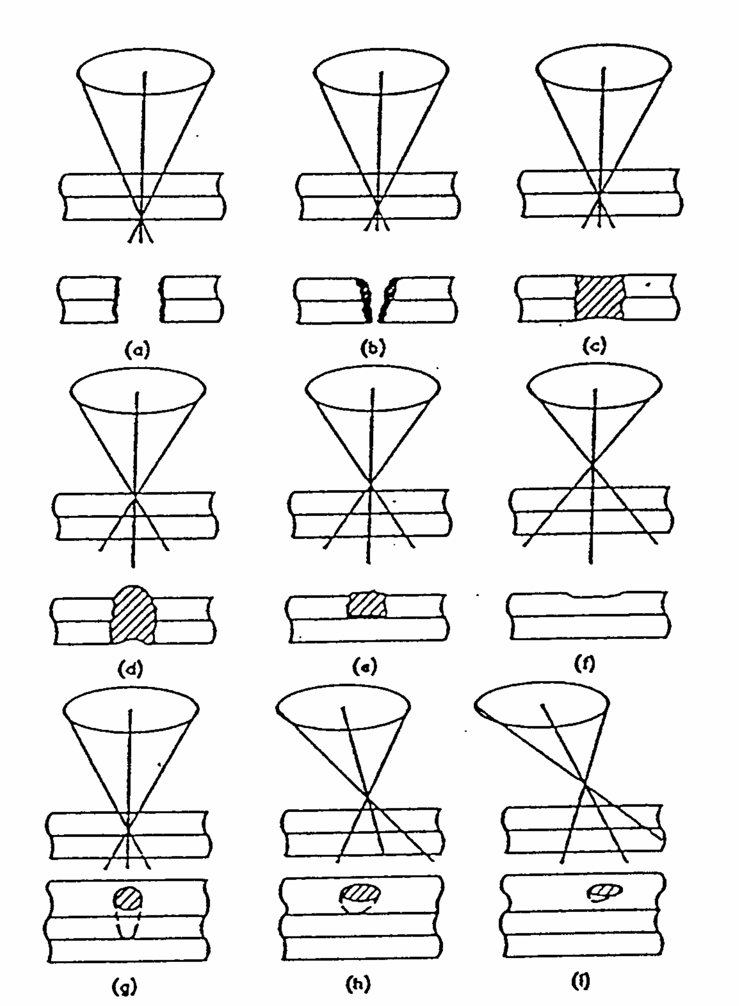

Fig. 6.11. The effect of laser focal position and direction of beam propagation.

As can be seen in Fig. 6.12, maximum *D_min* can be obtained at zero *fpp* for various number of laser pulses, due to the maximum power intensity at the laser focal position. For single pulse conditions, no through holes were produced with the positive *fpp* conditions (laser beam was focused above the workpiece surface), indicating that not enough power density was provided to the workpiece for the multiple phase

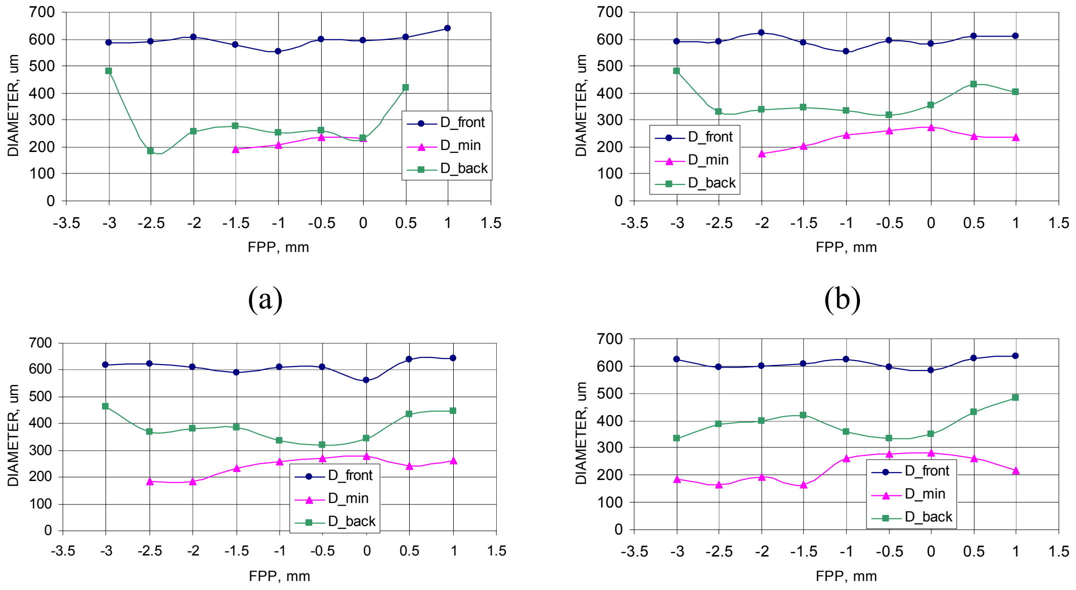

(a) (b)

(c) (d)

Fig. 6.12. Effect of laser *fpp* on the size of laser microdrilled holes on stainless steel 304 sheets for different laser pulse numbers, $f = 5$ Hz, $t = 1$ ms, $E = 3.5$ J: (a) $N = 1$, (b) $N = 2$, (c) $N = 3$, (d) $N = 4$.

transformations as well as material rejection that were required for drilling. When the laser was focused above the workpiece top surface, as the laser beam propagates from its focal position to the workpiece top surface, the laser power intensity decreased as the spot diameter increased, also large amount of energy was lost in the medium, particularly because of the high reflectivity of metals. For the zero and negative *fpp* (laser beam was focused below the workpiece top surface), through holes were produced until *fpp* = -1.5 mm, and *D_min* decreased while *D_back* increased as the laser was defocused more. For laser microdrilling on stainless steel sheets with multiple pulses, as the number of pulses increased, more through holes could be produced as the laser beam was defocused more, however only restricted to the range from *fpp* = +1.0 mm until *fpp* = -3.0 mm, for the specific workpiece material and the laser system used in this Dissertation. Therefore, it can be suggested that, for laser microdrilling on metal sheets, the optimum laser focal position should be on the top surface of the workpiece, and the selection of the optimum range for the focus setting should include the considerations of the workpiece material properties, thickness, coupling effect of the focus setting, and power intensity distribution on the workpiece surface.

6.3. Experimental investigations of laser microwelding

Laser microwelding experiments were carried out with various laser parameters on welding copper sheets with various other materials such as beryllium copper sheets, and all of the workpiece had the thickness of 0.1 mm. Typical axial shape and characteristic dimensions of the laser microwelded samples are similar as illustrated in Fig. 6.2, including the welded diameter on the top surface, *D_front*, where the laser impinges on the workpiece surface, the minimum weld diameter, *D_min*, which was measured by sectioning the welded samples, and weld diameter on the bottom surface, *D_back*, and these characteristic dimensions were measured using the microscope. These dimensions give a general idea of what is the shape of the microweld when looked in the direction of propagation of the laser beam.

6.3.1. Laser microwelding experiments on thin metal sheets

The pulsed Nd:YAG laser emitting at 1.06 μm wavelength was used in the microwelding experiments to produce welds of micrometer size. The laser beam was focused with a lens of 100 mm focal length, and provided a beam spot size of approximately 80 μm in diameter.

Several parameters, such as the laser peak power, laser pulse length, and laser focal position, were adjusted for obtaining different microwelding profiles. At each setting, ten microwelds were made repetitively on the metal sheets, with 8 mm weld pitch so that the effect of one weld does not influence the welding conditions of the next adjacent weld, and the final values were taken from the average weld dimensions. The major investigation is to obtain the size of the microwelds as well as the porosity and grain size of the fusion zone, as they all might affect the strength, function, and lifetime of the microwelded parts.

6.3.1.1. SEM characterization of surface topography

Every laser micromachined test sample was first taken to the SEM to study its surface topography. Figure 6.13a shows the representative SEM picture of a laser microweld, where thermal cracking at the center of the microweld can be viewed. The cracking was caused by thermal stress developed during the process. In laser microwelding, solidification starts at the end of the laser pulse in the transition area between solid and molten metal and ends in the center of the microweld, which produces tensile stresses as a result of the inevitable shrinkage of the metal comprising the microweld (Han and Pryputniewicz, 2001). The sample was then cut and polished to view the cross sectional profile of the micromachined spot using an optical microscope. Figure 6.13b shows an optical image of the cross section of a laser microweld after etching, where there shows clear microstructure of the HAZ and significant discontinuity of the profile at the interface between the two materials.

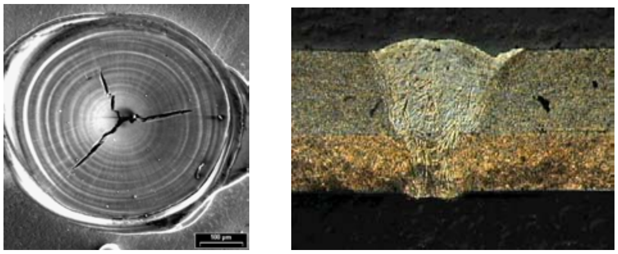

(a) (b)

Fig. 6.13. Characterization of a laser microweld: (a) SEM image of the top, (b) optical image of the cross section.

6.3.1.2. Effect of laser power

Laser microwelding is a fusion welding process, where materials are joined by melting the interface between them and allowing it to solidify. Unsuccessful results can be obtained if the melt pool is too large or too small or if significant vaporization occurs while it is present. Therefore, the control of laser power level as well as the pulse length is very critical as they might significantly affect the features of the microwelded spots.

For laser microwelding experiments, effect of laser power on the dimensions of the microwelded workpiece was studied for welding two copper sheets with the same thickness of 0.1 mm, as shown in Fig. 6.14. At a low laser power level ($P < 1.25$ kW), no complete weld penetration was achieved because no enough energy was provided to melt the two layers of material, and at these low power levels, the melted zone of the top surface was small. When enough power ($P >= 1.25$ kW) was provided, the two layers of materials both experienced melting, therefore the melted zone at the top surface (*D_front*) increased drastically. In addition, as the laser power continued to increase, the melted zone at the top surface (*D_front*) increased slightly while the melted zone at the bottom surface increased significantly, indicates that the top layer material has reached the energy equilibrium, and the extra power was absorbed by the bottom layer material continuously therefore the melted zone was increased more.

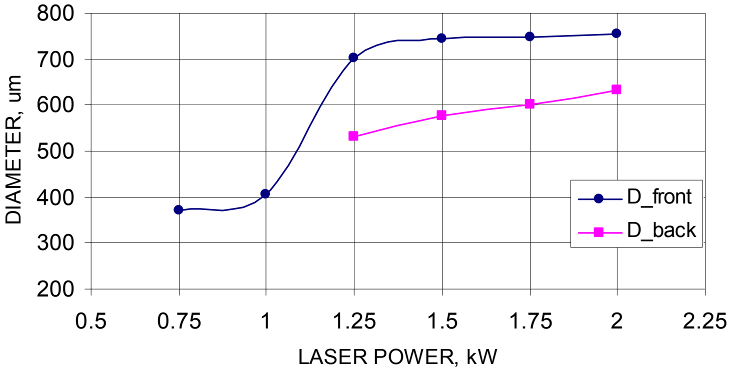

Fig. 6.14. Effect of laser power on the dimensions of laser microwelded workpiece, $f = 1$ Hz, $t = 4$ ms, $N = 1$, and $fpp = 0$.

6.3.1.3. Effect of laser pulse length

Increasing the pulse width at a fixed peak power results in the increase of the energy per pulse of the laser, therefore effectively causes longer interaction time between the laser beam and the workpiece, and creates larger melted zone, as shown in Fig. 6.15, when a constant power of 1.25 kW was used.

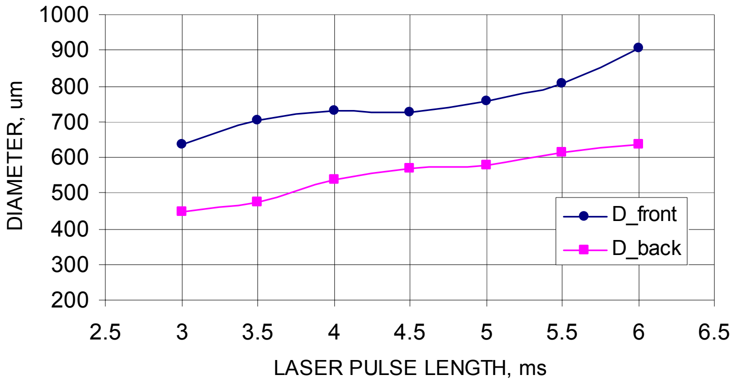

Fig. 6.15. Effect of laser pulse length on the dimensions of laser microwelded workpiece, *f* = 1 Hz, *P* = 1.25 kW, *N* = 1, and *fpp* = 0.

6.3.1.4. Effect of laser focal position

For laser microwelding experiments, effect of laser focal position under the constant power and pulse length on the dimensions of the welded workpiece was studied, as shown in Fig. 6.16.

For a positive *fpp* (laser beam was focused above the workpiece surface), there was no melted zone on the bottom surface, indicates that not enough power density was provided in order to let the both layer reaching melting state. The reason for the lack of

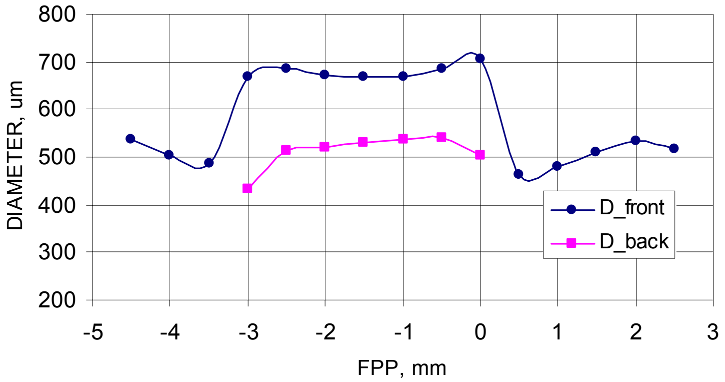

Fig. 6.16. Effect of laser focal position on the dimensions of laser microwelded workpiece, *f* = 1 Hz, *t* = 4 ms, *E* = 5 J, and *N* = 1.

melting zone on the bottom surface was that, when the laser was focused above the workpiece top surface, as the laser beam propagates from its focal position to the workpiece top surface, large amount of energy was lost, particularly since the reflectivity of polished copper is very high, and laser welding requires the power level between heating and drilling conditions, which is very critical and difficult to control. For the zero and negative *fpp* (laser beam was focused below the workpiece top surface), fusion zones were obtained continuously until *fpp* = -3 mm, and at zero *fpp*, the melted zone on top surface increased significantly, then decreased slightly as the *fpp* was placed more below the top surface. For the melted zone at the bottom surface, it increased slightly from *fpp* = 0 to *fpp* = -0.5 mm, then decreased slightly as it was defocused more. Furthermore, *D_front* and *D_back* remained almost constant for the range of *fpp* from -1.0 mm till -2.0 mm, which relates to the depth of focus of the laser beam and the resultant almost constant power density. In practical applications, the major parameters to consider would be the depth of focus and the minimum laser spot size, and some empirical data indicated that, for laser welding, it was suggest to place the laser focal position 1/3 of the thickness within the workpiece, as they may result in good weld size and qualities (Steen, 1998).

6.3.2. Evaluations of laser microwelding experiments

Quality of the laser microwelding depends on a number of parameters such as the characteristics of the laser beam, environmental conditions, and properties of the workpiece, and the performance of the laser microwelded structures is of special importance. Because of the large temperature gradients occur during fast laser microwelding process, a high stress level might occur and result in many undesirable phenomena such as the high level of residual stresses in the vicinity of the heat-affected zone (HAZ) that adversely affect the life time of the component. In addition, due to the modification of microstructure of the materials inside the HAZ during phase changes, the strength of the laser welded spots might vary significantly from the base material. Therefore, the evaluation of thermal deformation and change of strength of the laser microwelded spots are very important.

Numerous studies have been performed on the evaluation and prediction of the thermal stresses in laser microwelding process. However, it is very difficult to measure the thermal stresses, and to predict the magnitude and direction of thermal stress/deformation. Therefore, we develop an optical methodology, based on optoelectronic holography (OEH) technique, to measure and evaluate the thermal stresses/deformations non-destructively. In addition, tensile tests were performed on laser microwelded workpiece for different number of welds and different patterns, as they can be helpful of determine the quality of the laser microwelded workpiece.

6.3.2.1. Evaluation of thermal deformations for laser material processing

Many fabrication operations including laser micromachining cause certain thermal deformations. In this study, a unique methodology for measuring thermal deformations of the laser microwelds based on optoelectronic holography (OEH) methodology, which provides quantitative real-time whole field of view imaging, and allows measurements of displacements and deformations with sub-micrometer accuracy was used (Brown, 1999; Pryputniewicz et al., 2001).

6.3.2.1.1. Theory of OEH measurements

In the OEH configuration shown in Fig. 6.17, light going through an interference filter was used to provide continuous single-wavelength illumination for the measurement. The OEH process involves formation and acquisition of phase stepped interference images (Pryputniewicz and Furlong, 2000), and processing of these images to obtain the displacements and deformations of objects that are investigated.

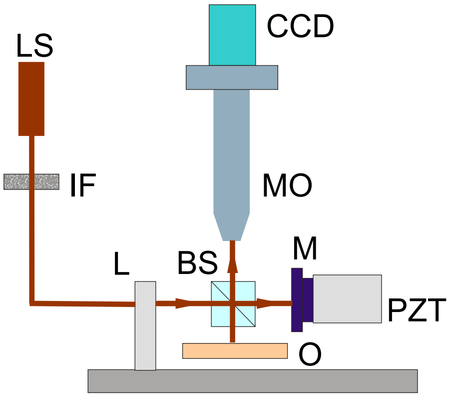

Fig. 6.17. Optical configuration of the OEH setup.

In the OEH system shown in Fig. 6.17, the beam from the light source (LS) is directed into an interference filter (IF), and the output of the single-wavelength beam is collimated by the lens system (L). The resulting light field is then divided into reference and illumination components by the beam splitter (BS). The reference leg is directed towards a PZT actuated phase step mirror (M) and back to the beam splitter. The illumination leg is directed towards the laser microweld under study (O) and is reflected back to the beam splitter (Han and Pryputniewicz, 2003a).

Therefore, from the observation point, two intensity distributions, transmitted by the long working distance microscope (MO), are viewed: one of light reflected from the object, and the other arising from reflection off the reference mirror. These two beams recombine and interfere with one another. The resulting interference intensity patterns are acquired by the camera (CCD), and the interference fringe patterns are processed by computer to produce deformation.

The images acquired by the CCD can be expressed as

$$I_i(x,y) = 2I_0(x,y)\{1+\cos[\phi(x,y)+\theta_i]\} \quad ,$$
$$i = 1,2,\ldots,5 \quad , \qquad \theta_i = \frac{(i-1)\pi}{2} \quad , \tag{177}$$

where $I_i(x,y)$ is the light intensity at each pixel of the i^{th} image, $I_0(x,y)$ is the average light intensity, $\phi(x,y)$ is the unknown phase, and θ_i is the known phase step introduced between successive interferograms in a given recording sequence (Pryputniewicz, 1999).

According to Eq. 177, the recording sequence consists of 5 interferograms between which phase steps of π/2 radians are introduced. These phase steps are applied in the reference beam with the mirror M, between acquisition of sequential images. The images in a given sequence record the same state of the laser microweld being studied, the only parameter that varies is θ_i, which changes in a stepwise fashion.

In order to determine deformations from the sequence of images described by Eq. 177, the optical phase is computed as (Furlong et al., 2002)

$$\phi(x,y) = \arctan\left\{\frac{2[I_4(x,y)-I_2(x,y)]}{2I_3(x,y)-I_1(x,y)-I_5(x,y)}\right\} \quad . \tag{178}$$

Equation 178 yields spatial distribution of wrapped phase. This wrapped phase map is then unwrapped to produce a continuous phase map at each point on the studied laser weld (Bushman et al., 1993). The continuous phase can, in turn, be used to determine the spatial distribution of differences in the optical path, *OP*(*x,y*), traversed by the object and reference beams, i.e.,

$$OP(x,y) = \frac{\lambda}{2\pi}\phi(x,y) \quad , \tag{179}$$

where λ is the wavelength of the illumination light used in the specific OEH setup.

Finally, using Eq. 179, the deformations *z*(*x,y*) of the laser microweld can be determined as

$$z(x,y) = \frac{OP(x,y)}{2} \quad . \tag{180}$$

Equation 175 yields spatial distribution of deformations of laser microweld.

6.3.2.1.2. Results of OEH measurements

The system setup for the OEH measurements of deformations of the laser microwelds is shown in Fig. 6.18.

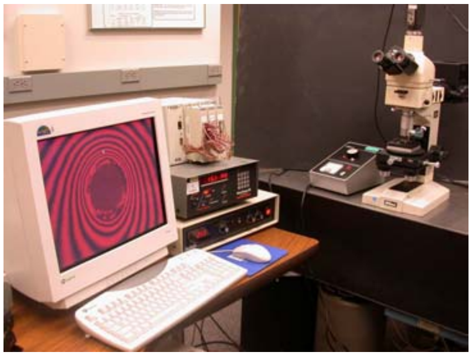

Fig. 6.18. System setup for OEH measurements.

To provide reference for comparison, flatness of the workpiece was measured before it was laser microwelded, Fig. 6.19a. The corresponding analyzed flatness of the workpiece is shown in Fig. 6.19b, with the maximum surface deformation of 0.40 µm.

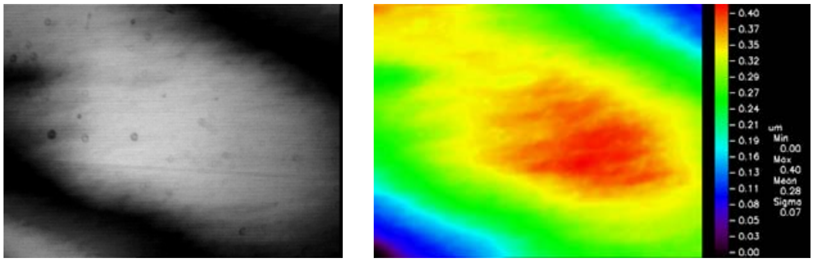

(a) (b)

Fig. 6.19. Measurement of flatness: (a) OEH fringe pattern corresponding to flatness (i.e., initial deformation) of the workpiece, before the laser microwelds were made, (b) 2D deformation of the workpiece corresponding to the OEH fringe pattern of (a).

After measuring the deformation of the unwelded workpiece, the Nd:YAG laser operating at the wavelength of 1064 nm was used to make the laser microwelds. The energy of the laser beam was 5 J, pulse length was 4 ms, and the spot diameter was 80 μm.

Copper was used as the working material, and the thickness was 0.1 mm. The workpiece was secured in a rectangular holder, and the microwelds are made at the center of the rectangular window. Representative OEH measured fringe pattern representing deformations surrounding a typical laser microweld is shown in Fig. 6.20a and the corresponding deformation is shown in Figs 6.20b and 6.20c.

As can be seen in Figs 6.20b and 6.20c, the maximum deformation is 2.52 μm; the deformation is not uniform on the surface of the workpiece. Furthermore, using the 3D deformation field shown in Fig. 6.20c, we can draw a line across the center of the laser microweld, or any other part, and the detailed values of the deformation along this line can be obtained as shown in Fig. 6.21; the same information can also be obtained from Fig. 6.20b. The displayed zero deformation in the middle of the microweld is due

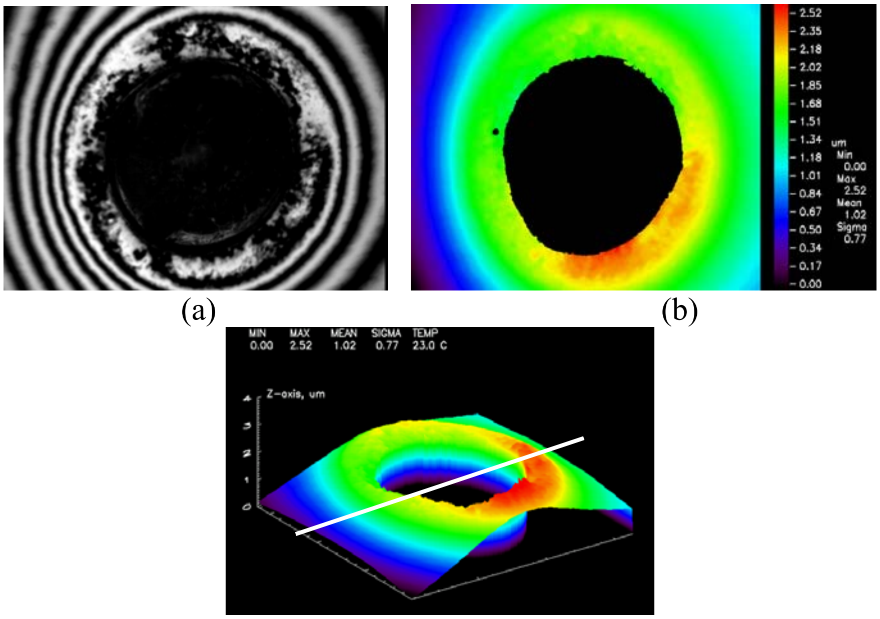

(a) (b)

(c)

Fig. 6.20. OEH measurement of deformation of the laser microweld made using $E = 5$ J, $t = 4$ ms, $f = 1$ Hz, and $N = 1$: (a) OEH fringe pattern, (b) 2D deformation field, (c) 3D deformation field.

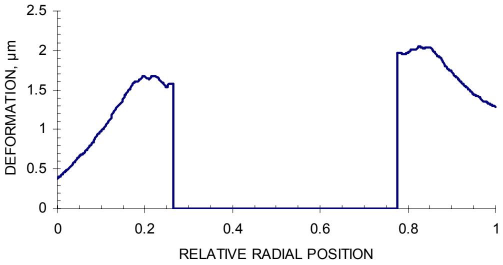

Fig. 6.21. Representative results for the detailed deformation along a line through the center of the laser microweld.

to low modulation of the OEH measurements because of the out-of-focus condition (Han, 2003). This measurement condition can be resolved using another method such as, e.g., the confocal microscopy (Furlong et al., 2003).

Representative OEH fringe patterns and the corresponding 3D deformations for laser energy levels at 4 J and 6 J with pulse length of 4 ms are shown in Figs 6.22 and 6.23, respectively. As can be seen in Figs 6.21 to 6.23, the deformation fields of the microwelds are different for different laser powers used. Based on the calculation of the required energy for performing the laser microwelding for the specific material used in the experiments, Eqs 120 to 125, 5 J is the optimal energy level, while 4 J provides less than the required energy, and 6 J creates over-heating problem. In addition, for each energy level (4 J, 5 J, and 6 J), numbers of microwelds were made under the same conditions, and the statistical results show that, when the laser energy was 5 J, the workpiece has maximum deformation, while when the workpiece was under-heated (4 J) or over-heated (6 J), the maximum deformations decrease. Therefore, it is very important to control the laser energy so that to achieve desired results of the microwelds. In addition, the method of how to secure the workpiece has significant effect on the deformation field, therefore it needs to be characterized in theory and carefully controlled during the experiments.

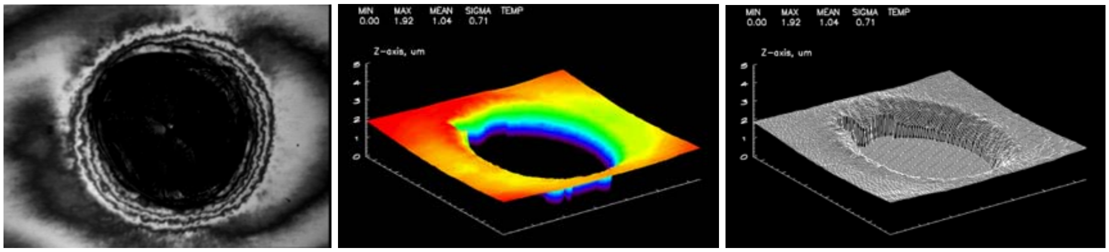

(a) (b) (c)

Fig. 6.22. OEH measurement of deformations of the laser microweld made using $E = 5$ J, $t = 4$ ms, $f = 1$ Hz, and $N = 1$: (a) OEH fringe pattern, (b) 3D deformation field, (c) 3D wireframe of deformation.

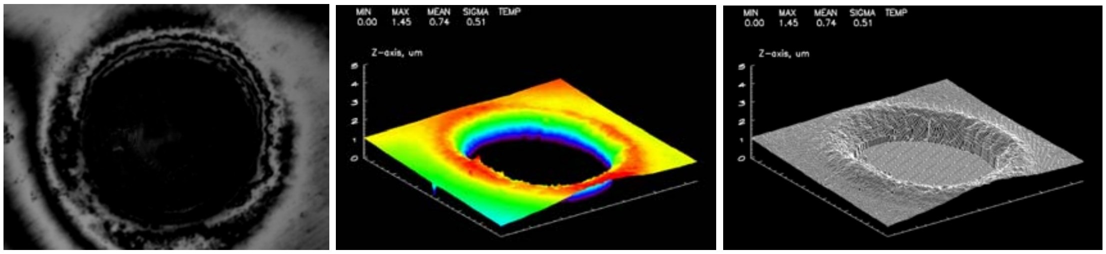

(a) (b) (c)

Fig. 6.23. OEH measurement of deformation of the laser microweld made using $E = 5$ J, $t = 4$ ms, $f = 1$ Hz, and $N = 1$: (a) OEH fringe pattern, (b) 3D deformation field, (c) 3D wireframe of deformation.

6.3.2.2. Tensile tests for the strength of laser microwelds

A laser weld between two components inevitably results in a modification of mechanical properties such as tensile strength, and longitudinal tensile tests are commonly used to evaluate the strength and elongation of laser welds in metals. Tensile failure usually occurs due to increased hardness in the weld and HAZ (Duley, 1999).

Strength testing is an important aspect of a weldability study in laser welding, and among all tests, static tensile-shear testing is the most common laboratory test used in the determination of weld strength because of its simplicity. The system setup for the tensile strength measurements of laser microwelds used in the research of this Dissertation is shown in Fig. 6.24, where the Instron 5500 universal materials test system (Instron, 2000) was used, and the laser microwelded workpiece was secured by the wedge action grips at both ends, Fig. 6.24b. The free body diagram of the forces and moments applied on the microweld in the tensile-shear testing is shown in Fig. 6.24c.

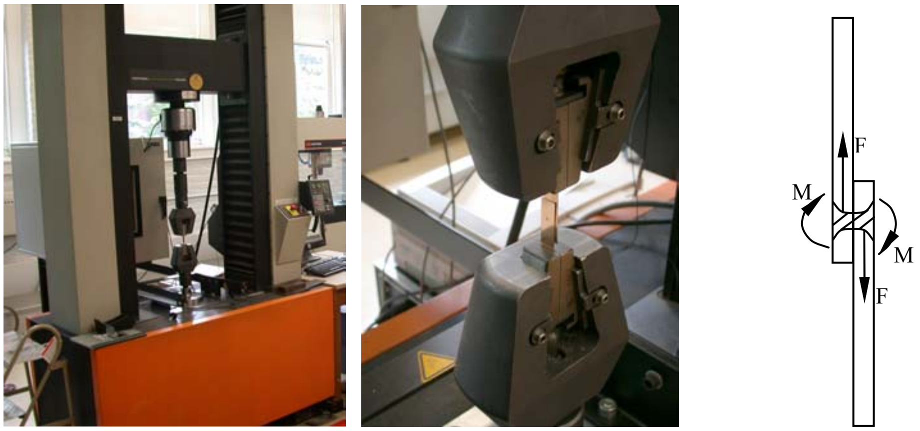

(a) (b) (c)

Fig. 6.24. System setup for tensile tests: (a) Instron 5500 tensile test machine, (b) loading fixture, (c) free body diagram of a test sample.

Tensile-shear testing results are influenced not only by the quality of spot welds, but also by the dimensions of testing specimens. According to the standards and specifications for tensile-shear tests in order to obtain desirable failure modes, which takes into consideration the influence on the measurement of the quality of the weld by its strength and the constraint imposed by its surrounding, the specimen width must be greater than two times the spot weld diameter, the overlap need to have at least equal size to the specimen width, and the length of the specimen is required to be long enough to avoid pronounced reduction in the measured strength (Zhou et al., 1999). Therefore, in the tensile tests conducted in this Dissertation, copper workpiece with length of 10 cm, width of 1 cm, and thickness of 0.1 mm was used, the overlaps between two microwelded workpiece was 3 cm, and the microwelds were made at the center of the overlaps. Note that the typical diameter of a laser microweld produced in the experiments in this Dissertation was about 500 to 700 micrometers, as shown in Fig. 6.14.

In the experiments, the displacements at different load conditions were recorded, and the force-extension curves were measured for the workpiece with laser spot microwelds made at different power levels and also with different number of microwelds. The most commonly monitored variable in tensile-shear testing is the peak load, and the tensile strength can be calculated at the peak load because the failure of specimens is basically determined at such a moment, and the displacement and load become not unique after the load reaches its peak value because of the uncertainty in tearing the specimens.

The workpieces with different microwelding powers were first tested, as shown in Fig. 6.25, where the laser energy of 5 J and 6 J were used with a constant pulse length of 4 ms, and the single microwelds for each specimen were made at the center of the overlap. For the microwelds made with 5 J and 6 J, Figs 6.25a and 6.25b, the maximum tensile forces in these curve are 67.60 N and 90.34 N, respectively, and the tensile strengths can be calculated by dividing the maximum forces by the cross sectional areas of the microwelds (Boyer, 1987), which were measured at the HAZ after the microwelds joint were broken. Note that the bending moments in the order of less than 0.1 N-m were determined not to affect the results. The calculated tensile strengths of the microwelds with the laser energies of 5 J and 6 J both have lower values than the tensile strength of the base material, which is due to the increase of hardness at the HAZ of the microweld (Han and Pryputniewicz, 2003b). Furthermore, the tensile strength of the microwelds made with higher laser power (6 J, 4 ms) showed a slightly higher value than the lower power case (5 J, 4 ms), as calculated in Appendix E.

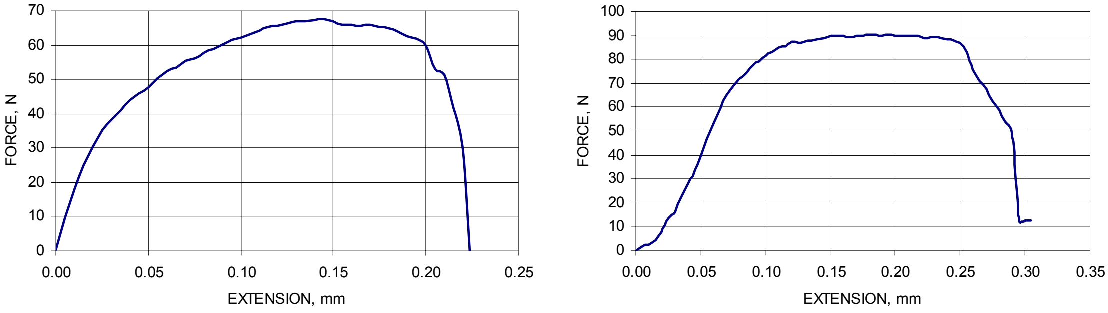

(a) (b)

Fig. 6.25. Force-extension measurements for laser microwelded workpieces under different laser power levels, with a single microweld, at $t = 4$ ms, $f = 1$ Hz, and $N = 1$: (a) $P = 1.25$ kW, (b) $P = 1.5$ kW.

Force-extension curves were also measured for workpieces with different number of microwelds, Fig. 6.26, where the laser energy of 5 J and pulse length of 4 ms was used. For the workpiece with two microwelds that were 5 mm apart and aligned along the direction of the force, the force-extension curve is shown in Fig. 6.26a. This figure exhibits a localized, heterogeneous type of transition from elastic to plastic deformation that produces a yield point in the force-extension curve, and the value of the yield point depends on the stiffness of the material (Benham and Crawford, 1987). Note that for one microweld on the workpiece, Fig. 6.25, there are no yield points exhibited. The maximum force in Fig. 6.26a is 150.25 N, and the calculated tensile strength of the workpiece with two microwelds is lower than the tensile strength of the base workpiece material. For the workpiece with three microwelds that were 5 mm apart and aligned in a line along the direction of the force, the force-extension curve is shown in Fig. 6.26b. This figure exhibits a similar localized, heterogeneous type of transition from elastic to plastic deformation that produces a yield point in the force-extension curve as for the case with two microwelds, and the maximum force in Fig. 6.26b is 191.97 N, and the calculated tensile strength of the workpiece with three microwelds is also lower than the tensile strength of the base workpiece material.

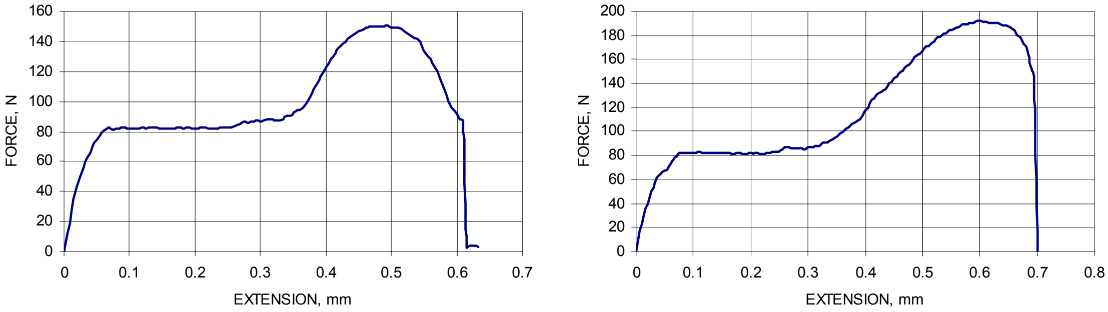

(a) (b)

Fig. 6.26. Force-extension measurements for laser microwelded workpieces, with multiple laser microwelds, at $E = 5$ J, $t = 4$ ms, $f = 1$ Hz, and $N = 1$ per weld: (a) two microwelds, (b) three microwelds.

More tensile tests for different number of microwelds and different microweld patterns, such as aligned in a triangular shape for three microwelds or in a rectangular shape for four microwelds, were conducted and the calculated tensile strengths of the workpiece with these microwelds were all lower than the tensile strength of the base workpiece material.

6.4. Correlations between computational and experimental investigations

In order to validate computational investigations, the results for temperature distributions and fusion zone profiles calculated from FDM program were compared with experimental results, and the discrepancies are discussed in the following sessions.

6.4.1. Temperature distributions

The laser used in this Dissertation was a Lasag Nd:YAG model KLS 126 pulsed laser that emits a beam at a wavelength of 1064 nanometers. The workpieces were secured (one at a time) by a rectangular plate with a square hole in the middle, so that the laser beam could irradiate the exposed workpiece in the middle of the clamp plate.

For the temperature measurements, several thermocouples were attached to the bottom surface of the workpiece, with different distances from the laser beam center, as shown in Fig. 6.27. National Instruments PCI E data acquisition board with the auxiliary SCXI chassis and SCXI-1122 modulus were used in the temperature measurements (NI, 1999a, 1999b, 1999c), and the temperature profiles were recorded using National Instruments LabVIEW software (Ver. 6.0) (NI, 2000). The sampling rate of the temperature recording was 4000 Hz.

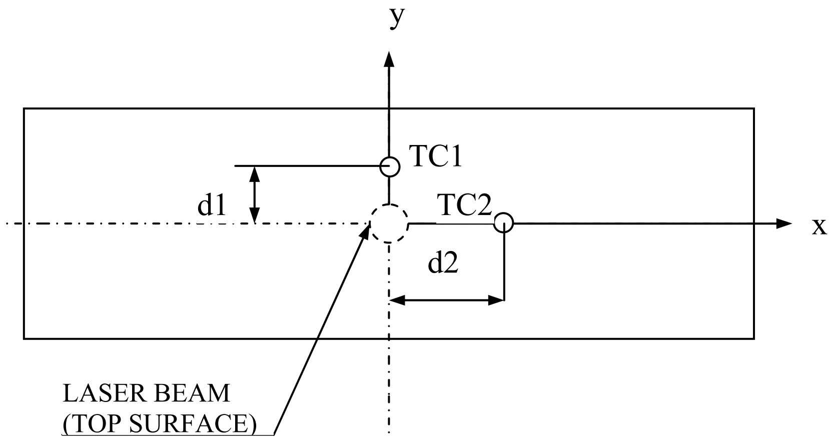

d1 = 1 mm, d2 = 1.5 mm

Fig. 6.27. Bottom view of the workpiece, with the locations of thermocouples relative to the laser beam (not to scale), measured within ±0.025 mm.

The thermocouples used in this study were of type T (copper and copper-nickel alloy) and have the wire diameter of 76 μm (0.003 in). The copper and copper-nickel wires were welded together with the bead size of 0.190 mm. The thermocouples were attached on the bottom surface of the workpiece using Omega's CC high temperature cement. The effective thermal time constant for these thermocouples was 12 ms. This time constant was used in interpretation of temperature-time history of the test samples.

Temperature variations at different points on the bottom surface of the workpiece were recorded, and the typical values are shown in Fig 6.28, where detailed temperature profiles for each of these thermocouples were recorded for 40 ms of the microwelding process. Although the laser pulse length was only 4 ms, thermal effects in the workpiece last significantly longer. Note that the temperature profiles during the laser microwelding processes are nonlinear.

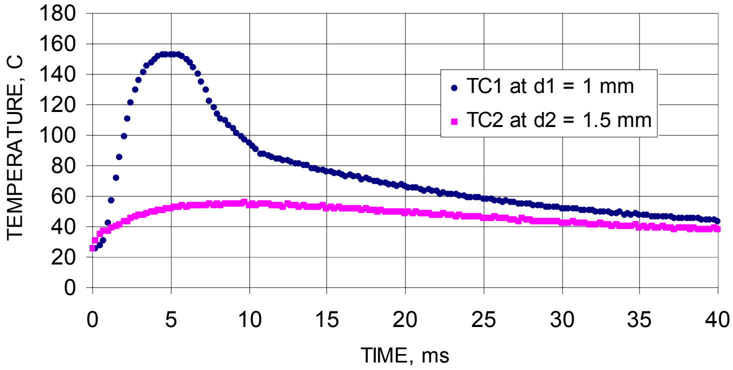

Fig. 6.28. Experimental temperature measurements for each thermocouple during laser microwelding process.

As can be seen from Fig. 6.28, for the measured point at about 1 mm away from the center of the laser beam, the temperature experienced a significant increase during the laser pulse duration. However for the points which are about 1.5 mm away from the beam center, only very slight temperature changes occurred, which indicates that laser welding results in very large temperature gradients, due to the high power intensity and the short pulse duration.

In order to validate the computational method to predict the temperature distribution of laser beam interaction with metals, it is important to compare the computational solutions with the experimental results. Because of the limitation of the attachment method of the thermocouples on the surface of the workpieces, it is only meaningful to use the data obtained in the computational results for the temperature variations which are located more than 1mm away from the laser beam center. Therefore, the data for the temperature at the point of 1 mm and 1.5 mm away from the laser center were compared and are shown in Figs 6.29 and 6.30. Figure 6.29 shows the temperature changes as the function of time for the node on the bottom surface; the node was 1 mm away from the center of the laser beam. Figures 6.30 shows the temperature changes as the function of time for the node at bottom surface, which was 1.5 mm away from the center of the laser beam.

The data shown in Figs 6.29 and 6.30 were obtained using copper workpiece, and had the dimensions of 1 cm by 1 cm by 0.1 mm. A single pulse mode of KSL126 Nd:YAG laser was used with the pulse duration of 4 ms and the energy output of 5 J. The laser beam interaction, during which temperature was measured, was in air under free convection. The FDM simulation was also performed for the case of free convection in air, which facilitated correlation with the experimental results.

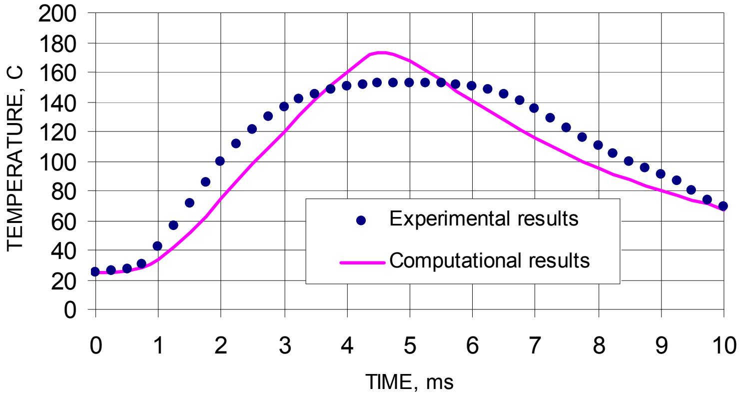

Fig. 6.29. Comparison of computational and experimental results of temperature as a function of time, at a point 1mm away from the center of the beam, on the bottom surface of the workpiece.

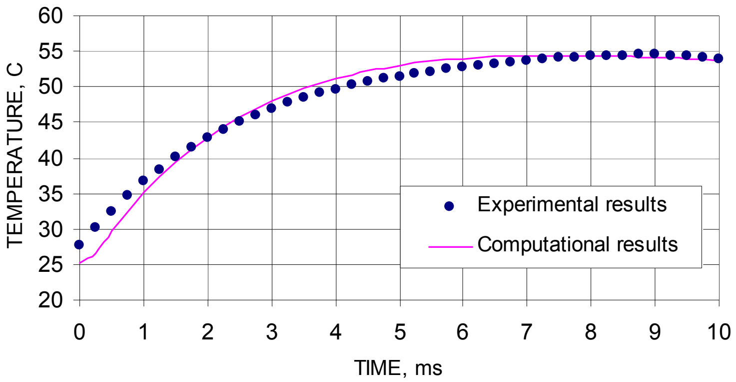

Fig. 6.30. Comparison of computational and experimental results of temperature as a function of time, at a point 1.5 mm away from the center of the beam, on the bottom surface of the workpiece.

As can be seen from Figs 6.29 and 6.30, both computational and experimental results show that, at the locations that are more than 1 mm away from the laser beam center, the temperature changes due to the laser beam irradiation on the workpiece were small. This is because of the small spot size of the laser beam and the very short laser pulse length, also due to the good heat conductivity of copper.

Discrepancies between the theoretical and experimental results are caused by the assumptions in the theoretical model and uncertainties in temperature measurements. The assumptions in the theoretical model that might cause the differences between the computational and experimental results are:

1. In the computational model, it was assumed that the laser energy output was 5 J, and it was uniformly distributed during the 4 msec pulse duration. Furthermore, it was assumed that part of the laser power was absorbed by the workpiece with the surface absorption coefficient equals to 0.1. However,

because of the energy loss during the laser beam propagation in the air before it reaches the workpiece, and also because of the change of energy absorption coefficient due to temperature change, the surface absorption is not a constant. Therefore, there may be a difference of laser power between the computational model and experimental situation.

2. It was assumed in the FDM model that the convection heat loss on the surfaces of the workpiece was free convection, and the heat transfer coefficient h was calculated as the function of surface temperature only. However, due to the high temperature and high pressure and the resultant complex plasma phenomena, the heat transfer coefficient need to be modeled in details based on fluid dynamics theory, as it can significantly affect the results (Steen, 1991).
3. For the radiation heat loss, the surface emissivity ε was assumed to be the constant at the value of 0.1. This is the very rough estimate; more accurate considerations should be taken into account as the function of surface temperature, surface roughness, and the existence of plasma cloud. Since emissivity strongly depends on temperature, more experiments need to be performed to determine this value more accurately.
4. It was assumed that the thermal conductivity of the workpiece (copper) was as shown in Table C.1 in Appendix C. These values were obtained from literature, the conditions at which they were determined were not specified in details, and the values were given only up to 900°C. Therefore, it is not

known how well they relate to the specific experimental conditions used in this Dissertation. Therefore, there is the need to find k values corresponding to different phase conditions of experiments conducted in this Dissertation.

5. In the FDM model, the energy absorption coefficient was assumed to be either a constant or follow the data in Fig. 4.10. However, large uncertainty exists in the real value of the energy absorption coefficient, especially because the large temperature range and the multiple phase changes that the workpiece materials experience. Therefore, detailed measurement for the energy absorption coefficient need to be performed.

In the experiments, there are several parameters that have large uncertainty because of the uncertainties in the measurements of temperature. First, due to the very short laser pulse duration, it requires that the thermocouple responses to be very fast. Although the thermocouples used in this study were the smallest that could be handled, at this time, they still could not satisfy the requirement for the fast response speed needed to reliably measure temperature changes. Second, it was difficult to control accuracy and precision of the location of the thermocouples on the surface of the workpiece, because of the large contact area, relative to the cross sectional area of the laser beam, required for attaching the thermocouples onto the surface. Therefore, large errors may be caused by this effect. Finally, since the voltage magnitudes of the thermocouples output were very small, and the data acquisition board (SCXI-1122) used in this study has limited resolution, the calibration of the thermocouples may be affected and may cause the differences between the real temperature of the workpiece and the measured temperatures.

6.4.2. Melting zone profile

In laser microwelding, the materials in the HAZ experience heating, melting, and resolidification, and the microstructures inside the HAZ have altered, as shown in Fig. 6.31, when proper etchant for copper was used to view the change in microstructure. Note that in Fig. 6.31, *D_front* = 705 µm, *D_min* = 368 µm, and *D_back* = 464 µm, and the thickness of the microwelded workpiece was 0.2 mm.

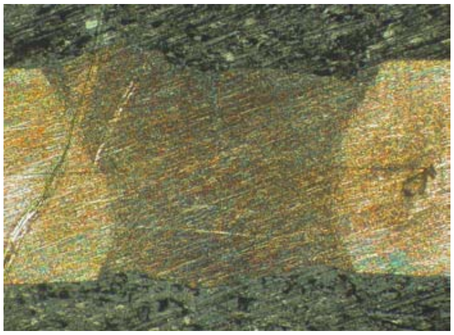

Fig. 6.31. Optical image of the cross sectional view of a laser microweld after etching.

From the calculated temperature profiles based on the FDM program developed in the preparation of this Dissertation, melting isotherms were output into files and therefore can be compared with the contours of the HAZ shown in the optical image. With the first trial that, under the assumption that the energy coefficient was 0.012 and was kept as a constant for all temperature ranges, the melting isotherm is shown in Fig. 6.32.

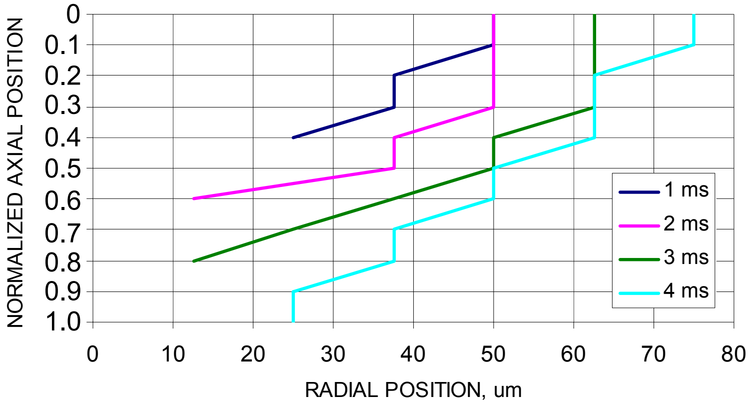

Fig. 6.32. Computational results of isotherms at melting temperature for different time steps in the workpiece for laser microwelding.

Figure 6.32 shows the isotherms at the melting temperature for the half-model of the cross section of the laser microweld, the zero position in the radial direction indicates the centerline of the microweld, and the zero position in the normalized axial direction represents the top surface of the workpiece. The maximum radius of the melting zone in Fig. 6.32 was about 75 µm, which is much smaller than the measured melting radii. Based on the data for energy absorption coefficient for copper, as shown in Fig. 4.10, the “Adjust absorption” icon in the FDM interface was checked and the temperature profiles were re-calculated, and the isotherms are shown in Fig. 6.33.

In Fig. 6.33, the maximum radius of the melting zone was about 125 µm, which is smaller than the measured melting radii, as shown in Fig. 6.31.

Furthermore, in order to investigate whether the effect of surface roughness on the surface reflectivity of the copper workpiece need to be accounted for in the

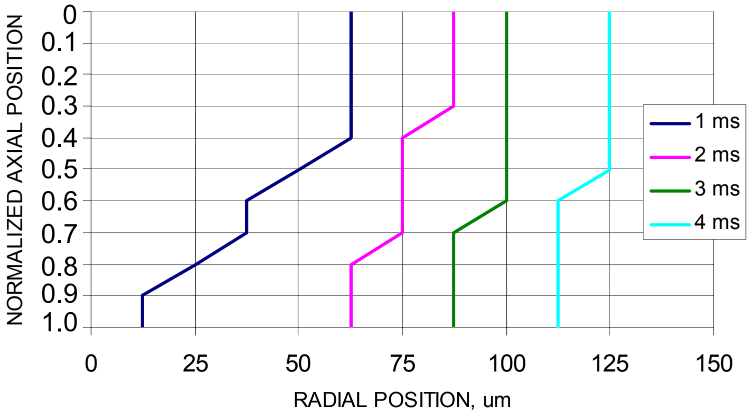

Fig. 6.33. Computational results of isotherms at melting temperature for different time steps in the workpiece for laser microwelding, after adjustment for energy absorption coefficient based on the data in Fig. 4.10.

computational models, DEKTAK 3 surface profile measuring system was used (Veeco Instruments, 2001), and the measurement of surface roughness of the copper workpiece is shown in Fig. 6.34, which shows the root-mean-square surface roughness of 73.5 nm. Using Eq. 128 in Chapter 4, for the reflectivity R^* of an opaque surface at normal incidence with the root-mean-square roughness σ, it was calculated as the same value as for R, which is the normal incidence reflectivity of the smooth surface. Therefore, it can be seen that due to the small value of the surface roughness of the copper workpiece, the reduction in reflectivity arises from the diffusely scattered workpiece that redirects incident laser radiation away from the normal to the surface was very small, therefore, in this case, it is not necessary to account for the reduction of reflectivity due to surface roughness.

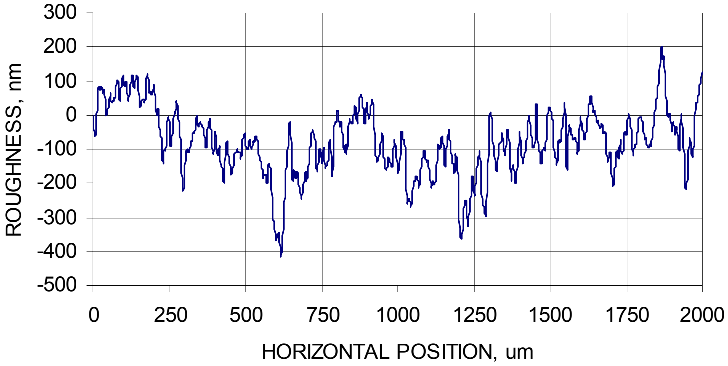

Fig. 6.34. Measurement of surface roughness of the copper workpiece, with the uncertainty of 10 nm.

Therefore, additional fluid dynamic considerations need to be accounted for the convection flow inside the weld pool, that is, the convection mechanism due to the buoyancy force, the surface tension gradient at the weld pool surface, and the shear stress acting on the pool surface by the plasma, so that to obtain the detailed profiles of the weld pool. Furthermore, complete information of the material properties of the workpiece as the function of temperature need to be obtained, in order to calculate the melting profiles of the microwelds and obtain good correlation with experimental data.

7. CONCLUSIONS AND FUTURE WORK

The objectives of this Dissertation were to investigate and develop a better understanding of the fundamental processes of laser microdrilling and microwelding in metallic materials than available until this time. Based on the properties of the laser system, the workpiece, and the environmental conditions, the general models of the laser micromachining processes were developed for the configuration of interest in this Dissertation. Studies included analytical, computational, and experimental investigations of the interaction of a laser beam with metallic workpieces of finite size.

In the analytical studies, the governing equations of the heat transfer problem during laser micromachining were developed and solved to obtain the temperature distributions. Energy transportations in multiple phases were investigated in detail for laser microdrilling and microwelding processes. In addition, thermal stress and strain in the laser micromachining processes were characterized, as they could significantly affect the quality and functionality of the laser micromachined parts. Furthermore, detailed investigations were performed to determine the effects that laser beam properties, energy absorption at the surface of the workpiece, shielding gas mechanisms, and energy loss due to surface emissivity have on the quality of laser micromachining.

The computational investigations included development of computer interface based on finite difference method (FDM) to solve the nonlinear heat transfer equations, including nonlinear material properties as the function of temperature, laser power distributions, coefficient of energy absorption, and trace the variation of convection and radiation heat losses during laser micromachining process. The second part of computational investigations was using finite element method (FEM) and software to solve for temperature distributions and mechanical problems, such as stress/strain and deformations during the laser micromachining process. Results from computational investigations were then compared with experimental data, and they showed reasonable correlations, some discrepancies were identified, and reasons for these discrepancies were discussed and methods of how to improve the results were proposed.

In the experimental investigations performed during this Dissertation, laser microdrilling and microwelding experiments were conducted using stainless steel 304 workpiece and copper workpiece, respectively, and the workpiece was processed by a pulsed Nd:YAG laser which had the typical spot diameter of 80 μm. The experimental investigations of the laser microdrilling and microwelding processes include the SEM characterization of surface topography of laser micromachined spots, parametric investigations of the effects of system parameters on microdrilling and microwelding results, optoelectronic holography (OEH) measurements of the thermal deformations, tensile tests to measure the strength of the laser microwelds, and temperature measurements of the laser micromachined workpiece using thermocouples.

Following is a summary of the results and observations obtained during this Dissertation:

1) laser micromachining is a thermal process that strongly depends on the thermal properties of the workpiece,
2) a graphical computer interface was developed based on FDM to determine the temperature distribution of the workpiece under the laser beam irradiation;

this model can be applied to various types of laser micromachining processes, such as laser microdrilling, laser microwelding, etc., and has the capabilities of adjusting the nonlinear material properties of the workpiece, i.e., material properties as the function of temperature, various power distributions of the laser beam, and the energy absorption coefficient due to temperature change,

3) for Gaussian power distribution, it resulted in a much higher value of the maximum temperature inside the workpiece than that for uniform power distribution, therefore leading to a much higher level of thermal stress,
4) the computational model needs to account for the fluid dynamics of the weld pool in order to accurately predict the shape of the HAZ,
5) for laser microdrilling, the threshold intensity at the onset of the beam breakthrough was greater than the value predicted using the empirical equation,
6) considering system parameters, the laser peak power had the most significant effect on the dimensions of the holes while the laser focal plane position had the second most significant effect, out of the system parameters that were considered,
7) for laser percussion drilling, the first pulse after the beam breakthrough always produced poor circularity of the hole, however the hole formed by the first pulse was comparable to the final size of the finished hole,
8) for laser microwelding, the laser focal plane position had the most significant effect on the dimensions of the microwelds,

9) a novel optoelectronic holography (OEH) methodology, which provided non-contact full-field displacements and deformations measurements with sub-micrometer accuracy, was utilized for measurements of thermal deformations of the laser microwelds,
10) tensile tests were performed for laser microwelded parts with different number of microwelds and in different patterns, the strength of laser microwelds was always smaller than the strength of the base material, due to decrease in values of properties of the materials inside the HAZ,
11) various measurement techniques (e.g., optical microscope, SEM, surface profiler device, specific etching method) were used to determine characteristics of the laser micromachined components, and the experimentally determined values were used in computational models for more accurate calculations,
12) temperature measurements were performed using computer based thermocouple apparatus that provided multi channel capabilities with 4000 Hz sampling rates. This apparatus should be enhanced to obtain sampling rates about one order of magnitude faster than currently possible, and the size of the thermocouples should be reduced to be more compatible with the large temperature gradients under or close to the center of the laser beam, in order to reduce uncertainty in temperature measurements which will facilitate correlation between computational and experimental results for the temperature distributions.

Although a great number of studies have been performed on the general subject of laser materials processing, and more specifically, concentrated on microdrilling and microwelding, still a number of aspects remain to be investigated in depth before lasers can be employed, to their full potential, in materials processing, especially due to increasing demand for microelectronic and packaging applications. The exact nature of the interrelationships among the various process parameters is still not fully understood, therefore no complete models were developed that could produce good correlations between computational and experimental results.

Listed below are several tasks that should be accomplished as a continuation of the investigation presented in this Dissertation:

1) determination of laser beam propagation properties, and further development of beam guiding and shaping components to facilitate accurate beam delivery system in flexible laser machining,
2) determination of surface absorption/reflection characteristics of the workpiece during the period of laser beam interaction with metals, especially to determine the variation due to phase change and temperature change during the laser materials processing,
3) further development of the computational model for characterizing the melt/vapor propagation based on fluid dynamics theory, and combined with the thermomechanical models of laser micromachining,
4) further development of the computational model for characterizing the plasma blocking effect on the energy absorption in the workpiece,

5) account for various metallurgical aspects such as the grain size, microcrack and its propagation in the computer interface, for some specific materials,
6) improvement of temperature measuring devices so that the temperature can be read faster and the thermocouples can be located more accurately,
7) development of new applications for laser processes in different industrial/practical cases.

The above listed tasks can be summed up by the objective of efficient predicting and monitoring of the laser micromachining processes based on laser beam analysis and evaluation of quality of the final products. Future advances in the complex processes of laser beam interaction with materials will depend on a closed-loop control of operational functionality of the system.

The research of this Dissertation showed viability of the laser system for micromachining, and addressed considerations that need to be accounted for in order to fully understand, develop computational models to predict, and obtain optimum control for laser micromachining processes. The benefit can then be utilized in the fast-growing laser micromachining applications and be extended to optimize the processing techniques of various sizes and different materials, and enable the emerging technologies relating to sensors/actuators and micromechanisms of the future.

8. REFERENCES

S. I. Anisimov and V. A. Khokhlov, 1995, *Instabilities in laser-matter interaction*, CRC, Boca Raton, FL.

M. K. Apalak, K. Aldas, and F. Sen, 2003, “Thermal non-linear stresses in an adhesively bonded and laser spot welded single-lap joint during laser-metal interaction,” *J. Materials Processing Technology*, 142:1-19.

S. Baik, S. Park, C. Kim, and S. Kim, 2001, “Holographic visualization of laser-induced plume in pulsed laser welding,” *Optics and Laser Technology*, 33:67-70.

J. R. Barber, 1984, “Thermoelastic displacements and stresses due to a heat srouce moving over the surface of half plane,” *J. Appl. Mech.*, 51:636-640.

A. Bejan, 1993, *Heat transfer*, Wiley, New York, NY.

M. Bertolotti, 1983, *Physical processes in laser-materials interactions*, Plenum Press, New York, NY.

P. P. Benham and R. J. Crawford, 1987, *Mechanics of engineering materials*, Wiley, New York, NY.

H. E. Boyer, 1987, *Atlas of stress-strain curves*, ASM International, Metals Park, Ohio.

G. C. Brown, 1999, *Laser interferometric methodologies for characterizing static and dynamic behavior of MEMS*, Ph.D. Dissertation, Worcester Polytechnic Institute, Worcester, MA.

T. W. Bushman, M. A. Gennert, and R. J. Pryputniewicz, 1993, "Phase unwrapping by least squares error minimization of phase curvature," *Proc. SPIE*, 2003:167-174.

A. B. Cambel, 1963, *Plasma physics and magnetofluid-mechanics*, McGraw-Hill, New York, NY.

H. S. Carslaw and J. C. Jaegar, 1969, *Conduction of heat in solids*, Oxford Press, Great Britain.

C. Chaleard, V. Detalle, S. Kocon, J. L. Lacour, P. Mauchien, P. Meynadier, C. Nouvellon, P. Palianov, M. Perdrix, G. Petite, B. Salle, B., and A. Semerok, 1986, “Influence of laser pulse duration on the ablation efficiency of metals,” *Proc. SPIE*, 3404:441-448.

C. Chan, J. Mazumder, and M. M. Chen, 1988, “Effect of surface tension gradient driven convection in a laser melt pool: three-dimensional perturbation,” *J. Appl. Phys.*, 64:6166-6174.

R. P. Chanberland, 1988, *Experimental and numerical study of laser interaction with a semi-infinite solid*, MS Thesis, Center for Holographic Studies and Laser micro-mechaTronics, Mechanical Engineering Department, Worcester Polytechnic Institute, Worcester, MA.

R. T. C. Choo and J. Szekely, 1994, “The possible role of turbulence in GTA weld pool behavior,” *Welding J.*, 73:25-31.

G. Chryssolouris, 1991, *Laser machining, theory and practice*, Springer-Verlag, New York, NY.

S. D. Conte and C. De Boor, 1980, *Elementary numerical analysis*, 3rd ed., McGraw-Hill, New York.

Y. Dain, P. D., Kapadia, and J. M. Dowden, 1999, “The distortion gap width and stresses in laser welding of thin elastic plates,” *J. Phys. D: Appl. Phys.*, 32:168-175.

J. M. Dowden, 2001, *The mathematics of thermal modeling*, Chapman & Hall/CRC, Boca Raton, FL.

R. Ducharme, K. Williams, P. Kapadia, J. Dowden, B. Steen, and M. Glowacki, 1994, “The laser welding of thin metal sheets: an integrated keyhole and weld pool model with supporting experiments,” *J. Phys. D: Appl. Phys.*, 27:1619-1627.

W. W. Duley, 1985, “Laser materials interactions of relevance to metal surface treatment,” *Proc. NATO Advanced Study Institute on Laser Surface Treatment of Metals,* Italy.

W. W. Duley, 1999, *Laser welding,* Wiley, New York, NY.

A. M. El-Batahgy, 1997, “Effect of laser welding parameters on fusion zone shape and solidification structure of austenitic stainless steels,” *Materials Letters*, 32:155-163.

G. Fan, Y. Guan, J. Zhang, and H. Wang, 1998, “Finite element method analysis for temperature field influence by applied stress during laser processing,” *Proc. SPIE*, 3550:357-365.

R. P. Ferron, 1984, *A preliminary computer simulation for the spot welding of plates*, MS Thesis, Center for Holographic Studies and Laser micro-mechaTronics, Mechanical Engineering Department, Worcester Polytechnic Institute, Worcester, MA.

B. R. Finke, P. D. Kapadia, and J. M. Dowden, 1990, “A fundamental plasma based model for energy transfer in laser material processing,” *J. Phys. D: Appl. Phys.*, 23:643-654.

M. R. Frewin and D. A. Scott, 1999, “Finite element model of pulsed laser welding,” *Welding J.*, 78:15-22.

S. Fujii, N. Takahashi, S. Sakai, T. Nakabayashi, and M. Muro, 2000, “Development of 2D simulation model for laser welding,” *Proc. SPIE*, 3888:115-214.

C. Furlong, R. J. Pryputniewicz, and J. S. Yokum, 2002, "Sensitivity, accuracy, and precision considerations of quantitative optical metrology based on high-spatial and high-digital resolution cameras," *Proc. SPIE*, 4777:74-82.

C. Furlong, J. S. Yokum, and R. J. Pryputniewicz, 2003, "Confocal optoelectronic holography for shape characterization of nanoindentation sites," *Proc. 4th Internat. Symp. on MEMS and Nanotechnology (4th-ISMAN)*, Charlotte, NC, pp. 325-332.

M. Ghoreishi, D. K. Y. Low, and L. Li, 2002, “Comparative statistical analysis of hole taper and circularity in laser percussion drilling,” *Int. J. Machine Tools & Manufacture,* 42:985-995.

Y. Guan, 1998, “Numerical analysis of temperature field during laser heating and cooling,” *Proc. SPIE*, 3550:223-228.

W. Han, 1999, *Theoretical and experimental investigation of laser drilling of small holes in metals*, MS Thesis, Center for Holographic Studies and Laser micro-mechaTronics, Mechanical Engineering Department, Worcester Polytechnic Institute, Worcester, MA.

W. Han and R. J. Pryputniewicz, 2001, "Study of a laser microwelding process for microelectronics and packaging," *Proc. 2001 IMAPS International Symposium on Microelectronics*, pp. 713-716.

W. Han, 2003, "Characterization of thermal deformations in laser micromachining processes for microelectronics and packaging," *Proc. 2003 Student Symposium on Mechanics and Packaging*, pp. 27-28.

W. Han and R. J. Pryputniewicz, 2003a, "Study of thermal stresses in laser microwelding processes for microelectronics industry," *Proc. 2003 SEM Spring Conference*, pp. 546-552.

W. Han and R. J. Pryputniewicz, 2003b, "Mechanical characterizations of laser microwelds for MEMS packaging," *Proc. 2003 MRS Fall Meeting*, in press.

W. Han, 2004, "Investigations of high power laser percussion drilling of small holes in thin metal sheets for microelectronic packaging," *Proc. 2004 Graduate Student Symposium on Mechanics and Packaging*, pp. 61-62.

W. Han, J. S. Yokum, and R. J. Pryputniewicz, 2004, "Parametric study of laser microdrilling process for MEMS fabrication," *Proc. 2004 SEM International Congress & Exposition*, in press.

W. F. Haun, 1968, "Laser applications," *IEEE Spectrum*, 5:82.

G. Herziger, 1986, "Physics of laser materials processing," *Proc. SPIE*, 650:188-194.

G. Herziger, E. W. Kreutz, and K. Wissenbach, 1986, "Fundamentals of laser processing of materials," *Proc. SPIE*, 658:2-10.

R. B. Hetnarski, 1986, *Thermal stresses I*, North-Holland, New York, NY.

R. Ifflander, 2001, *Solid-State lasers for materials processing*, Springer, New York, NY.

Instron, 2000, *Instron 5500 universal materials test system user manual*, Instron Corporation, Canton, MA.

X. Jin and L. Li, 2003, "An experimental study on the keyhole shapes in laser deep penetration welding," *Optics and Lasers in Engineering*, 40:239-246.

K. L. Johnson, 1986, *Contact mechanics*, Cambridge University Press, United Kingdom.

S. Kou, 2002, *Welding metallurgy*, Wiley, New York, NY.

J. Kroos, U. Gratzke, M. Vicanek, and G. Simon, 1992, "Dynamic behavior of the keyhole in laser," *J. Phys. D: Appl. Phys.*, 26:481-485.

Lasag, 1997, *Operator's manual for KLS 126 laser source*, LASAG Corporation, Switzerland.

D. K. Y. Low, L. Li, and A. G. Corfe, 2000, "Effects of assist gas on the physical characteristics of spatter during laser percussion drilling of NIMONIC 263 alloy," *Appl. Surface Science*, 154:689-695.

C. Marley, 2002, "Laser welding photonic devices," *Industrial Laser Solutions*, pp. 9-14.

B. Martin, A. Loredo, M. Pilloz, and D. Grevey, 2001, "Characterization of CW Nd:YAG laser keyhole dynamics," *Optics and Laser Technology*, 33:201-207.

J. Mazumder and W. M. Steen, 1980, “Heat transfer model for cw laser material processing,” *J. Appl. Phys.*, 51:941-947.

J. McGeough, 2002, *Micromachining of engineering materials*, Marcel Dekker, Inc., New York.

I. Miyamoto, 1986, “Beam absorption mechanism in laser welding,” *Proc. SPIE*, 668:11-18.

G. K. L. Ng and L. Li, 2001, “The effect of laser peak power and pulse width on the hole geometry repeatability in laser percussion drilling,” *Optics and Laser Technology*, 33:393-402.

NI, 1999a, *DAQ, PCI E series user manual*, National Instruments Corporation, Austin, TX.

NI, 1999b, *DAQ, SCXI chassis user manual*, National Instruments Corporation, Austin, TX.

NI, 1999c, *DAQ, SCXI-1122 user manual*, National Instruments Corporation, Austin, TX.

NI, 2000, *LabVIEW user manual, Version 6.0*, National Instruments Corporation, Austin, TX.

W. Nowacki, 1962, *Thermoelasticity*, Addison-Wesley, Reading, MA.

T. Nowak, 1990, *Theoretical and experimental investigation of laser drilling in a partially transparent medium*, MS Thesis, Center for Holographic Studies and Laser micro-mechaTronics, Mechanical Engineering Department, Worcester Polytechnic Institute, Worcester, MA.

T. Nowak and R. J. Pryputniewicz, 1992, "Theoretical and experimental investigation of laser drilling in a partially transparent medium," *J. Electronic Packaging*, 114:71-80.

K. Nowakowski, 1990, *Computer simulation and experimental investigation of laser beam interaction with metals*, MS Thesis, Center for Holographic Studies and Laser micro-mechaTronics, Mechanical Engineering Department, Worcester Polytechnic Institute, Worcester, MA.

R. W. Olson and W. C. Swope, 1992, “Laser drilling with focused Gaussian beams,” *J. Appl. Phys.*, 72:3686-3696.

M. A. Ordal, R. J. Bell, R. W. Alexander, L. L. Long, and M. R. Querry, 1985, "Optical properties of fourteen metals in the infrared and far infrared: Al, Co, Cu, Au, Fe, Pb, Mo, Ni, Pd, Pt, Ag, Ti, V and W," *Appl. Opt.*, 24: 4493-4499.

G. M. Oreper, T. W. Eager, and J. Szekely, 1983, "Convection in arc weld pools," *Welding J.*, 62:307-312.

A. Paul and T. Debroy, 1988, "Free surface flow and heat transfer in conduction mode laser welding," *Metall. Trans.*, 19B:851-858.

A. Penz, S. Fazeny, and D. Schuoecker, 1998, "Theoretical and experimental investigation on the role of the oxidation and gas flow in the machining of steel moulds due to melt removal with high power CO_2 lasers," *Proc. SPIE*, 3343:915-926.

N. Postacioglu, P. Kapadia, and J. M. Dowden, 1997, "The thermal stress generated by a moving elliptical weldpool in the welding of thin metal sheets," *Journal of Physics. D: Applied Physics*, 30:2304-2312.

R. J. Pryputniewicz, 1998, *Laser engineering, science, and applications*, Center for Holographic Studies and Laser micro-mechaTronics, Mechanical Engineering Department, Worcester Polytechnic Institute, Worcester, MA.

R. J. Pryputniewicz, 1999, *Holographic numerical analysis*, Center for Holographic Studies and Laser micro-mechaTronics, Mechanical Engineering Department, Worcester Polytechnic Institute, Worcester, MA.

R. J. Pryputniewicz, 2001, *Integrated thermomechanical design and analysis*, Worcester Polytechnic Institute, Worcester, MA.

R. J. Pryputniewicz, 2004, *Thermodynamics of microsystems*, Center for Holographic Studies and Laser micro-mechaTronics, Mechanical Engineering Department, Worcester Polytechnic Institute, Worcester, MA.

R. J. Pryputniewicz and C. Furlong, 2000, "Novel optical-computational approach for NDT applications in microelectronics," *Proc. IX International Congress on Experimental Mechanics*, SEM, Bethel, CT, pp. 1001-1004.

R. J. Pryputniewicz, C. Furlong, G. C. Brown, and E. J. Pryputniewicz, 2001, "Optical methodology for static and dynamic measurements of nanodisplacements," *Proc. of International Congress on Experimental and Applied Mechanics for Emerging Technologies*, Portland, OR, pp. 826-831.

J. F. Ready, 1971, *Effect of high power laser radiation,* Academic, London, UK.

D. A. Rosato, 2002, *Thermal analysis system: user's manual,* Harvard Thermal, Harvard, MA.

J. M. Ruselowski, 1987, "Laser selection for drilling," *Proc. SPIE*, 744:106-123.

V. Semak and A. Matsunawa, 1997, "The role of recoil pressure in energy balance during laser materials processing," *J. Phys. D: Appl. Phys.*, 30:2541-2552.

V. Semak, X. Chen, K. Mundra, and J. Zhao, 1997, "Numerical simulation of hole profile in high beam intensity laser drilling," *Proc. of Laser Materials Processing Conf.*, 81-90.

V. Semak, B. Damkroger, and S. Kempka, 1999, "Temporal evolution of the temperature field in the beam interaction zone during laser material processing," *J. Phys. D: Appl. Phys.*, 32:1819-1825.

V. Semak, G. A. Knorovsky, and D. O. MacCallum, 2003, "On the possibility of microwelding with laser beams," *J. Phys. D: Appl. Phys.*, 36:2170-2174.

A. L. Shaeffler, 1947, "Selection of austenitic electrodes for welding dissimilar metals," *Welding J.*, 26:601-620.

Z. H. Shen, S. Y. Zhang, J. Lu, and X. W. Ni, 2000, "Mathematical modeling of laser induced heating and melting in solids," *Optics and Laser Technology*, 33:533-537.

I. C. Sheng and Y. Chen, 1991, "Thermoelastic analysis for a semi-infinite plane subjected to a moving Gaussian heat source," *J. Therm. Stresses*, 14:129-141.

W. M. Steen, 1991, *Laser material processing*, Springer-Verlag, New York, NY.

W. M. Steen, 1998, *Laser material processing, 2nd edition*, Springer-Verlag, New York, NY.

W. M. Steen, 2003, "Laser material processing — an overview," *J. Opt. A: Pure Appl. Opt.*, 5:3-7.

N. Sumi, R. B. Hetnazske, and N. Noda, 1987, "Transient thermal stresses due to a local source of heat moving over the surface of an infinite slab," *J. Therm. Stresses*, 10:83-96.

W. B. Tiffany, 1985, "Drilling, marking and other applications for industrial Nd:YAG lasers," *Proc. SPIE*, 527:28-36.

H. C. Tse, 2000, "Effect of electric field on plasma control during CO_2 laser welding," *Optics & Laser Engineering*, 33:181-189.

S. A. Tsirkas, P. Papanikos, and T. Kermanidis, 2003, “Numerical simulation of the laser welding process in butt-joint specimens,” *J. Materials Processing Technology*, 134:59-69.

J. Trappe, J. Kroos, C. Tix, and G. Simon, 1994, “On the shape and location of the keyhole in penetration laser welding,” *J. Phys. D: Appl. Phys.*, 27:2152-2154.

H. G. Treusch and G. Herziger, 1986, “Metal precision drilling with lasers,” *Proc. SPIE*, 650:220-225.

L. Tunna, A. Kearns, W. O’Neill, and C. J. Sutcliffe, 2000, “Micromachining of copper using Nd:YAG laser radiation at 1064, 532, and 355 nm wavelengths,” *Optics and Laser Technology*, 33:135-143.

Veeco Instruments, 2001, *DEKTAK 3 surface profile measuring system, installation, operation and maintenance manual*, Veeco Instruments Inc., Santa Barbara, CA.

J. C. J. Verhoeven, J. K. M. Jansen, and R. M. M. Mattheij, 2003, “Modeling laser induced melting,” *Mathematical and computer modeling*, 37:419-437.

M. Vicanek, A. Rosch, F. Piron, and G. Simon, 1994, “Thermal deformation of a solid surface under laser irradiation,” *Appl. Phys.*, 59:407-412.

K. T. Voisey, S. S. Kudesia, W. S. O. Rodden, D. P. Hand, J. D. C. Jones, and T.W. Clyne, 2003, “Melt ejection during laser drilling of metals,” *Materials Science & Engineering*, A356:414-424.

M. Von Allmen, 1976, “Laser drilling velocity in metals,” *J. Appl. Phys.*, 47:5460-5463.

H. Wang and X. Chen, 2003, “Three-dimensional modeling of the laser-induced plasma plume characteristics in laser welding,” *J. Phys. D: Appl. Phys.*, 36:628-639.

R. Webb, 1986, “Thermal modeling of laser materials interaction,” *Proc. SPIE*, 668:112-115.

M. A. Wojcicki and R. J. Pryputniewicz, 1997, "Feasibility study of laser microwelding of high density cable assemblies with applications to portable electronics," *Proc. 47th Electronics Components and Technology Conf.*, San Jose, CA, pp. 905-910.

J. Xie and A. Kar, 1999, “Laser welding of thin sheet steel with surface oxidation,” *Welding J.*, 78:343-348.

X. Xu, G. Chen, and K. H. Song, 1999, “Experimental and numerical investigation of heat transfer and phase change phenomena during excimer laser interaction with nickel,” *Int. J. Heat and Mass Transfer*, 42:1371-1382.

L. J. Yang and Z. M. Xiao, 1995, “Elastic-plastic modeling of the residual stress caused by welding,” *J. Materials Processing Technology*, 48:589-601.

Y. S. Yang and S. H. Lee, 1999, “A study on the joining strength of laser spot welding for automotive applications,” *J. Materials processing technology*, 94:151-156.

B. S. Yilbas, 1987, “Study of affecting parameters in laser hole drilling of sheet metals,” *Trans. ASME: J. Eng. Mat. Tech.*, 109:282-287.

B. S. Yilbas and Z. Yilbas, 1987, “Parameters affecting hole geometry in laser drilling of Nimonic 75,” *Proc. SPIE*, 744:87-91.

B. S. Yilbas and S. Z. Shuja, 1999, “Laser short-pulse heating of surfaces,” *J. Phys. D: Appl. Phys.*, 32:1947-1954.

B. S. Yilbas, S. A. Gbadebo, and M. Sami, 2000, “Laser heating: an electro-kinetic theory approach and induced thermal stresses,” *Optics and Laser Engineering*, 33:65-79.

B. S. Yilbas and A. F. M. Arif, 2001, “Material response to thermal loading due to short pulse laser heating,” *Int. J. Heat and Mass Transfer*, 44:3787-3798.

T. Zacharia, S. A. David, J. M. Vitek, and T. Debroy, 1989, “Weld pool development during GTA and laser beam welding of type 304 stainless steel, part I — theoretical analysis,” *Welding J.*, 68:499-509.

G. Yu, J. Zhang, C. Gao, H. Wang, and P. Li, 1998, “Laser drilling improving circuit board manufacturing,” *Proc. SPIE*, 3550:1-6.

M. Zhou, S. J. Hu, and H. Zhang, 1999, “Critical specimen sizes for tensile-shear testing of steel sheets,” *Welding J.*, 78:305-313.

APPENDIX A. THE FINITE DIFFERENCE EQUATIONS FOR A FINITE OBJECT

This Appendix presents development of the central difference equations for specific nodal elements, which have to be solved in order to obtain a temperature distribution within the metallic object irradiated by a laser beam. The finite difference equations are based on Eq. 2. To facilitate this development, consider the energy balance on one of the nodes shown in Fig. A.1. For example, consider node number 18.

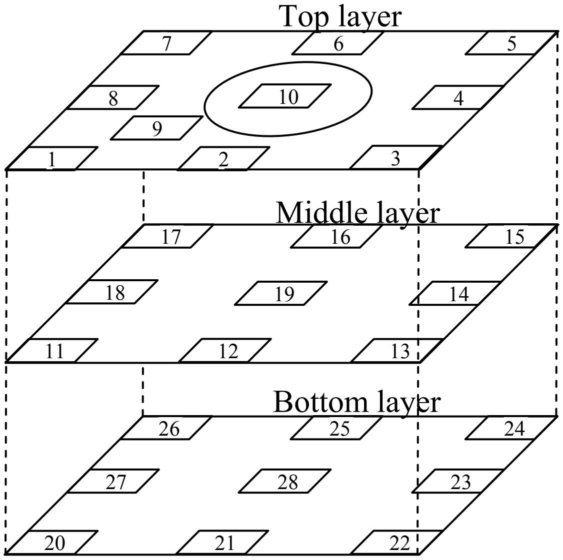

Fig. A.1. Three “layers” of a workpiece.

The first law of thermodynamics and the Fourier’s law applied to the wall node number 18 in Fig. A.2, yield

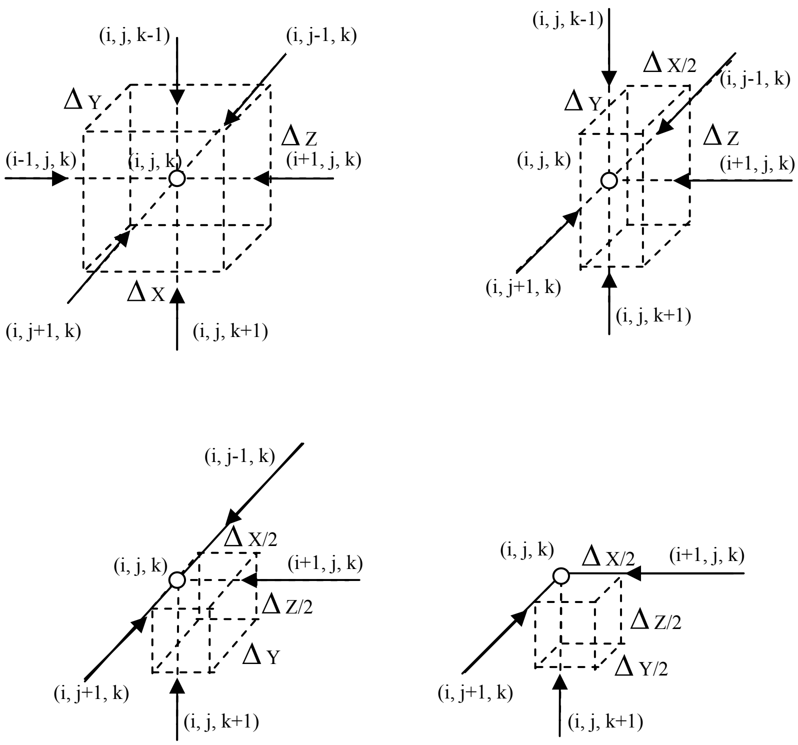

Fig. A.2. The four typical nodal elements of the workpiece.

$$0 = (q_{i-1,j,k} + q_{i+1,j,k})\Delta y\Delta z + (q_{i,j-1,k} + q_{i,j+1,k})\Delta x\Delta z + (q_{i,j,k-1} + q_{i,j,k+1})\Delta x\Delta y + u'\Delta x\Delta y\Delta z \;, \tag{A.1}$$

where

$$\begin{aligned} q_{i-1,j,k} &= -h_{xl}T_{i,j,k} - \sigma\varepsilon {T_{i,j,k}}^{4} \\ &= -\left(h_{xl} + \sigma\varepsilon {T_{i,j,k}}^{3}\right)T_{i,j,k} \\ &= -\left(h_{xl} + {h_{i,j,k}}^{R}\right)T_{i,j,k} \;. \end{aligned} \tag{A.2}$$

Defining

$$h_{xl} + {h_{i,j,k}}^{R} = h_{l} \;, \tag{A.3}$$

where ${h_{i,j,k}}^{R} = \sigma\varepsilon {T_{i,j,k}}^{3}$. Equation A.2 can be rewritten as

$$q_{i-1,j,k} = -h_l T_{i,j,k} \,, \tag{A.4}$$

while heat fluxes in other directions can be defined to be

$$q_{i+1,j,k} = -k \frac{T^t{}_{i+1,j,k} - T^t{}_{i,j,k}}{\Delta x} \,, \tag{A.5}$$

$$q_{i,j-1,k} = -k \frac{T^t{}_{i,j-1,k} - T^t{}_{i,j,k}}{\Delta x} \,, \tag{A.6}$$

$$q_{i,j+1,k} = -k \frac{T^t{}_{i,j+1,k} - T^t{}_{i,j,k}}{\Delta x} \,, \tag{A.7}$$

$$q_{i,j,k+1} = -k \frac{T^t{}_{i,j,k+1} - T^t{}_{i,j,k}}{\Delta x} \,, \tag{A.8}$$

$$q_{i,j,k-1} = -k \frac{T^t{}_{i,j,k-1} - T^t{}_{i,j,k}}{\Delta x} \,, \tag{A.9}$$

$$u' = \frac{\Delta u}{\Delta T} = \rho c \frac{T^{t+\Delta t}{}_{i,j,k} - T^t{}_{i,j,k}}{\Delta t} \,, \tag{A.10}$$

The sign convention adopted in this thesis states that all energy coming into the nodal element is positive, and energy coming out from the nodal element is negative.

The heat fluxes appearing in Eqs A.2 to A.10 are defined as follows:

$q_{i-1,j,k}$	conduction energy flux per unit area in the positive x-direction
$q_{i+1,j,k}$	conduction energy flux per unit area in the negative x-direction
$q_{i,j-1,k}$	conduction energy flux per unit area in the positive y-direction
$q_{i,j+1,k}$	conduction energy flux per unit area in the negative y-direction
$q_{i,j,k-1}$	conduction energy flux per unit area in the positive z-direction
$q_{i,j,k+1}$	conduction energy flux per unit area in the positive z-direction.

Substitution of Eqs A.4 to A.10 into Eq. A.1 yields

$$\begin{aligned}\rho c\frac{T'_{i,j,k}-T_{i,j,k}}{\Delta t}(\Delta x\Delta y\Delta z) &= k\frac{T_{i-1,j,k}+T_{i+1,j,k}-2T_{i,j,k}}{\Delta x}(\Delta y\Delta z)\\ &+k\frac{T_{i,j-1,k}+T_{i,j+1,k}-2T_{i,j,k}}{\Delta y}(\Delta x\Delta z)\\ &+k\frac{T_{i,j,k-1}+T_{i,j,k+1}-2T_{i,j,k}}{\Delta z}(\Delta x\Delta y) \qquad \text{(A.11)}\end{aligned}$$

Equation A.11 can be rearranged as

$$\begin{aligned}T'_{i,j,k}-T_{i,j,k} &= \frac{\kappa\Delta t}{\Delta x^2}(T_{i-1,j,k}+T_{i+1,j,k})+\frac{\kappa\Delta t}{\Delta y^2}(T_{i,j-1,k}+T_{i,j+1,k})+\frac{\kappa\Delta t}{\Delta z^2}(T_{i,j,k-1}+T_{i,j,k+1})\\ &+\frac{\kappa\Delta t}{\Delta z^2}(T_{i,j,k-1}+T_{i,j,k+1}-\left[2\kappa\Delta t\left(\frac{1}{\Delta x^2}+\frac{1}{\Delta y^2}+\frac{1}{\Delta z^2}\right)\right]T_{i,j,k}\ . \qquad \text{(A.12)}\end{aligned}$$

Following the above procedure, the finite difference equations for the remaining 26 nodes can be developed. To facilitate this development, the following coefficients are defined

$$h_1 = h_{xl} + h^R_{i,j,k}\ , \qquad \text{(A.13)}$$

$$h_1' = h_{xr} + h^R_{i,j,k}\ , \qquad \text{(A.14)}$$

$$h_2 = h_{yr} + h^R_{i,j,k}\ , \qquad \text{(A.15)}$$

$$h_2' = h_{yl} + h^R_{i,j,k}\ , \qquad \text{(A.16)}$$

$$h_3 = h_{zl} + h^R_{i,j,k}\ , \qquad \text{(A.17)}$$

$$h_3' = h_{zr} + h^R_{i,j,k}\ , \qquad \text{(A.18)}$$

where $h^R_{i,j,k}$ is the radiation heat transfer coefficient, as defined in Eq. 40.

Using the coefficients given by Eqs A.13 to A.18, and following the proceduring used to obtain Eq. A.12, the following set of 27 finite difference equations was derived, that is, one equation for each of the remaining 27 nodes shown in Fig. A.1.

Node number 1:

$$\begin{aligned} T'_{i,j,k} - T_{i,j,k} &= \frac{2\kappa\Delta t}{\Delta x^2} T_{i+1,j,k} + \frac{2\kappa\Delta t}{\Delta y^2} T_{i,j+1,k} + \frac{2\kappa\Delta t}{\Delta z^2} T_{i,j,k-1} \\ &- \left[2\kappa\Delta t \left(\frac{1}{\Delta x^2} + \frac{1}{\Delta y^2} + \frac{1}{\Delta z^2} \right) + \frac{2\kappa\Delta t}{k} \left(\frac{h_1}{\Delta x} + \frac{h_2}{\Delta y} + \frac{h_3}{\Delta z} \right) \right] T_{i,j,k} \end{aligned} \tag{A.19}$$

Node number 2:

$$\begin{aligned} T'_{i,j,k} - T_{i,j,k} &= \frac{\kappa\Delta t}{\Delta x^2} (T_{i-1,j,k} + T_{i+1,j,k}) + \frac{2\kappa\Delta t}{\Delta y^2} T_{i,j+1,k} + \frac{2\kappa\Delta t}{\Delta z^2} T_{i,j,k-1} \\ &- \left[2\kappa\Delta t \left(\frac{1}{\Delta x^2} + \frac{1}{\Delta y^2} + \frac{1}{\Delta z^2} \right) + \frac{2\kappa\Delta t}{k} \left(\frac{h_2}{\Delta y} + \frac{h_3}{\Delta z} \right) \right] T_{i,j,k} \end{aligned} \tag{A.20}$$

Node number 3:

$$\begin{aligned} T'_{i,j,k} - T_{i,j,k} &= \frac{2\kappa\Delta t}{\Delta x^2} T_{i-1,j,k} + \frac{2\kappa\Delta t}{\Delta y^2} T_{i,j+1,k} + \frac{2\kappa\Delta t}{\Delta z^2} T_{i,j,k-1} \\ &- \left[2\kappa\Delta t \left(\frac{1}{\Delta x^2} + \frac{1}{\Delta y^2} + \frac{1}{\Delta z^2} \right) + \frac{2\kappa\Delta t}{k} \left(\frac{h_1'}{\Delta x} + \frac{h_2}{\Delta y} + \frac{h_3}{\Delta z} \right) \right] T_{i,j,k} \end{aligned} \tag{A.21}$$

Node number 4:

$$\begin{aligned} T'_{i,j,k} - T_{i,j,k} &= \frac{2\kappa\Delta t}{\Delta x^2} (T_{i-1,j,k} + T_{i+1,j,k}) + \frac{\kappa\Delta t}{\Delta y^2} (T_{i,j+1,k} + T_{i,j-1,k}) + \frac{2\kappa\Delta t}{\Delta z^2} T_{i,j,k-1} \\ &- \left[2\kappa\Delta t \left(\frac{1}{\Delta x^2} + \frac{1}{\Delta y^2} + \frac{1}{\Delta z^2} \right) + \frac{2\kappa\Delta t}{k} \left(\frac{h_1'}{\Delta y} + \frac{h_3}{\Delta z} \right) \right] T_{i,j,k} \end{aligned} \tag{A.22}$$

Node number 5:

$$\begin{aligned} T'_{i,j,k} - T_{i,j,k} &= \frac{2\kappa\Delta t}{\Delta x^2} T_{i-1,j,k} + \frac{2\kappa\Delta t}{\Delta y^2} T_{i,j-1,k} + \frac{2\kappa\Delta t}{\Delta z^2} T_{i,j,k-1} \\ &\quad - \left[2\kappa\Delta t \left(\frac{1}{\Delta x^2} + \frac{1}{\Delta y^2} + \frac{1}{\Delta z^2} \right) + \frac{2\kappa\Delta t}{k} \left(\frac{h_1'}{\Delta x} + \frac{h_2'}{\Delta y} + \frac{h_3}{\Delta z} \right) \right] T_{i,j,k} \end{aligned} \tag{A.23}$$

Node number 6:

$$\begin{aligned} T'_{i,j,k} - T_{i,j,k} &= \frac{\kappa\Delta t}{\Delta x^2} (T_{i-1,j,k} + T_{i+1,j,k}) + \frac{2\kappa\Delta t}{\Delta y^2} T_{i,j-1,k} + \frac{2\kappa\Delta t}{\Delta z^2} T_{i,j,k-1} \\ &\quad - \left[2\kappa\Delta t \left(\frac{1}{\Delta x^2} + \frac{1}{\Delta y^2} + \frac{1}{\Delta z^2} \right) + \frac{2\kappa\Delta t}{k} \left(\frac{h_2'}{\Delta y} + \frac{h_3}{\Delta z} \right) \right] T_{i,j,k} \end{aligned} \tag{A.24}$$

Node number 7:

$$\begin{aligned} T'_{i,j,k} - T_{i,j,k} &= \frac{2\kappa\Delta t}{\Delta x^2} T_{i+1,j,k} + \frac{2\kappa\Delta t}{\Delta y^2} T_{i,j-1,k} + \frac{2\kappa\Delta t}{\Delta z^2} T_{i,j,k-1} \\ &\quad - \left[2\kappa\Delta t \left(\frac{1}{\Delta x^2} + \frac{1}{\Delta y^2} + \frac{1}{\Delta z^2} \right) + \frac{2\kappa\Delta t}{k} \left(\frac{h_1}{\Delta x} + \frac{h_2'}{\Delta y} + \frac{h_3}{\Delta z} \right) \right] T_{i,j,k} \end{aligned} \tag{A.25}$$

Node number 8:

$$\begin{aligned} T'_{i,j,k} - T_{i,j,k} &= \frac{2\kappa\Delta t}{\Delta x^2} T_{i+1,j,k} + \frac{\kappa\Delta t}{\Delta y^2} (T_{i,j-1,k} + T_{i,j+1,k}) + \frac{2\kappa\Delta t}{\Delta z^2} T_{i,j,k-1} \\ &\quad - \left[2\kappa\Delta t \left(\frac{1}{\Delta x^2} + \frac{1}{\Delta y^2} + \frac{1}{\Delta z^2} \right) + \frac{2\kappa\Delta t}{k} \left(\frac{h_1}{\Delta x} + \frac{h_3}{\Delta z} \right) \right] T_{i,j,k} \end{aligned} \tag{A.26}$$

Node number 9:

$$\begin{aligned} T'_{i,j,k} - T_{i,j,k} &= \frac{\kappa\Delta t}{\Delta x^2} (T_{i+1,j,k} + T_{i-1,j,k}) + \frac{\kappa\Delta t}{\Delta y^2} (T_{i,j-1,k} + T_{i,j+1,k}) + \frac{2\kappa\Delta t}{\Delta z^2} T_{i,j,k-1} \\ &\quad - \left[2\kappa\Delta t \left(\frac{1}{\Delta x^2} + \frac{1}{\Delta y^2} + \frac{1}{\Delta z^2} \right) + \frac{2\kappa\Delta t}{k} \left(\frac{h_3}{\Delta z} \right) \right] T_{i,j,k} \end{aligned} \tag{A.27}$$

Node number 10:

$$\begin{aligned} T'_{i,j,k} - T_{i,j,k} &= \frac{\kappa\Delta t}{\Delta x^2}(T_{i+1,j,k} + T_{i-1,j,k}) + \frac{\kappa\Delta t}{\Delta y^2}(T_{i,j-1,k} + T_{i,j+1,k}) + \frac{2\kappa\Delta t}{\Delta z^2}T_{i,j,k-1} \\ &\quad - \left[2\kappa\Delta t\left(\frac{1}{\Delta x^2} + \frac{1}{\Delta y^2} + \frac{1}{\Delta z^2}\right) + \frac{2\kappa\Delta t}{k}\left(\frac{h_3}{\Delta z}\right)\right]T_{i,j,k} + \frac{2\kappa\Delta t I(r,t)}{k\Delta z} \end{aligned} \tag{A.28}$$

Node number 11:

$$\begin{aligned} T'_{i,j,k} - T_{i,j,k} &= \frac{2\kappa\Delta t}{\Delta x^2}T_{i+1,j,k} + \frac{2\kappa\Delta t}{\Delta y^2}T_{i,j+1,k} + \frac{\kappa\Delta t}{\Delta z^2}(T_{i,j,k-1} + T_{i,j,k+1}) \\ &\quad - \left[2\kappa\Delta t\left(\frac{1}{\Delta x^2} + \frac{1}{\Delta y^2} + \frac{1}{\Delta z^2}\right) + \frac{2\kappa\Delta t}{k}\left(\frac{h_1}{\Delta x} + \frac{h_2}{\Delta y}\right)\right]T_{i,j,k} \end{aligned} \tag{A.29}$$

Node number 12:

$$\begin{aligned} T'_{i,j,k} - T_{i,j,k} &= \frac{\kappa\Delta t}{\Delta x^2}(T_{i+1,j,k} + T_{i-1,j,k}) + \frac{2\kappa\Delta t}{\Delta y^2}T_{i,j+1,k} + \frac{\kappa\Delta t}{\Delta z^2}(T_{i,j,k-1} + T_{i,j,k+1}) \\ &\quad - \left[2\kappa\Delta t\left(\frac{1}{\Delta x^2} + \frac{1}{\Delta y^2} + \frac{1}{\Delta z^2}\right) + \frac{2\kappa\Delta t}{k}\left(\frac{h_2}{\Delta y}\right)\right]T_{i,j,k} \end{aligned} \tag{A.30}$$

Node number 13:

$$\begin{aligned} T'_{i,j,k} - T_{i,j,k} &= \frac{2\kappa\Delta t}{\Delta x^2}T_{i-1,j,k} + \frac{2\kappa\Delta t}{\Delta y^2}T_{i,j+1,k} + \frac{\kappa\Delta t}{\Delta z^2}(T_{i,j,k-1} + T_{i,j,k+1}) \\ &\quad - \left[2\kappa\Delta t\left(\frac{1}{\Delta x^2} + \frac{1}{\Delta y^2} + \frac{1}{\Delta z^2}\right) + \frac{2\kappa\Delta t}{k}\left(\frac{h_1'}{\Delta x} + \frac{h_2}{\Delta y}\right)\right]T_{i,j,k} \end{aligned} \tag{A.31}$$

Node number 14:

$$\begin{aligned} T'_{i,j,k} - T_{i,j,k} &= \frac{2\kappa\Delta t}{\Delta x^2}T_{i-1,j,k} + \frac{\kappa\Delta t}{\Delta y^2}(T_{i,j+1,k} + T_{i,j-1,k}) + \frac{\kappa\Delta t}{\Delta z^2}(T_{i,j,k-1} + T_{i,j,k+1}) \\ &\quad - \left[2\kappa\Delta t\left(\frac{1}{\Delta x^2} + \frac{1}{\Delta y^2} + \frac{1}{\Delta z^2}\right) + \frac{2\kappa\Delta t}{k}\left(\frac{h_1'}{\Delta x}\right)\right]T_{i,j,k} \end{aligned} \tag{A.32}$$

Node number 15:

$$T'_{i,j,k}-T_{i,j,k}=\frac{2\kappa\Delta t}{\Delta x^2}T_{i-1,j,k}+\frac{2\kappa\Delta t}{\Delta y^2}T_{i,j-1,k}+\frac{\kappa\Delta t}{\Delta z^2}(T_{i,j,k-1}+T_{i,j,k+1})$$
$$-\left[2\kappa\Delta t\left(\frac{1}{\Delta x^2}+\frac{1}{\Delta y^2}+\frac{1}{\Delta z^2}\right)+\frac{2\kappa\Delta t}{k}\left(\frac{h_1'}{\Delta x}+\frac{h_2'}{\Delta y}\right)\right]T_{i,j,k} \tag{A.33}$$

Node number 16:

$$T'_{i,j,k}-T_{i,j,k}=\frac{\kappa\Delta t}{\Delta x^2}(T_{i+1,j,k}+T_{i-1,j,k})+\frac{2\kappa\Delta t}{\Delta y^2}T_{i,j-1,k}+\frac{\kappa\Delta t}{\Delta z^2}(T_{i,j,k-1}+T_{i,j,k+1})$$
$$-\left[2\kappa\Delta t\left(\frac{1}{\Delta x^2}+\frac{1}{\Delta y^2}+\frac{1}{\Delta z^2}\right)+\frac{2\kappa\Delta t}{k}\left(\frac{h_2'}{\Delta y}\right)\right]T_{i,j,k} \tag{A.34}$$

Node number 17:

$$T'_{i,j,k}-T_{i,j,k}=\frac{2\kappa\Delta t}{\Delta x^2}T_{i+1,j,k}+\frac{2\kappa\Delta t}{\Delta y^2}T_{i,j-1,k}+\frac{\kappa\Delta t}{\Delta z^2}(T_{i,j,k-1}+T_{i,j,k+1})$$
$$-\left[2\kappa\Delta t\left(\frac{1}{\Delta x^2}+\frac{1}{\Delta y^2}+\frac{1}{\Delta z^2}\right)+\frac{2\kappa\Delta t}{k}\left(\frac{h_1}{\Delta x}+\frac{h_2'}{\Delta y}\right)\right]T_{i,j,k} \tag{A.35}$$

Node number 18:

$$T'_{i,j,k}-T_{i,j,k}=\frac{2\kappa\Delta t}{\Delta x^2}T_{i+1,j,k}+\frac{\kappa\Delta t}{\Delta y^2}(T_{i,j+1,k}+T_{i,j-1,k})+\frac{\kappa\Delta t}{\Delta z^2}(T_{i,j,k-1}+T_{i,j,k+1})$$
$$-\left[2\kappa\Delta t\left(\frac{1}{\Delta x^2}+\frac{1}{\Delta y^2}+\frac{1}{\Delta z^2}\right)+\frac{2\kappa\Delta t}{k}\left(\frac{h_1}{\Delta x}\right)\right]T_{i,j,k} \tag{A.36}$$

Node number 19:

$$T'_{i,j,k}-T_{i,j,k}=\frac{\kappa\Delta t}{\Delta x^2}(T_{i+1,j,k}+T_{i-1,j,k})+\frac{\kappa\Delta t}{\Delta y^2}(T_{i,j+1,k}+T_{i,j-1,k})$$
$$+\frac{\kappa\Delta t}{\Delta z^2}(T_{i,j,k-1}+T_{i,j,k+1})-\left[2\kappa\Delta t\left(\frac{1}{\Delta x^2}+\frac{1}{\Delta y^2}+\frac{1}{\Delta z^2}\right)\right]T_{i,j,k} \tag{A.37}$$

Node number 20:

$$\begin{aligned} T'_{i,j,k} - T_{i,j,k} &= \frac{2\kappa\Delta t}{\Delta x^2} T_{i+1,j,k} + \frac{2\kappa\Delta t}{\Delta y^2} T_{i,j+1,k} + \frac{2\kappa\Delta t}{\Delta z^2} T_{i,j,k+1} \\ &\quad - \left[2\kappa\Delta t \left(\frac{1}{\Delta x^2} + \frac{1}{\Delta y^2} + \frac{1}{\Delta z^2} \right) + \frac{2\kappa\Delta t}{k} \left(\frac{h_1}{\Delta x} + \frac{h_2}{\Delta y} + \frac{h_3'}{\Delta z} \right) \right] T_{i,j,k} \end{aligned} \tag{A.38}$$

Node number 21:

$$\begin{aligned} T'_{i,j,k} - T_{i,j,k} &= \frac{\kappa\Delta t}{\Delta x^2} (T_{i-1,j,k} + T_{i+1,j,k}) + \frac{2\kappa\Delta t}{\Delta y^2} T_{i,j+1,k} + \frac{2\kappa\Delta t}{\Delta z^2} T_{i,j,k+1} \\ &\quad - \left[2\kappa\Delta t \left(\frac{1}{\Delta x^2} + \frac{1}{\Delta y^2} + \frac{1}{\Delta z^2} \right) + \frac{2\kappa\Delta t}{k} \left(\frac{h_2}{\Delta y} + \frac{h_3'}{\Delta z} \right) \right] T_{i,j,k} \end{aligned} \tag{A.39}$$

Node number 22:

$$\begin{aligned} T'_{i,j,k} - T_{i,j,k} &= \frac{2\kappa\Delta t}{\Delta x^2} T_{i-1,j,k} + \frac{2\kappa\Delta t}{\Delta y^2} T_{i,j+1,k} + \frac{2\kappa\Delta t}{\Delta z^2} T_{i,j,k+1} \\ &\quad - \left[2\kappa\Delta t \left(\frac{1}{\Delta x^2} + \frac{1}{\Delta y^2} + \frac{1}{\Delta z^2} \right) + \frac{2\kappa\Delta t}{k} \left(\frac{h_1'}{\Delta x} + \frac{h_2}{\Delta y} + \frac{h_3'}{\Delta z} \right) \right] T_{i,j,k} \end{aligned} \tag{A.40}$$

Node number 23:

$$\begin{aligned} T'_{i,j,k} - T_{i,j,k} &= \frac{2\kappa\Delta t}{\Delta x^2} T_{i-1,j,k} + \frac{\kappa\Delta t}{\Delta y^2} (T_{i,j-1,k} + T_{i,j+1,k}) + \frac{2\kappa\Delta t}{\Delta z^2} T_{i,j,k+1} \\ &\quad - \left[2\kappa\Delta t \left(\frac{1}{\Delta x^2} + \frac{1}{\Delta y^2} + \frac{1}{\Delta z^2} \right) + \frac{2\kappa\Delta t}{k} \left(\frac{h_1'}{\Delta x} + \frac{h_3'}{\Delta z} \right) \right] T_{i,j,k} \end{aligned} \tag{A.41}$$

Node number 24:

$$\begin{aligned} T'_{i,j,k} - T_{i,j,k} &= \frac{2\kappa\Delta t}{\Delta x^2} T_{i-1,j,k} + \frac{2\kappa\Delta t}{\Delta y^2} T_{i,j-1,k} + \frac{2\kappa\Delta t}{\Delta z^2} T_{i,j,k+1} \\ &\quad - \left[2\kappa\Delta t \left(\frac{1}{\Delta x^2} + \frac{1}{\Delta y^2} + \frac{1}{\Delta z^2} \right) + \frac{2\kappa\Delta t}{k} \left(\frac{h_1'}{\Delta x} + \frac{h_2'}{\Delta y} + \frac{h_3'}{\Delta z} \right) \right] T_{i,j,k} \end{aligned} \tag{A.42}$$

Node number 25:

$$T'_{i,j,k} - T_{i,j,k} = \frac{\kappa\Delta t}{\Delta x^2}(T_{i-1,j,k} + T_{i+1,j,k}) + \frac{2\kappa\Delta t}{\Delta y^2}T_{i,j-1,k} + \frac{2\kappa\Delta t}{\Delta z^2}T_{i,j,k+1}$$
$$-\left[2\kappa\Delta t\left(\frac{1}{\Delta x^2} + \frac{1}{\Delta y^2} + \frac{1}{\Delta z^2}\right) + \frac{2\kappa\Delta t}{k}\left(\frac{h_2'}{\Delta y} + \frac{h_3'}{\Delta z}\right)\right]T_{i,j,k} \qquad \text{(A.43)}$$

Node number 26:

$$T'_{i,j,k} - T_{i,j,k} = \frac{2\kappa\Delta t}{\Delta x^2}T_{i+1,j,k} + \frac{2\kappa\Delta t}{\Delta y^2}T_{i,j-1,k} + \frac{2\kappa\Delta t}{\Delta z^2}T_{i,j,k+1}$$
$$-\left[2\kappa\Delta t\left(\frac{1}{\Delta x^2} + \frac{1}{\Delta y^2} + \frac{1}{\Delta z^2}\right) + \frac{2\kappa\Delta t}{k}\left(\frac{h_1}{\Delta x} + \frac{h_2'}{\Delta y} + \frac{h_3'}{\Delta z}\right)\right]T_{i,j,k} \qquad \text{(A.44)}$$

Node number 27:

$$T'_{i,j,k} - T_{i,j,k} = \frac{2\kappa\Delta t}{\Delta x^2}T_{i+1,j,k} + \frac{\kappa\Delta t}{\Delta y^2}(T_{i,j-1,k} + T_{i,j+1,k}) + \frac{2\kappa\Delta t}{\Delta z^2}T_{i,j,k+1}$$
$$-\left[2\kappa\Delta t\left(\frac{1}{\Delta x^2} + \frac{1}{\Delta y^2} + \frac{1}{\Delta z^2}\right) + \frac{2\kappa\Delta t}{k}\left(\frac{h_1}{\Delta x} + \frac{h_3'}{\Delta z}\right)\right]T_{i,j,k} \qquad \text{(A.45)}$$

Node number 28:

$$T'_{i,j,k} - T_{i,j,k} = \frac{\kappa\Delta t}{\Delta x^2}(T_{i+1,j,k} + T_{i-1,j,k}) + \frac{\kappa\Delta t}{\Delta y^2}(T_{i,j-1,k} + T_{i,j+1,k}) + \frac{2\kappa\Delta t}{\Delta z^2}T_{i,j,k+1}$$
$$-\left[2\kappa\Delta t\left(\frac{1}{\Delta x^2} + \frac{1}{\Delta y^2} + \frac{1}{\Delta z^2}\right) + \frac{2\kappa\Delta t}{k}\left(\frac{h_3'}{\Delta z}\right)\right]T_{i,j,k} \qquad \text{(A.46)}$$

Examination of Eqs A.19 to A.46 shows that out of 28 characteristic nodal equations only four equations are unique. These equations correspond to the four typical nodes shown in Fig. A.2, and are further discussed in Section 3.1. The stability analysis of Eqs A.19 to A.46 is shown in Appendix B.

APPENDIX B. STABILITY ANALYSIS OF FINITE DIFFERENCE EQUATIONS

This Appendix is continuation of discussion from Section 5.1.5 and presents equations which were used for stability analysis.

First step in the stability analysis is to get a finite difference equation into the form

$$T'_{i,j,k} - T_{i,j,k} \leq G(\Omega - T_{i,j,k}) \ , \tag{B.1}$$

where G represent a collection of time and space terms, and Ω represents a collection of space and termperature terms.

For steady-state solution, Eq. B.1 results in

$$G \geq \frac{T_{i,j,k}' - T_{i,j,k}}{\Omega - T_{i,j,k}} \ . \tag{B.2}$$

Sufficient condition for convergence of Eq. B.2 to steady state temperature is

$$0 \leq G \leq 1 . \tag{B.3}$$

To illustrate development of the stability criteria for the given problem, consider an example where temperature difference for an interior node at coordinates x, y, z can be shown, Eq. A.36, to be

$$T'_{i,j,k} - T_{i,j,k} = \frac{\kappa \Delta t}{\Delta x^2}(T_{i+1,j,k} + T_{i-1,j,k}) + \frac{\kappa \Delta t}{\Delta y^2}(T_{i,j+1,k} + T_{i,j-1,k}) + \frac{\kappa \Delta t}{\Delta z^2}(T_{i,j,k-1} + T_{i,j,k+1})$$

$$- \left[2\kappa \Delta t \left(\frac{1}{\Delta x^2} + \frac{1}{\Delta y^2} + \frac{1}{\Delta z^2} \right) \right] T_{i,j,k} \ . \tag{B.4}$$

The following steps show a procedure taken to write Eq. B.4 in the form of Eq. B.1.

Group terms,

$$\begin{aligned} T'_{i,j,k} - T_{i,j,k} = \kappa \Delta t \left[\frac{T_{i+1,j,k} + T_{i-1,j,k}}{\Delta x^2} + \frac{T_{i,j+1,k} + T_{i,j-1,k}}{\Delta y^2} + \frac{T_{i,j,k-1} + T_{i,j,k+1}}{\Delta z^2} \right] \\ - \left[2\kappa \Delta t \left(\frac{1}{\Delta x^2} + \frac{1}{\Delta y^2} + \frac{1}{\Delta z^2} \right) \right] T_{i,j,k} \end{aligned} . \tag{B.5}$$

Define time space term

$$G = 2\kappa \Delta t \left(\frac{1}{\Delta x^2} + \frac{1}{\Delta y^2} + \frac{1}{\Delta z^2} \right) . \tag{B.6}$$

Substitute Eq. B.6 into Eq. B.5

$$T'_{i,j,k} - T_{i,j,k} = \kappa \Delta t \left[\frac{T_{i-1,j,k} + T_{i+1,j,k}}{\Delta x^2} + \frac{T_{i,j-1,k} + T_{i,j+1,k}}{\Delta y^2} + \frac{T_{i,j,k-1} + T_{i,j,k+1}}{\Delta z^2} \right] - G \cdot T_{i,j,k} . \tag{B.7}$$

Simplify Eq. B.7

$$\begin{aligned} T'_{i,j,k} - T_{i,j,k} = G \cdot \Bigg\{ \left[2\left(\frac{1}{\Delta x^2} + \frac{1}{\Delta y^2} + \frac{1}{\Delta z^2} \right) \right]^{-1} \\ \kappa \Delta t \left[\frac{T_{i-1,j,k} + T_{i+1,j,k}}{\Delta x^2} + \frac{T_{i,j-1,k} + T_{i,j+1,k}}{\Delta y^2} + \frac{T_{i,j,k-1} + T_{i,j,k+1}}{\Delta z^2} \right] - T_{i,j,k} \Bigg\} . \end{aligned} \tag{B.8}$$

Define space and temperature term

$$\Omega = \left[\frac{T_{i-1,j,k} + T_{i+1,j,k}}{\Delta x^2} + \frac{T_{i,j-1,k} + T_{i,j+1,k}}{\Delta y^2} + \frac{T_{i,j,k+1} + T_{i,j,k-1}}{\Delta z^2} \right]^{-1}$$

$$\cdot \left[2\left(\frac{1}{\Delta x^2} + \frac{1}{\Delta y^2} + \frac{1}{\Delta z^2} \right) \right] . \tag{B.9}$$

Substitute Eq. B.9 into Eq. B.8 to obtain

$$T'_{i,j,k} - T_{i,j,k} \leq G(\Omega - T_{i,j,k}) . \tag{B.10}$$

Clearly Eq. B.10 is of the form of Eq. B.1. Solution of Eq. B.10, subject to the condition imposed by Eq. B.3, yields

$$2\kappa \Delta t \left(\frac{1}{\Delta x^2} + \frac{1}{\Delta y^2} + \frac{1}{\Delta z^2} \right) \leq 1 . \tag{B.11}$$

Rearrange Eq. B.11, to get

$$\Delta t \leq \left[2\kappa \left(\frac{1}{\Delta x^2} + \frac{1}{\Delta y^2} + \frac{1}{\Delta z^2} \right) \right]^{-1} . \tag{B.12}$$

Following the above procedure, a stability analysis of the finite difference equations for all of the nodes shown in Fig. B.1 can be performed. Different values of heat conduction might result in different values for each side of the workpiece. Therefore, it is necessary to perform stability analysis for all 28 finite difference equations. The results of these analysis are

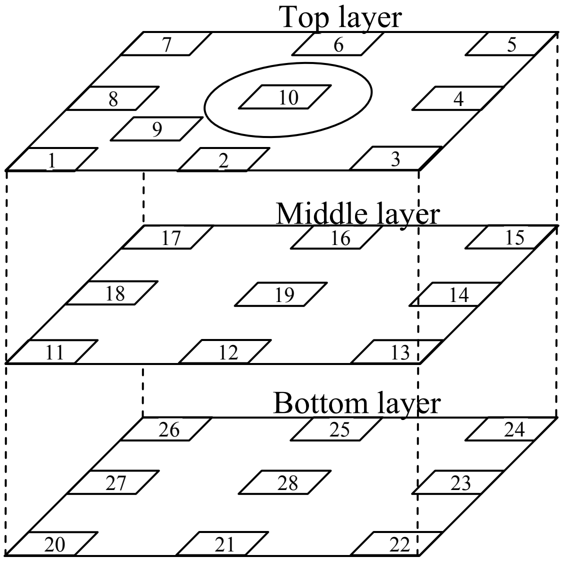

Fig. B.1. Three "layers" of a workpiece.

Node number 1:

$$\Delta t \le \frac{1}{2\kappa\left[\left(\frac{1}{\Delta x^2}+\frac{1}{\Delta y^2}+\frac{1}{\Delta z^2}\right)+\frac{1}{k}\left(\frac{h_1}{\Delta x}+\frac{h_2}{\Delta y}+\frac{h_3}{\Delta z}\right)\right]}, \tag{B.13}$$

Node number 2:

$$\Delta t \le \frac{1}{2\kappa\left[\left(\frac{1}{\Delta x^2}+\frac{1}{\Delta y^2}+\frac{1}{\Delta z^2}\right)+\frac{1}{k}\left(\frac{h_2}{\Delta y}+\frac{h_3}{\Delta z}\right)\right]}, \tag{B.14}$$

Node number 3:

$$\Delta t \le \frac{1}{2\kappa\left[\left(\frac{1}{\Delta x^2}+\frac{1}{\Delta y^2}+\frac{1}{\Delta z^2}\right)+\frac{1}{k}\left(\frac{h_1'}{\Delta x}+\frac{h_2}{\Delta y}+\frac{h_3}{\Delta z}\right)\right]}, \tag{B.15}$$

Node number 4:

$$\Delta t \leq \frac{1}{2\kappa\left[\left(\frac{1}{\Delta x^2}+\frac{1}{\Delta y^2}+\frac{1}{\Delta z^2}\right)+\frac{2\kappa\Delta t}{k}\left(\frac{h_1'}{\Delta x}+\frac{h_3}{\Delta z}\right)\right]}\ , \tag{B.16}$$

Node number 5:

$$\Delta t \leq \frac{1}{2\kappa\left[\left(\frac{1}{\Delta x^2}+\frac{1}{\Delta y^2}+\frac{1}{\Delta z^2}\right)+\frac{1}{k}\left(\frac{h_1'}{\Delta x}+\frac{h_2'}{\Delta y}+\frac{h_3}{\Delta z}\right)\right]}\ , \tag{B.17}$$

Node number 6:

$$\Delta t \leq \frac{1}{2\kappa\left[\left(\frac{1}{\Delta x^2}+\frac{1}{\Delta y^2}+\frac{1}{\Delta z^2}\right)+\frac{1}{k}\left(\frac{h_2'}{\Delta y}+\frac{h_3}{\Delta z}\right)\right]}\ , \tag{B.18}$$

Node number 7:

$$\Delta t \leq \frac{1}{2\kappa\left[\left(\frac{1}{\Delta x^2}+\frac{1}{\Delta y^2}+\frac{1}{\Delta z^2}\right)+\frac{1}{k}\left(\frac{h_1}{\Delta x}+\frac{h_2'}{\Delta y}+\frac{h_3}{\Delta z}\right)\right]}\ , \tag{B.19}$$

Node number 8:

$$\Delta t \leq \frac{1}{2\kappa\left[\left(\frac{1}{\Delta x^2}+\frac{1}{\Delta y^2}+\frac{1}{\Delta z^2}\right)+\frac{1}{k}\left(\frac{h_1}{\Delta x}+\frac{h_3}{\Delta z}\right)\right]}\ , \tag{B.20}$$

Node number 9:

$$\Delta t \le \frac{1}{2\kappa\left[\left(\frac{1}{\Delta x^2}+\frac{1}{\Delta y^2}+\frac{1}{\Delta z^2}\right)+\frac{1}{k}\left(\frac{h_3}{\Delta z}\right)\right]}\ , \tag{B.21}$$

Node number 10:

$$\Delta t \le \frac{1}{2\kappa\left[\left(\frac{1}{\Delta x^2}+\frac{1}{\Delta y^2}+\frac{1}{\Delta z^2}\right)+\frac{1}{k}\left(\frac{h_3}{\Delta z}\right)\right]}\ , \tag{B.22}$$

Node number 11:

$$\Delta t \le \frac{1}{2\kappa\left[\left(\frac{1}{\Delta x^2}+\frac{1}{\Delta y^2}+\frac{1}{\Delta z^2}\right)+\frac{1}{k}\left(\frac{h_1}{\Delta x}+\frac{h_2}{\Delta y}\right)\right]}\ , \tag{B.23}$$

Node number 12:

$$\Delta t \le \frac{1}{2\kappa\left[\left(\frac{1}{\Delta x^2}+\frac{1}{\Delta y^2}+\frac{1}{\Delta z^2}\right)+\frac{1}{k}\left(\frac{h_2}{\Delta y}\right)\right]}\ , \tag{B.24}$$

Node number 13:

$$\Delta t \le \frac{1}{2\kappa\left[\left(\frac{1}{\Delta x^2}+\frac{1}{\Delta y^2}+\frac{1}{\Delta z^2}\right)+\frac{1}{k}\left(\frac{h_1'}{\Delta x}+\frac{h_2}{\Delta y}\right)\right]}\ , \tag{B.25}$$

Node number 14:

$$\Delta t \le \frac{1}{2\kappa\left[\left(\frac{1}{\Delta x^2}+\frac{1}{\Delta y^2}+\frac{1}{\Delta z^2}\right)+\frac{1}{k}\left(\frac{h_1'}{\Delta x}\right)\right]}\ , \tag{B.26}$$

Node number 15:

$$\Delta t \le \frac{1}{2\kappa\left[\left(\frac{1}{\Delta x^2}+\frac{1}{\Delta y^2}+\frac{1}{\Delta z^2}\right)+\frac{1}{k}\left(\frac{h_1'}{\Delta x}+\frac{h_2'}{\Delta y}\right)\right]}\ , \tag{B.27}$$

Node number 16:

$$\Delta t \le \frac{1}{2\kappa\left[\left(\frac{1}{\Delta x^2}+\frac{1}{\Delta y^2}+\frac{1}{\Delta z^2}\right)+\frac{1}{k}\left(\frac{h_2'}{\Delta y}\right)\right]}\ , \tag{B.28}$$

Node number 17:

$$\Delta t \le \frac{1}{2\kappa\left[\left(\frac{1}{\Delta x^2}+\frac{1}{\Delta y^2}+\frac{1}{\Delta z^2}\right)+\frac{1}{k}\left(\frac{h_1}{\Delta x}+\frac{h_2'}{\Delta y}\right)\right]}\ , \tag{B.29}$$

Node number 18:

$$\Delta t \le \frac{1}{2\kappa\left[\left(\frac{1}{\Delta x^2}+\frac{1}{\Delta y^2}+\frac{1}{\Delta z^2}\right)+\frac{1}{k}\left(\frac{h_1}{\Delta x}\right)\right]}\ , \tag{B.30}$$

Node number 19:

$$\Delta t \le \frac{1}{2\kappa\left[\left(\frac{1}{\Delta x^2}+\frac{1}{\Delta y^2}+\frac{1}{\Delta z^2}\right)\right]} \,, \tag{B.31}$$

Node number 20:

$$\Delta t \le \frac{1}{2\kappa\left[\left(\frac{1}{\Delta x^2}+\frac{1}{\Delta y^2}+\frac{1}{\Delta z^2}\right)+\frac{1}{k}\left(\frac{h_1}{\Delta x}+\frac{h_2}{\Delta y}+\frac{h_3'}{\Delta z}\right)\right]} \,, \tag{B.32}$$

Node number 21:

$$\Delta t \le \frac{1}{2\kappa\left[\left(\frac{1}{\Delta x^2}+\frac{1}{\Delta y^2}+\frac{1}{\Delta z^2}\right)+\frac{1}{k}\left(\frac{h_2}{\Delta y}+\frac{h_3'}{\Delta z}\right)\right]} \,, \tag{B.33}$$

Node number 22:

$$\Delta t \le \frac{1}{2\kappa\left[\left(\frac{1}{\Delta x^2}+\frac{1}{\Delta y^2}+\frac{1}{\Delta z^2}\right)+\frac{1}{k}\left(\frac{h_1'}{\Delta x}+\frac{h_2}{\Delta y}+\frac{h_3'}{\Delta z}\right)\right]} \,, \tag{B.34}$$

Node number 23:

$$\Delta t \le \frac{1}{2\kappa\left[\left(\frac{1}{\Delta x^2}+\frac{1}{\Delta y^2}+\frac{1}{\Delta z^2}\right)+\frac{1}{k}\left(\frac{h_1'}{\Delta x}+\frac{h_3'}{\Delta z}\right)\right]} \,, \tag{B.35}$$

Node number 24:

$$\Delta t \le \frac{1}{2\kappa\left[\left(\frac{1}{\Delta x^2}+\frac{1}{\Delta y^2}+\frac{1}{\Delta z^2}\right)+\frac{1}{k}\left(\frac{h_1'}{\Delta x}+\frac{h_2'}{\Delta y}+\frac{h_3'}{\Delta z}\right)\right]}\ , \tag{B.36}$$

Node number 25:

$$\Delta t \le \frac{1}{2\kappa\left[\left(\frac{1}{\Delta x^2}+\frac{1}{\Delta y^2}+\frac{1}{\Delta z^2}\right)+\frac{1}{k}\left(\frac{h_2'}{\Delta y}+\frac{h_3'}{\Delta z}\right)\right]}\ , \tag{B.37}$$

Node number 26:

$$\Delta t \le \frac{1}{2\kappa\left[\left(\frac{1}{\Delta x^2}+\frac{1}{\Delta y^2}+\frac{1}{\Delta z^2}\right)+\frac{1}{k}\left(\frac{h_1}{\Delta x}+\frac{h_2'}{\Delta y}+\frac{h_3'}{\Delta z}\right)\right]}\ , \tag{B.38}$$

Node number 27:

$$\Delta t \le \frac{1}{2\kappa\left[\left(\frac{1}{\Delta x^2}+\frac{1}{\Delta y^2}+\frac{1}{\Delta z^2}\right)+\frac{1}{k}\left(\frac{h_1}{\Delta x}+\frac{h_3'}{\Delta z}\right)\right]}\ , \tag{B.39}$$

Node number 28:

$$\Delta t \le \frac{1}{2\kappa\left[\left(\frac{1}{\Delta x^2}+\frac{1}{\Delta y^2}+\frac{1}{\Delta z^2}\right)+\frac{1}{k}\left(\frac{h_3'}{\Delta z}\right)\right]}\ . \tag{B.40}$$

The stability analysis show that for the specific values of thermal diffusivity κ, Δx, Δy, Δz, k and all h coefficients, such as $h_1, h_2, h_3, h_1', h_2', h_3'$, the governing time increament is controlled by Eqs B.13 through B.40. These equations specify the largest time increment which will still provide convergence in temperature calculations. That is, time increments equal to or less than that obtained from Eq. B.12 must be used in the finite difference computations.

For the copper workpiece used in this research, which has the dimension of 1 cm by 1 cm by 0.1 mm, the model dimensions of 2.5 mm by 2.5 mm by 0.1 mm was used in FDM calculations, due to the large temperature gradients and localized heat effect. Therefore, for the different meshing element size, the critical time increments were calculated for the different type of nodes, according to Eqs B.13 to 40, i.e.,

interior node: $\Delta t \leq 0.00200$ ms,

wall node: $\Delta t \leq 0.00245$ ms,

edge node: $\Delta t \leq 0.00228$ ms,

corner node: $\Delta t \leq 0.00296$ ms.

Then the time step less than the minimum value of the critical time increments was chosen and used in the FDM calculation.

APPENDIX C. ANALYTICAL CONSIDERATIONS FOR LASER MICROWELDING ON COPPER

The purpose of this Appendix is to present the calculations for the required energy, thermal time constant, and temperature variations for laser microwelding process studied in this Dissertation, based on the material properties for copper workpiece. Analytical equations were used to calculate the required energy, thermal time constant, and temperature for the spot on top surface of the workpiece at the center of the beam focus, and the values are compared with the computational results to show the validity of the computational results.

The material properties of copper, used in the study of this Dissertation, are listed in Table C.1.

Table C.1. Material properties of copper used in the Dissertation.

Property name	Symbol	Value
Density	ρ, kg/m^3	8960
Specific heat	c, J/kg°K	386
Thermal conductivity	k, W/m°K	401
Melting temperature	T_m, °K	1173
Vaporization temperature	T_v, °K	2836

In order to determine the energy that is required for laser microwelding for the copper workpiece used in the research of this Dissertation, Eq. 120 in Section 4.4.2 was used for welding conditions, that is, no material vaporization occurred, therefore, Eq. 120 could be written as

$$E = \rho V[c(T_m - T_{amb}) + L_m] \quad , \tag{C.1}$$

where E is the required energy, V is the volume of the melted material, c is the specific heats of the workpiece material in solid phases, T_m is the melting temperature, T_{amb} is the ambient temperature, and L_m is the latent heat of melting of the workpiece material. In the calculations, for the consideration of the volume of the melted material, assume that it has the height of the thickness of the workpiece, and the diameter range from the laser spot diameter 2w to 600 µm, which is the value summarized from the typical experimental results, as shown in Fig. 6.20. Also, taking the values of the complex refractive index to 1.06 µm for copper and the calculated absorptivity of 0.012 for copper, as discussed in Section 4.4.2, the required energy as the function of the diameter of the melted zone is calculated as shown in Fig. C.1. Therefore, based on the range of the calculated required energy, experiments were performed and the optimum energy level was found to be 5 J on the copper workpiece used in the research of this Dissertation.

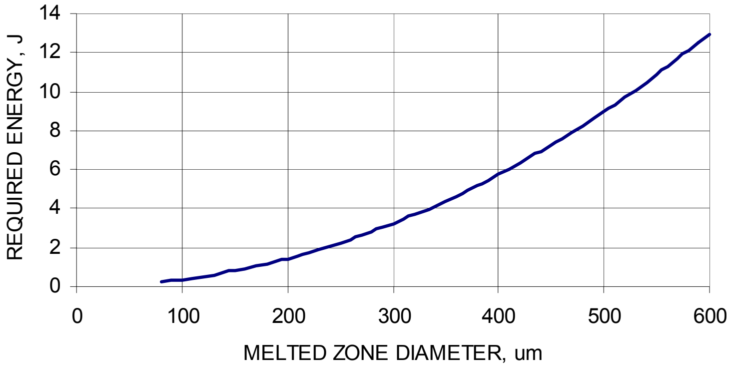

Fig. C.1. Calculated required energy as the function of the diameter of the melted zone for laser microwelding on copper.

In laser microwelding experiments, the typical value of laser pulse length of 4 ms was used, and the copper workpiece had the dimensions of 1 cm by 1 cm by 0.1 mm.

To estimate the thermal time constant τ, which is defined as the object reaches 63.28% of the temperature change due to applied external thermal load, can be calculated as (Pryputniewicz, 2001)

$$\tau = \frac{h^2}{4\kappa} = \frac{h^2}{4k/\rho c} = 7.613 \times 10^{-5}\ \sec = 0.076 ms \quad , \tag{C.2}$$

where h and κ are the thickness and thermal diffusivity of the copper workpiece, respectively.

For laser materials processing, the thermal penetration depth, l_{th}, for a fixed pulse length is defined as a function of the thermal diffusivity of the workpiece, κ, and pulse length t_p, i.e.,

$$l_{th} = 2\sqrt{\kappa t_p} = 2\sqrt{(k/\rho c)t_p} = 7.249 \times 10^{-4} m = 0.7149 mm \,. \tag{C.3}$$

Under conduction limited conditions, as for the case occurs for the thin copper workpiece that was used in laser microwelding experiments in this Dissertation, the temperature at the center of the beam focus (r=0) can be estimated according to Eq. 62 as

$$T(0,t) - T_0 = \frac{AI(0)w}{k(2\pi)^{1/2}} \tan^{-1}\left(\frac{8\kappa t}{w^2}\right)^{1/2} \quad , \tag{C.4}$$

where k is the thermal conductivity, κ is thermal diffusivity, w is the Gaussian beam radius, which is 40 μm for the Nd:YAG laser used in this Dissertation, T_0 is the ambient temperature, and t is time. When assuming the energy absorption coefficient A was

0.012, as discussed in Section 4.4.2, the temperature at the center of the beam focus was calculated based on Eq. 62 and is shown in Fig. C.2.

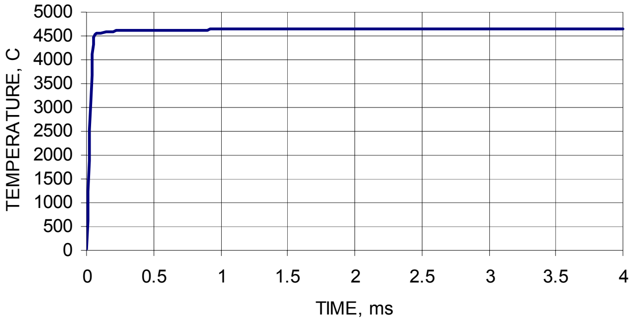

Fig. C.2. Analytical results of temperature variation for laser microwelding process, based on Eq. 62.

Assume *T(0,t)=T*$_m$, the melting temperature, then the time for the spot at the center of the beam focus (r=0) to reach melting temperature, t_m, can be estimated, by substituting T_m into Eq. C.4 and solve for t_m, which has the value of 5.032 µs, note that this value is very short when compared with the pulse of the laser beam.

For the estimation of the depth of penetration, z_m, of the weld pool under laser microwelding conditions used in this Dissertation, according to Eq. 63, that is,

$$z_m(t) \sim \frac{0.16AI}{\rho L_m}(t - t_m) \quad , \tag{C.5}$$

where ρ is the density of the melt and L_m is the latent heat of melting, and t_m is the time at which $T(z=0)=T_m$,. The estimation of depth of penetration for the amount of energy provided by the laser in the experiments was calculated and shown in Fig. C.3.

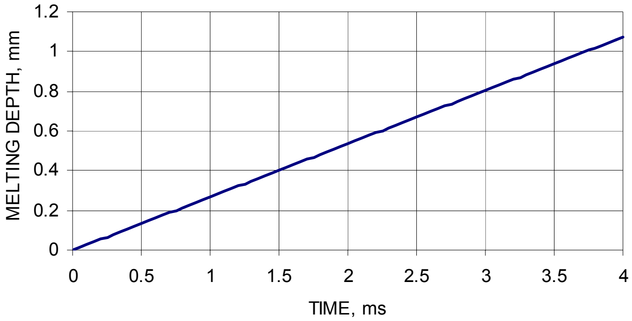

Fig. C.3. Analytical results of depth of penetration for laser microwelding process, based on Eq. 63.

APPENDIX D. ANALYTICAL CONSIDERATIONS FOR LASER MICRODRILLING ON STAINLESS STEEL 304

The purpose of this Appendix is to present some analytical calculations for laser microdrilling process studied in this Dissertation, including the calculations for thermal time constant, threshold intensity, and durations of heating stage during laser microdrilling, based on the analytical equations in Chapter 4. And the values can be a reference for computational and experimental investigations.

The material properties of stainless steel 304, used in this Dissertation, are listed in Table D.1.

Table D.1. Material properties of stainless steel 304 used in the Dissertation.

Property name	Symbol	Value
Density	ρ, kg/m^3	7800
Specific heat	c, J/kg°K	465
Thermal conductivity	k, W/m°K	16.4
Melting temperature	T_m, °C	1460
Vaporization temperature	T_v, °C	2315

In laser microdrilling experiments performed in the research of this Dissertation, the typical values of laser energy of 3.5 J and pulse length of 1 ms were used, and the stainless steel 304 workpiece has the thickness of 30 mils, which is 0.762 mm.

To estimate the thermal time constant τ, which is defined as the object reaches 63.28% of the temperature change due to applied external thermal load, can be calculated as (Pryputniewicz, 2001)

$$\tau = \frac{h^2}{4\kappa} = \frac{h^2}{4k/(\rho c)} = 3.203 \times 10^{-2}\,\text{sec} = 32ms \quad , \tag{D.1}$$

where h and κ are the thickness and thermal diffusivity of the stainless steel 304 workpiece, respectively.

According to Eq. 40 in Chapter 4, the threshold intensity, I_v, for material removal in laser drilling to occur, which is determined by the losses due to surface reflection and heat conduction into the material, and I_v is defined as

$$I_v = \frac{T_v k \sqrt{2\pi}}{A w_0 \, arctg \sqrt{8\kappa t_p / w_0^2}} \quad , \tag{D.2}$$

where T_v is the vaporization temperature, k is thermal conductivity of the workpiece material, A is the energy absorption coefficient at the workpiece surface, w_0 is the beam radius with a Gaussian intensity distribution, κ is thermal diffusivity of the workpiece material, and t_p is the length of the laser pulse.

Therefore, assume the energy absorption coefficient is 0.356, and laser pulse length is 1 ms for microdrilling, the threshold intensity was calculated as 5.494×10^9 W/m^2. However, the threshold intensity in Eq. D.2 showed a lower value than the actual onset breakthrough intensity, as shown in Fig. 6.4, which has the power level of 2.25 kW and leads to the intensity of 1.594×10^{11} W/m^2.

The duration of the heating stage, that is, the time period before the spot at the center of the beam focus on top surface of the workpiece reaches melting temperature, for laser microdrilling can be estimated, based on Eq. 15 in Chapter 4, as

$$t_h = \frac{\pi}{\kappa} \left[\frac{k\left(T_m - T_0\right)}{2 I_0} \right]^2 \quad . \tag{D.3}$$

Substituting the value for the threshold intensity calculated based on Eq. D.2, that is, 5.494×10^{9} W/m^2, into Eq. D.3, the duration of the heating stage was 3.209×10^{-3} ms. When using the real power intensity at the onset of the breakthrough, which has the value of 1.594×10^{11} W/m^2, the duration of the heating stage was calculated as 3.815×10^{-6} ms. Note that these calculated values for the durations of the heating stage are much smaller than the pulse length used in laser microdrilling, which was 1 ms.

APPENDIX E. CALCULATION OF TENSILE STRENGTH OF LASER MICROWELDS

In the tensile-shear testing in Chapter 6, the peak load, *F*, in the force-extension measurements for a single laser microweld, when laser power was 1.25 kW, was *F* = 67.60 N, Fig. 6.30a, and the diameters of the fusion zone measured at the front and back surfaces for this power level were *D_front* = 704 μm and *D_back* = 532 μm, respectively. Therefore, the tensile strength, *TS*, can be estimated as

$$TS = \frac{F}{A} \quad , \tag{E.1}$$

where *A* is the estimated average cross-sectional area of the fusion zone, and can be calculated as

$$A = \pi \left(\frac{D\_ave}{2} \right)^2 = \pi \left[\frac{(D\_front + D\_back)/2}{2} \right]^2 \quad , \tag{E.2}$$

where *D_ave* is the average diameter of the microweld. Therefore, when the laser power of 1.25 kW was used, the calculated tensile strength is about 225.36 MPa.

When laser power was 1.5 kW and a single laser microweld was made in the workpiece, the peak load in the force-extension curve was *F* = 90.34 N, Fig. 6.30b, and the diameters of the fusion zone measured at the front and back surfaces were *D_front* = 743 μm and *D_back* = 577 μm, respectively. Therefore, the calculated tensile strength is about 264.06 MPa. Furthermore, the tensile strengths as the functions of estimated average fusion zone diameters for *P* = 1.25 kW and *P* = 1.5 kW are shown in Fig. E.1.

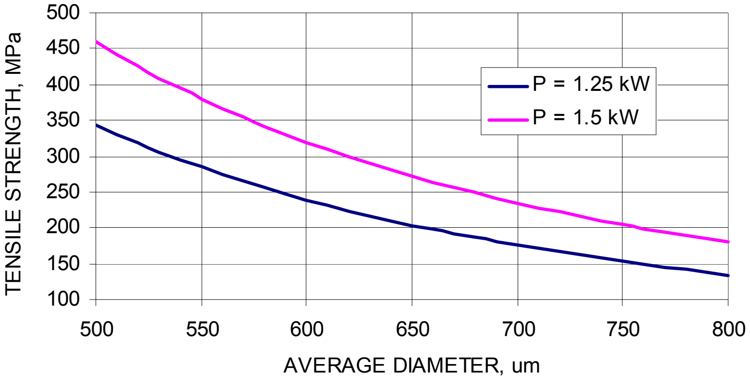

Fig. E.1. Tensile strengths calculated from the force-extension measurements for a single microweld in the workpieces under different laser power levels.